University of Applied Science Jena

Department of SciTec

Scientific Instrumentation

MASTER THESIS

submitted by

Yanwing Ng

born in HONG KONG

under the supervision of

Prof. Dr. Brend Ploss

Finite Element Analysis
of the Cooling System
for the Mu3e Experiment

This Master Thesis has been carried out by

Yanwing Ng

at the

Physikalisches Institut
in Heidelberg

under the supervision of

Prof. Dr. André Schoening

Abstract

The Mu3e experiment searches for the Charge Lepton Flavor Violating decay $\mu^+ \to e^+e^-e^+$, which is strongly suppressed and unobservable in the Standard Model. Hence any signal form the decay indicates a New Physics beyond the Standard Model. The experiment is aimed to reach a sensitivity to the decay for the branching ratio of 10^{-16}. For this purpose, a detector with precise momentum, timing and vertex resolution with a high intensity muon source are required. The experiment observes decay electrons/positrons at energy below 53 MeV, such that multiple coulomb scattering is a dominant factor to the resolution. Therefore, a detector design with low material budget must be considered.

The Mu3e experiment makes use of High Voltage Monolithic Active Pixel Sensor (HV-MAPS), which can be thinned down to $50\mu m$ and operated at high decay rate. The power consumption of the HV-MAPS is expected to be $250\mathrm{mV/cm^2}$. Additionally the front end FPGAs in the read-out electronics have a power consumption of 25W per chip. Therefore, a cooling system with minimal material budget is design to provide sufficient cooling power to the sensors, keeping the accuracy of the measurement at an appropriate level. In this design gaseous helium cooling is applied in the acceptance region of the detector and water cooling is applied to the passive region near the beamline. In this thesis, designated models of the detector with cooling system are constructed. Computational Fluid Dynamics (CFD) using Finite Element Analysis (FEA), is applied on the models to illustrate the efficiency of the cooling system.

The analytical results indicate the design is capable of providing sufficient cooling to the phase I Mu3e experiment with a power consumption of $250\mathrm{mW/cm^2}$. Concerning phase II experiment or phase I experiment with power consumption at level of $400\mathrm{mW/cm^2}$, an improvement of the cooling system may be required.

Contents

Chapter 1

Introduction

The Standard Model (SM) is a successful theory to describe the interactions between elementary particles and there properties. It is also well supported in experimental research. One of the greatest successes was the discovery of Higgs Boson in 2012 at the Large Hadron Collider (LHC), which completes the SM. However, there are still phenomenas and experimental results that can not be explained by the SM, e.g. gravitation and dark matter. These suggest the existence of Physics beyond Standard Model. Despite the fact that Lepton Flavor Violation (LFV) is forbidden in the SM, neutrino mixing has been observed in various experiment in the last decade. So far LFV processes have only been observed in the neutrino sector but the LFV decay in charged lepton sector has not been discovered yet.

The goal of the Mu3e Experiment is to search for the charged lepton flavor violating (CLFV) decay $\mu^+ \rightarrow e^+e^-e^+$ with sensitivity to the branching ratio of 10^{-16} at 90% confidence level. The decay is forbidden at tree level in the SM and only possible to be induced by neutrino mixing through higher order loop diagrams. Due to the small neutrino mass, the decay is heavily suppressed and unobservable in the SM. Therefore, any signal of the decay would be a clear sign of new physics beyond Standard Model. To observe the decay with the desired sensitivity, a detector with high momentum, timing and vertex resolution is required. As the moun decay yields gives electrons (positron) in low energy regime, the resolution of the detector is limited by multiple coulomb scattering. Hence, a design with minimal material is needed. Therefore, the Mu3e experiment makes use of the ultra thin High Voltage Monolithic Active Pixel Sensors (HV-MAPS) complemented by time of flight systems.

The monolithic design of HV-MAPS integrates all readout electronics and sensor on the device, providing a excellent momentum and timing resolution with a sensor thickness of $50\mu m$. The power consumption of HV-MAPS is expected to be approximately 250 mW/cm^2. Due to the requirement of low material budget, gaseous helium cooling is planned to applied in the acceptance region of the detector, complemented by water cooling in the inactive region.

In this thesis, the cooling concept is studied via computational fluid dynamics (CFD) simulation using finite element analysis (FEA). The discussion covers the major components of the Mu3e detector. To be on the safe side, simulations with power consumption up to $400mW/cm^2$ have been performed. Chapter 2 gives a brief introduction to the experiment. Chapter 3 introduces the mechanical design of the Mu3e cooling system and previous thesis related to it. Chapter 4 outlines the procedure of finite element analysis and the program Autodesk® CFD Simulation. Chapter 5 - 10 constitute the main part of this thesis. The measurement of cooling test from previous thesis is

verfiy by CFD simulation in chapter 5. The simulations of the outer detector is discussed in chapter 6. In chapter 7 the optimization of the gas distribution system is performed. Inner components of the detector are added to the model in chapter 8. The water cooling system is tested in chapter 9 and the simulations of the complete Phase I Mu3e detector are discussed. Chapter 10 discusses the possibilities for improvements of the local cooling system.

Chapter 2

The Mu3e Experiment

The goal of Mu3e experiment is to search for the Charge Lepton Flavor Violating decay $\mu^+ \rightarrow e^+ e^+ e^-$ with a sensitivity corresponding to the branching ratio limit of 10^{-16} at 90% confidence level. This limit is four orders of magnitude lower than the previous search, performed by SINDRUM experiment, which gave a limit of $Br(\mu^+ \rightarrow e^+ e^+ e^-) < 1 \cdot 10^{-12}$ at 90% CL [9].

The experiment is carried out at the Paul Scherrer Institute (PSI) in Switzerland. It runs in two phases. Phase I is aimed to gain experience with the new technologies and validate the experimental concept, while looking for a sensitivity to the branching ratio of 10^{-15}. In this phase, only part of the detector and read-out electronics is constructed . With the use of the existing muon beam at PSI, providing 10^8Hz of mouns on target, the intermediate gaol can be reached. In Phase II, the ultimate sensitivity of 10^{-16} is aimed for. In order to archive the goal in a reasonable data taking time, a new beamline has to be installed, which delivers more than $2 \cdot 10^9$Hz of muons.

2.1   Motivation

In the Standard Model (SM), lepton flavor is conserved at tree level. Allowed decays are eg. $\mu^+ \rightarrow e^+ \nu_e \overline{\nu}_\mu$ and $\mu^+ \rightarrow e^+ e^- e^+ \nu_e \overline{\nu}_\mu$. However, the change in lepton flavor has been observed in form of neutrino oscillation in several experiment[1]. Flavor changing interaction is labeled as lepton flavor violation (LFV). Consequently, the SM has to been extended for neutrinos with small but definite mass and LFV is also expected for charged lepton sector.

In the SM, charged lepton flavor violating reactions are forbidden at tree level and can only be induced by lepton mixing through higher order loop diagram. However, the dominant neutrino mixing loop diagram (Figure 2.1) is heavily suppressed in the Standard Model with branching ratio $Br(\mu^+ \rightarrow e^+ e^+ e^-) < 1 \cdot 10^{-54}$. Therefore, any observation of charged lepton flavor violation(CLFV) would be a clear sign for new physics beyond the SM.

An example are new supersymmetric (SUSY) particles running in a loop of a γ/Z- penguin diagram as shown in figure 2.2. Another example would be a tree level digram involving new particles, labeled as X in figure 2.3, such as R-parity violation scalar neutrinos or new heavy vector bosons [8]

---

[1]Super-Kamiokande[16], SNO[17], KamLAND[18] and others.

3
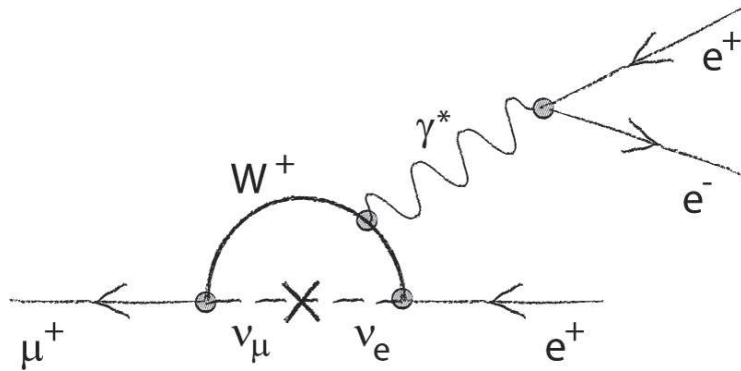
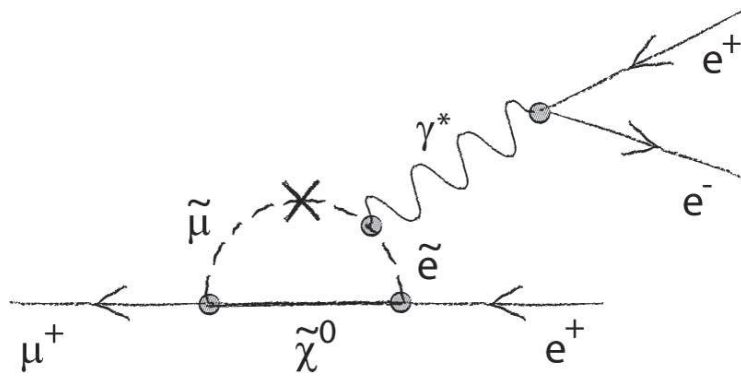Figure 2.1: Feynman diagram for the $\mu \to eee$ process via neutrino mixing

Figure 2.2: Diagram for lepton flavor violation involving supersymmetric particles

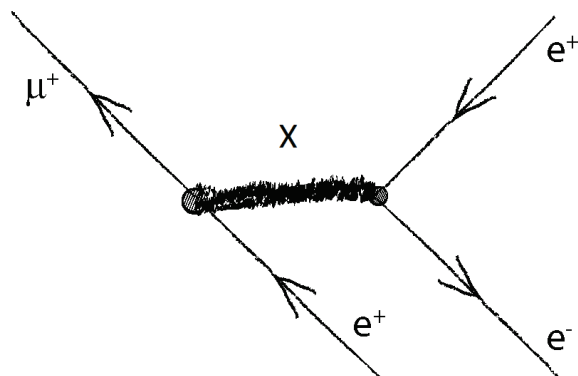Figure 2.3: Diagram for lepton flavor violation at tree level by exchanging a new particle X

2.2   The Decay $\mu^+ \to e^+ e^+ e^-$

2.2.1   Kinematics

In the decay $\mu^+ \to e^+ e^+ e^-$, all particles decay simultaneously at the same vertex. Assuming that the muon comes to rest when it hits the stopping target, the vectorial sum of all decay particle momenta should be zero :

$$|\vec{p}_{tot}| = \left|\sum \vec{p}_i\right| = 0$$

and the total energy of the decay particle has to be equal to the muon mass. The energies of the decay electrons or positrons are all below 53 MeV, which is half of the rest mass of the muon.

2.2.2   Background

In order to reach the desired sensitivity, it is necessary to distinguish between the signal decay $\mu^+ \to e^+ e^- e^+$ and background decays. There are mainly two sources of background. One is the muon decay with Internal conversions and the other is accidental background from incorrectly reconstructed events.

Internal Conversions

The Internal conversion decay $\mu^+ \to e^+ e^+ e^- \nu_e \bar{\nu}_\mu$ occurs with a branching ratio of $3.4 \cdot 10^{-5}$. It originates from a radiative muon decay where the emitted photon immediately decays into a pair of electron and positron. A diagram for the decay is shown in figure 2.4. Due to the missing energy from the neutrinos, this background can be suppressed by reconstruction of the neutrino with a detector of good momentum and energy resolution.
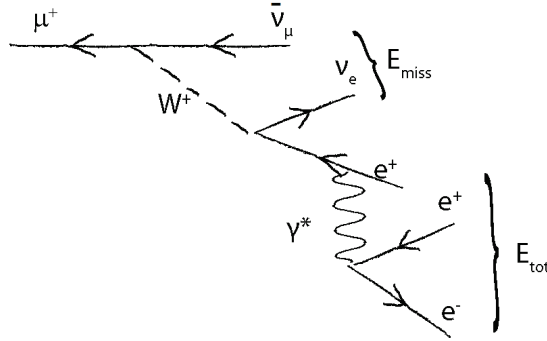

Figure 2.4: Diagram for the internal conversion decay $\mu^+ \to e^+ e^+ e^- \nu_e \bar{\nu}_\mu$

Figure 2.5 shows the Branching ratio of the Internal conversion events as a function of the missing energy.[1]. The plot indicates a requirement of a average momentum resolution better than 1 MeV for the detector at phase II.
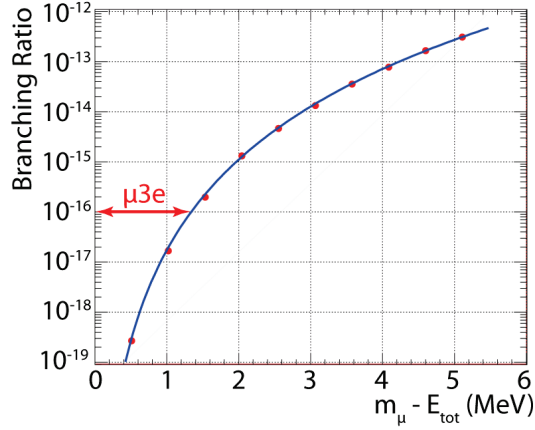
Figure 2.5: Branching ratio of the Internal conversion decay $\mu^+ \to e^+ e^+ e^- \nu_e \bar{\nu}_\mu$ as function of the missing energy [23]

Accidental Background

The accidental background comes from incorrectly reconstructed events, where 2 positrons and 1 electron from distinct decays are recognized as products of a single process. The main contribution to the accidental background comes from the Michel decay $\mu^+ \to e^+ \nu_e \bar{\nu}_\mu$. An electron can be produced by Bhabha scattering from a positron originated from Michel decay or beam-positron. This process also crates a positron in the same vertex as the electron. Figure 2.6 shows a schematic comparison of the signal decay and an accidental background event. As this accidental background comes from discrete decays which originated from different vertices and time, it can be suppressed by precise timing and vertex resolution .

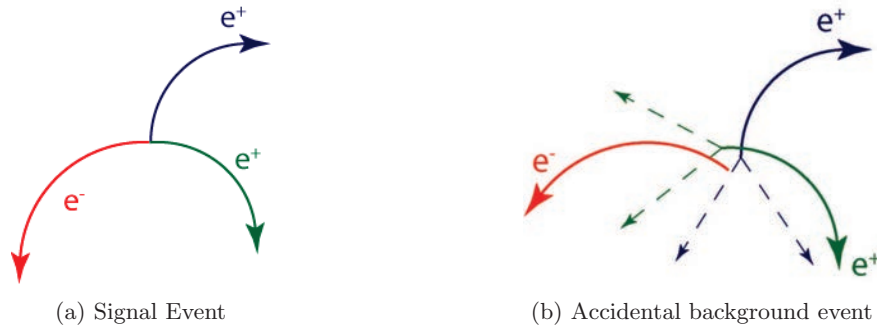(a) Signal Event   (b) Accidental background event

Figure 2.6: Schematic comparison of (a) the Mu3e signal event and (b) an accidental background event of two Michel decays with an additional electron

2.3   The Mu3e Detector

2.3.1   Experimental Concept

The goal of the Mu3e detector is to search for the decay $\mu^+ \to e^+e^+e^-$ with sensitivity at a level of 10^{-16}. In order to archive the goal, it is required to run at high muon decay rate, with a precise momentum resolution for the suppression of background from internal conversion decay $\mu^+ \to e^+e^+e^-\nu_e\overline{\nu}_\mu$. In addition a good timing and vertex resolution for the suppression of accidental background is required. Moreover, with the electron energy below 53 MeV, multiple Coulomb scattering in detector material is the dominating limitation to the momentum resolution . Therefore, a design with low material budget in the active part of the detector is desired.

A high rate muon beam is stop on a double cone Mylar target. The Mu3e detector mainly consists of a ultra thin pixel tracker, implemented in High Voltage Monolithic Active Pixel Sensors (HV-MAPS). The momentum measurement is done by HV-MAPS in a B = 1T solenoidal magnetic field. A cylindrical station with two double layers, in total four HV-MAPS layers, is located along the beam-line and surrounding the Mylar target. In order to provide precise momentum measurements with the help of re-curling electrons (positrons), the outer two HV-MAPS layers are extended upstream and downstream to form recurl station on each end of the central station. To provide precise time measurements, timing systems are placed under the outer layers of each station, a scintillating fiber detector in the central station and a scintillating tiles detector in each of the recurl station. The complete detector is approximately 2m long. The schematic views of the detector can be found on Figure 2.9 and 2.10.

The detector is completed in three phases. In the first phase Ia, a minimum configuration with only the aluminum target surrounded by the inner and outer double pixel sensor layers are constructed, see figure 2.7. By the use of an existing beam line at PSI providing a muon stopping rate at around $2 \cdot 10^7$Hz, this configuration will allow a competitive measurement with a sensitivity down to $\mathcal{O}(10^{-14})$. In the next phase Ib, a pair of recurl station, the corresponding tile detectors and the fiber tracker would be added to the configuration, see figure 2.8. With the help of the recurl station, the momentum resolution is significantly enhanced such that the suppression of internal conversion background would improve. The new timing system improves the suppression of accidental background further and allow measurement at a higher muon decay rate around $1 \cdot 10^8$Hz. The sensitivity to the branching ratio is expected to reach $\mathcal{O}(10^{-15})$ and be limited by the muon decay rate. In the final phase II, a new high intensity muon beam line delivering muons at a maximum rate of $2 \cdot 10^9 muons/second$ [19] has to be used. To cope with the high muon stopping rate, the detector is completed by adding a second pair of recurl stations with tile detectors, see figure 2.9. The improvement in momentum and timing resolution together with the increase of muon stopping rate pushes the sensitivity to $\text{Br}(\mu \to e^+e^-e^+) \leq 10^{-16}$.
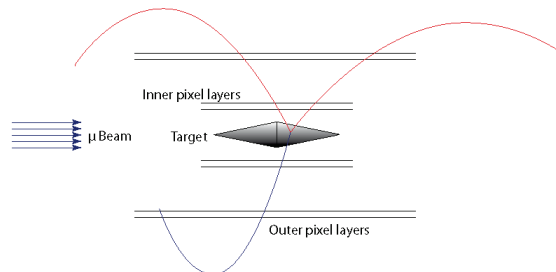
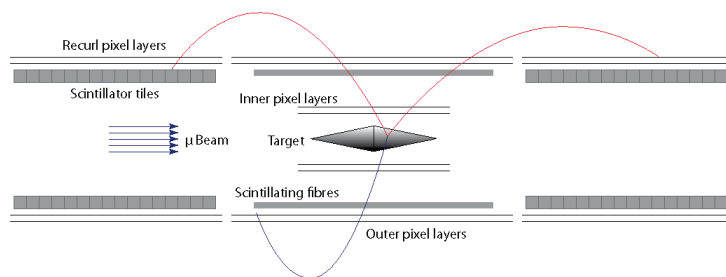Figure 2.7: Schematic view of the experiment cut along the beam axis in the phase Ia configuration

Figure 2.8: Schematic view of the experiment cut along the beam axis in the phase Ib configuration
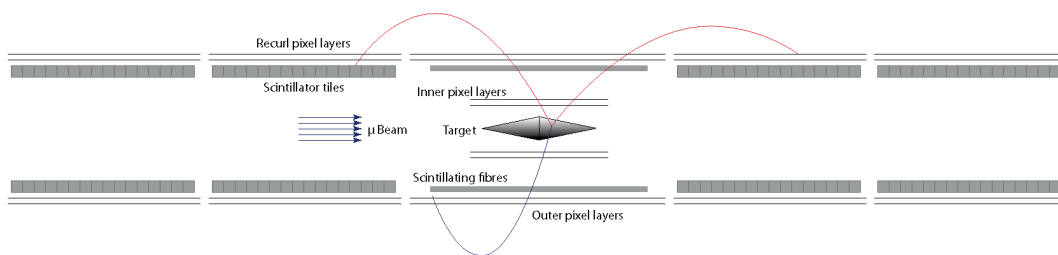

Figure 2.9: Schematic view of the experiment cut along the beam axis in the phase II configuration
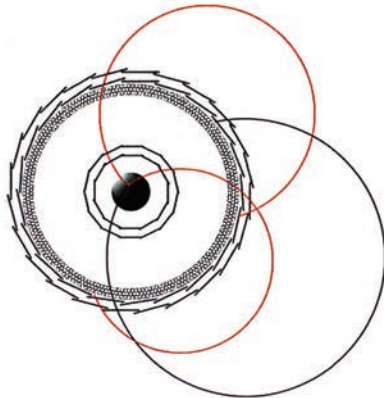
Figure 2.10: Schematic view of the experiment cut transverse to the beam axis. Fibers not drawn to scale

2.3.2 Pixel Detector

Due to the requirement of low material budget for minimization of multiple coulomb scattering and fast read out rate for high muon decay rates, the Mu3e detector makes use of the High Voltage Monolithic Active Pixel Sensor (HV-MAPS). The design of HV-MAPS integrates all readout electronics and the pixel sensor on the same chip, providing an excellent timing resolution with minimal material. HV-MAPS can be thinned to $50\mu m$. All together with a flex-print cable and a Kapton® support structure[2],it gives a thickness of 0.1% to the radiation length, see table 2.1. A sketch for the assembly of the component is illustrated in figure 2.11.
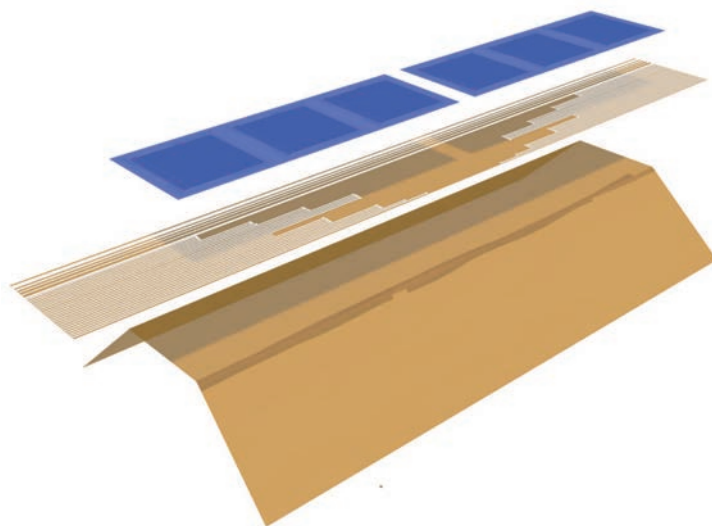

Figure 2.11: Sketch of the basic component for pixel detector

---

[2]Detail in chapter 3.1

Component	Tickness [μ m]	$x/X_0[\%]$
Support structure	25	0.009
Flex-print	25	0.009
Aluminum traces	12	0.013
HV-MAPS	50	0.053
Adhesive	10	0.003
Full layer	122	0.087

Table 2.1: radiation length $\frac{x}{X_0}$ for the individual components of one pixel tracker layer

High Voltage Monolithic Active Pixel Sensor (HV-MAPS)

The classical concepts of hybrid designs of silicon sensors usually lead to high material budget due to the additional interconnection and extra readout electronics, which eventually compromise the track reconstruction performance especially at low track momentum. For HV-MAPS, the pixel cells are designed in a smart diode structure [21], such that the pixel electronics, e.g. the charge sensitive amplifier (CSA), is integrated in the sensor chip n-well. These deep n-wells in a p-doped substrate are reversely biased to act as a signal collecting electrode for charge generated by the ionizing particle in the depletion zone. By arranging such smart diode close to each other, called Smart Diode Array (SDA), a pixel sensor with close to 100% fill-factor can be built. A sketch of the HVMAPS design is shown in Figure 2.12. Since the depletion zone is only $9\mu m$, the HV-MAPS can be thinned down to $50\mu m$. In contrast to ordinary MAPS designs, which collects ionization charges mainly by diffusion with a timing constant of several hundreds of nanosecond, HV-MAPS collects charges via drift by the use of a high bias voltage exceeding 50V [3]. This design gives a timing resolution better than 10ns. Besides, the design of HV-MAPS makes it highly tolerant to radiation damage. Radiation test of the HV-MAPS sensor [22] indicate that no radiation damage is expected even at highest muon rates at phase II. The power consumption of HV-MAPS is expected to be 250 - 400 mW/cm^2.

The HV-MAPS can be implemented in a commerical HV-CMOS process, which will be long-term available in industry. Hence, the cost of production is low.

The HV-MAPS chip designed specifically for the Mu3e experiment is named MuPix. Studies for characterization of several Mupix prototype have been carried out [3][4][5]. With the MuPix6 prototype a power consumption of $223mW/cm^2$ and an operation temperature at 0 - 70 °C has been validated.
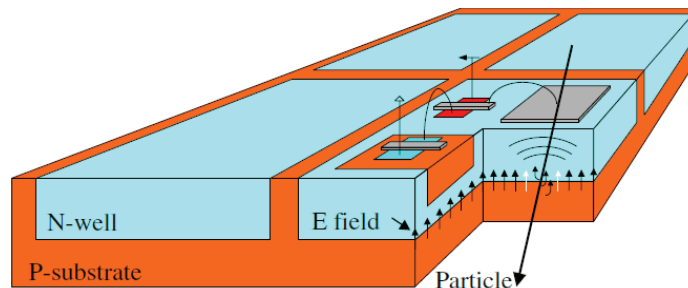

Figure 2.12: Sketch of the MAPS detector design [20]

Figure 2.13: A 50μm thin silicon wafer

2.3.3 Time of Flight Detector

The main concept of the Mu3e time of flight system is to measure precisely the time of arrival for particles in order to allow for the matching with hits detected in the pixel sensor. This improves the time resolution and hence help rejecting accidental events. The system consists of two components, a scintillating fiber detector and four scintillating tiles detectors. The scintillating fiber detector is located in the central detector station and gives a timing resolution of 1 ns. The scintillating tile detectors are located in each recurl detector station and gives a timing resolution of 100 ps. Both detector are placed right under the outer double sensor layer.

Fiber Detector

The scintillation fiber detector is composed of 24 scintillating fiber ribbons, each 30 cm long and 16 mm wide, as shown in figure 2.14. As the fiber detector is located in the central detector station, i.e. the highly active region, a design for minimal material budget has to be considered in order to reduce the multiple coulomb scattering, while providing high time resolution. Therefore 3 layers of scintillating fibers with 250μm diameter are used. The fiber ribbons are supported by a Kapton® mechanical structure. The emitted signals are detected by SiPM arrays which are located at both ends of the ribbons. SiPMs are compact photo-detector device that can be operated in high magnetic fields with high gain and high counting rates. The scintillation fiber detector is expected to give a timing resolution below 1ns.

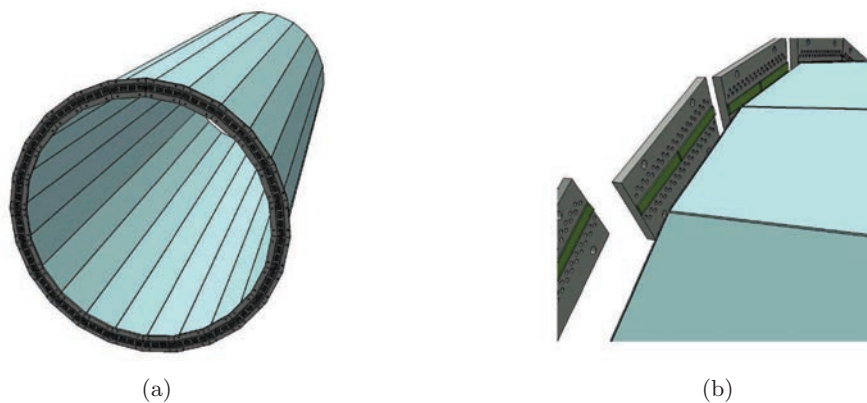(a)   (b)

Figure 2.14: (a) The drawing of the scintillating fiber barrel for the central time of flight detector. (b) SiPM supports for the scintillating fiber arrays

Tile Detector

The second component of the time of flight system is the scintillating tile detector, see figure 8.12. The detector is aimed at a time resolution below 100 ps and an efficiency close to 100 % in order to effectively identify signal and reject accidental background. As there is no interest in the particle after traversing the tile detector, the design can focus on optimization in time resolution instead of minimization in material budget. Therefore thick tiles with a size of 7.5 x 7.5 x 5 mm are used in the detector. The tiles are assembled together to form a module with length of 36cm, diameter of about 12 cm and thickness of 5mm. There are 4 stations of tile detectors and each of them is located in each of the recurl station under the outer HV-MAPS double layer. Silicon Photomultipliers (SiPM) are used for signal read out and attached on the inner side of each tile.
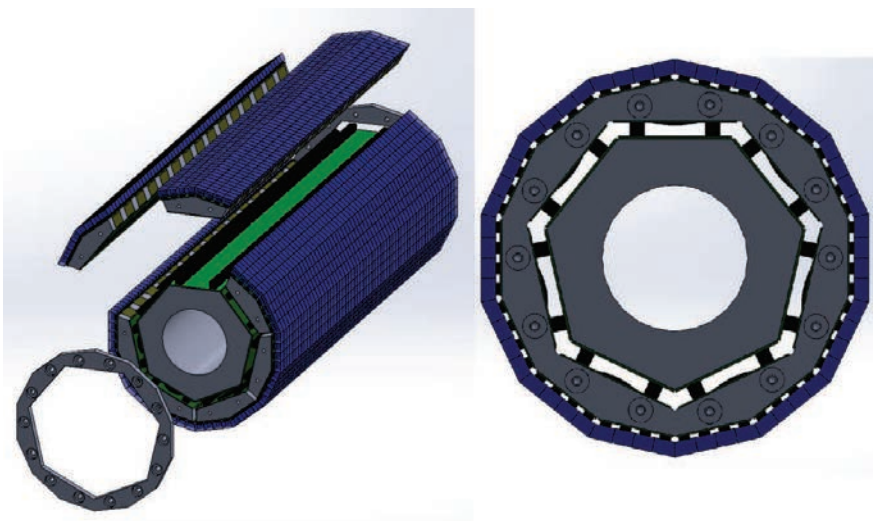

Figure 2.15: Drawing of the tile detector

2.3.4 Data Acquisition

The Mu3e data acquisition system works without a hardware trigger, i.e. the detector elements continuously send hit information to the data acquisition (DAQ) system. The DAQ consists of three layers, the front-end FPGAs, switching boards and the filter farm. Figure 2.16 shows the readout scheme for the Mu3e experiment. The detector first sends data rates in order of 1 Tbit/s to the front-end FPGAs, which are located on the beam pipe. The detector information is passed to the PCs of the filter farm where the event is reconstructed online. Selected events are sent to the data collection server at a rate of 50 MByte/s and then written into a mass storage system.
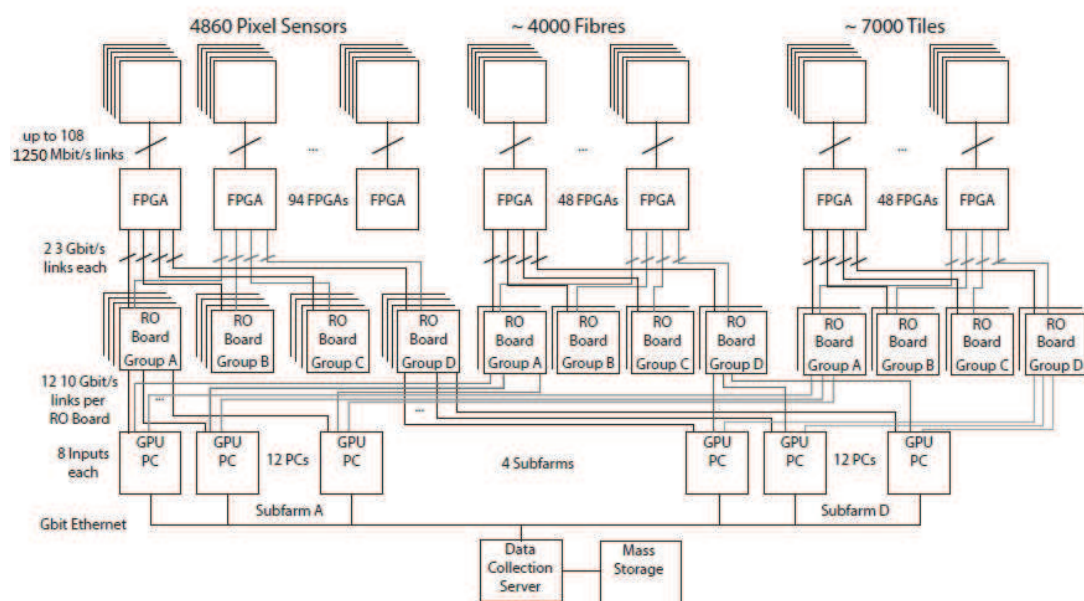
Figure 2.16: Mu3e readout scheme

Chapter 3

Cooling system of the Mu3e Detector

According to the characterization of the Mupix6 sensor, the power consumption of this HV-MAPS is expected to be 223mW/cm^{-2} [3]. The total power consumption for the outer layer is expected to be about 890W per station and for inner layer about 90W. Additionally, each of the front-end FPGA located along the surface of the beam pipe consumes a power of 25W, approximately 1400W in total. All together, a cooling system for 4000W is required in order to keep the temperature of sensors below 70 °C, which is the maximum working temperature for Mupix sensor [4].

It is a challenge for the design of a cooling system to provide enough cooling power while keeping the material budget minimal, in order to reduce multiple coulomb scattering which leads to a decrease of the momentum resolution. Therefore, the concept of the cooling system is to use gaseous helium cooling on silicon detector stations plus water cooling for the front-end FPGAs on the beam pipe. Gaseous helium is chosen as coolant due to its low atomic number and good cooling ability. The radiation length $\frac{x}{X_0}$ on a helium layer of 1 meter thickness is approximately 0.019%, which is much lower than for nitrogen [1]. The helium cooling system is separated into two channels, a Global Flow channel thoughout the acceptance region of the detector and a Local Flow channel through the V-shaped supporting structure located right under each sensor segment. Details of the design are discussed in section 3.1. The water cooling system is integrated into the beam pipe and water is running in pipes under the FPGA chips. The temperature of both coolants is selected to be slightly above 0 °C in order to prevent icing problems for both water cooling system and moisture in detector.

In order to verify the design concept, a series of tests with heatable detector model have been carried out.[2][6][7], a detailed description can be found in section 3.2.

3.1 Mechanical Design

The Mechanical Design of the Mu3e detector is aimed at low material budget, at the same time providing mechanical stability, temperature tolerance and easy assembly and maintenance. The HV-MAPS detector station is based on a frame made of Kapton® foil and milled pie end-structure.

---

[1]Radiation length for 1m thick nitrogen layer $\frac{x}{X_0} \sim 0.3\%$.

The pixel sensors are glued and bonded on a flex-print and then mounted on the frame.

The Kapton® used for the frame is 25 μm thin. An 25μm aluminum foil is glued on the Kapton® and the circuits for sensor bonding are lasered out. To provide mechanical stability, an extra 25 μm Kapton ® foil is folded in a V-shaped template and glued right under the frame ,see figure 2.11. It acts as a supporting structure to the frame and provides an extra gas flow channel for the cooling system. The Kapton® segment is then glued on a plastic end-piece, see figure 3.2. Each pair of end-piece is combined with 4 sensor segments and forms a module, see figure 3.1. A specialized assembling tool is built for the construction of the module. Figure 3.3 shows the assembly tool for the bonding of the frame and the end-piece ; figure 3.4 shows the tool for the shaping of supporting V-shaped structure. The 50 μm pixel sensors are glued on the Kapton® flex print to the correct position by an alignment tool and then bonded to the circuits on the flex print. Due to the digital readout circuits of the pixel chips, there is an approximately 0.5 mm width dead zone. Therefore, the sensors are assembled with a 1mm overlap to the adjacent sensor. The modules are then mounted together to form the detector station. Disassembly of each module is possible for maintenance.

The detector is made up of 4 different layers of HV-MAPS, see figure 2.10. The innermost layer is labeled as the first layer and accordingly the outermost as the fourth layer. The outer double layer are the layer 3 and 4, and the inner double layer are the layer 1 and 2. The outer layers 3 and 4 have an active length of 36cm. The width of the sensor segment is 20mm, with a dead zone of approximately 0.5 mm as mentioned above. The layer 3 and 4 have 24 and 28 sensors segments. 4 sensor segments are glued on one end-piece, layer 3 consists of 6 modules while layer 4 consists of 7. The inner detector station is much smaller and shorter than the outer layer. For inner layer 1 and 2, the active region of the sensor segment is only 12cm long with a width of 20mm. Layer 1 and 2 have 8 and 10 sensors segments. The segments of each layer are glued on supporting endrings. As opposed to the outer layer segment, the V-shape fold in the Kapton® support structure is not foreseen. Therefore, a specialized assembly tool is also designed for the construction of inner detector, see figure 3.5. A prototype model of the inner detector station is shown on figure 3.6. Despite the absence of V-shape folds, the structure still provides enough mechanical stability to the station.

Figure 3.1: Mechanical prototype of a layer 3 module

Figure 3.2: Kapton foil with supporting structure glued on an end-piece

Figure 3.3: Assembly tool for outer layer modules

Figure 3.4: Assembly tool for the supporting structure of the layer 3

Figure 3.5: Assembly tool for the inner layer prototype

Figure 3.6: A mechanical prototype of the inner detector station, with sensor layer 1 and 2

The Cooling System

The cooling system is designed for a heat disposal of about 4000W from electronics on the the detector. The schematic of the cooling systems can be found on figure 3.7.

The helium cooling system uses gaseous helium at 0°C as coolant. Helium is a good choice due to its low atomic number which leads to a long radiation length and eventually reduces multiple coulomb scattering. The helium gas system is designed for the heat disposal of approximately 900W per station. The system is separated into two channels, Global Flow channel and Local Flow channel. The Global Flow channel applies gaseous helium flow on the outer drift volume of the detector. The detector is contained in a long cylindrical barrel filled with gaseous helium. Flow is applied from one of the ends of the barrel and the heated helium leaves the barrel on the other end. As mentioned in the mechanical design of the Kapton® frame, the V-shaped fold for the supporting structure not only provides mechanical stability, but also a gas flow channel. To make use of this structure, gaseous helium is applied by a gas distribution system to this channel in opposite direction of the global flow channel. This flow channel is named Local Flow channel. It provides extra cooling power under each sensor segments and helps effectively to cool the sensor [2].

As the front end FPGAs are located in the inactive region along the beam line, multiple coulomb scattering inside this system does not affect the resolution of the measurement. Therefore, the design of the FPGA cooling system does not have to focus on the low material budget. For this reason, the usage of a thermal heat sink with active water cooling is allowed. The water cooling system is integrated into the muon beam pipe. Thermal heat sinks with water pipes inside are installed along the beam pipe perimeter. The use of steel with copper in the contact area is proposed. A mechanical model of the preliminary design is shown in figure 3.8 The water pipes are located in the U-shaped gaps on each heat sink. Water with temperature slightly above 0 °C is running through inside of the heat sink. The FPGAs are aligned in a row on the heat sinks. The power consumption of each front end FPGA chip is expected to be below 25W. Each heat sink is populated with 8

FPGAs and generates a heating power up to 200W. There are 7 rows of FPGAs and the total heating power is up to1400W per station.
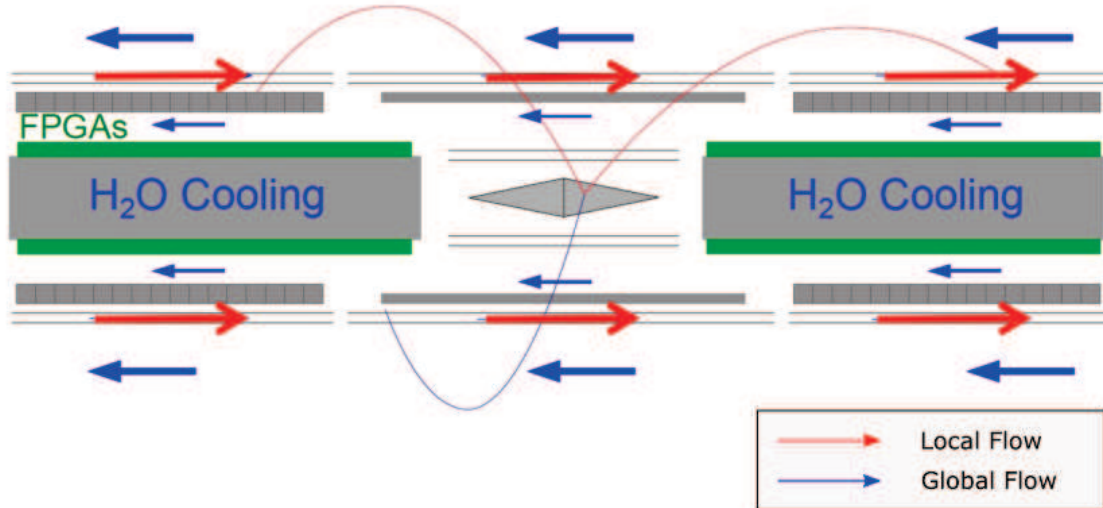

Figure 3.7: Schematic for the cooling system of Mu3e detector [2]

Figure 3.8: 3D printed model for the preliminary design of the water cooling system

3.2   Test of the Cooling System

In order to investigate the concept of the cooling system, tests have been carried out on a heatable detector model [2] [6] [7]. Temperature profiles for both helium and water cooling are measured under varied condition. Results are found within the specification.

Helium Cooling system for the Pixel Detector

This section summaries the tests on the helium cooling system, see thesis of Andrian Herkert [2]. An ohmic heatable model prototype was built for the cooling test. The model follows the detector design but only one module of layer 3 and 4 was installed. The geometry of the model is similar to the real detector and contains local flow channels. The model is made up of 25μm Kapton® foil

(a)   (b)
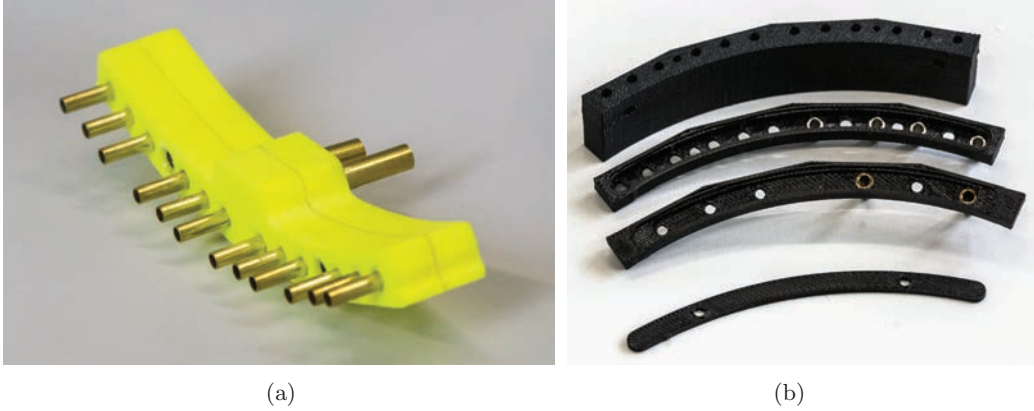
Figure 3.9: (a) end-piece for helium coolant inlet (b) end-piece before assembly

laminated with 12μm Aluminum foil. The model is built with the assembling tools mentioned in section 3.1. Ohmic heating circuits are lasered on the surface of the sensor segment. Thin glass plates of 50μm are glued on the surface to model the pixel sensor chips. Under the sensor segment, the same aluminum Kapton® foil is used to construct the supporting structure. This supporting V-shaped provide a flow channel for local cooling.

A wind tunnel with mechanical frame and ventilation system for the module is built for the test, see figure 3.10. The heatable module is mounted on the mechanical frame in the tunnel. The ventilation system consists of two 22cm diameter computer fans, located at both ends of the tunnel. The system provides gaseous coolant flow into the tunnel as global flow. Holes are drilled on the surface of the tunnel for gas inlets of the local flow channel. The gaseous inlets are connected by gas tubes to the inlet end-pieces at both ends of the module. They provide gaseous helium coolant flow to the local channel and guide out the heated coolant. During the test, the whole tunnel with the heatable model is contained in a chamber filled with gaseous helium. Although the idea is to use helium at $0°C$ as coolant, it is hard to keep the helium at such temperature in normal laboratory environment. Therefore, the model is tested with helium at 20°C. Water cooled radiators for computer cooling are placed inside and outside the gaseous container to maintain the temperature of helium. The schematic of the setup for the helium cooling test is shown on figure 3.11. Pt1000 resistance thermometer are attached on the surface of the module. The sensors are align in a row on both layer.

Measurements were carried out at different heating power and variable flow. The results are plotted in figure 3.12 and 3.13. The horizontal axis shows the position of the temperature sensor along the detector module. The global helium flow comes from the right and the local helium flow from the left. The vertical axis shows the relative temperature ΔT. ΔT denotes the difference between the temperature of the sensor T and the temperature of the helium coolant T_0 :

$$\Delta T = T - T_0 \tag{3.1}$$

Figure 3.12 shows the plot for the temperature profile with the expected power consumption 250 mW/cm^2. In this test, a flow velocity of 2.3 m/s was applied to the global cooling channel and 20 m/s in the local cooling channel. A maximum relative temperature of about 30 °C is found in the center region on layer 4. The temperature of layer 4 is found higher than for layer 3. It lies within the MuPix temperature operating range of 70 upto °C. The module is also tested with heating

power of 400mW/cm^2, which is about 60% higher than the expected power consumption. Figure 3.13 shows the plot for the temperature profile with the a consumption 400mW/cm^2. In this test, a flow velocity of 2.5 m/s was applied to the global cooling channel and 20m/s in the local cooling channel. The temperature difference between layer 3 and 4 becomes more significant. Layer 4 has a maximum temperature of approximately 52°C. On Layer 3 it is 43°C, which is 9°C lower. The result is still below the upper limit of the operating temperature, assuming $T = 0°C$ helium at the inlet.
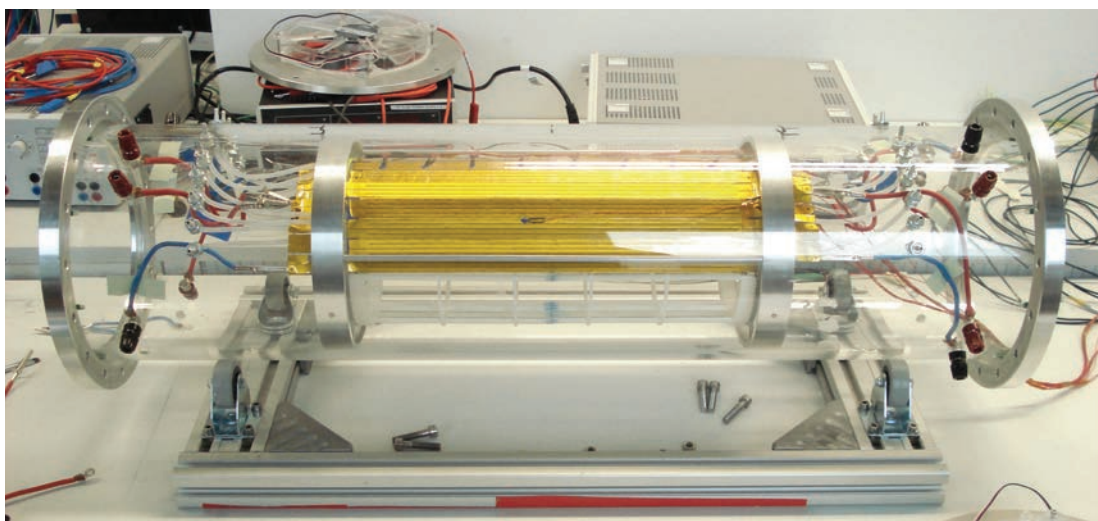
Figure 3.10: Setup for the hellium cooling test [2]
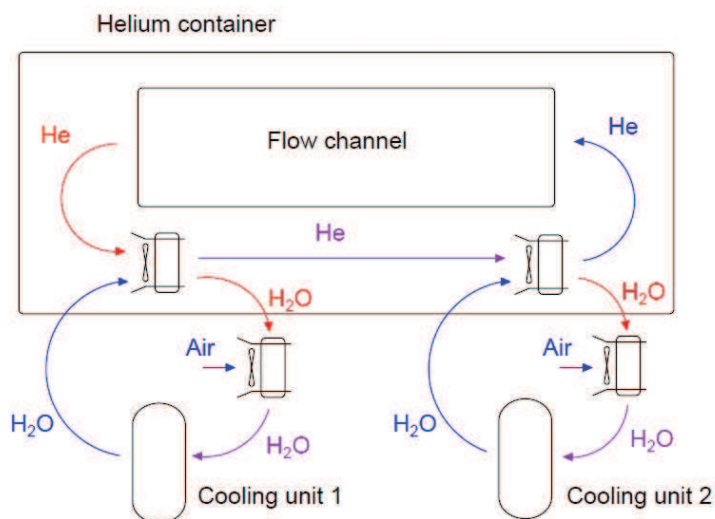
Figure 3.11: schematic of the setup for the cooling test [2]
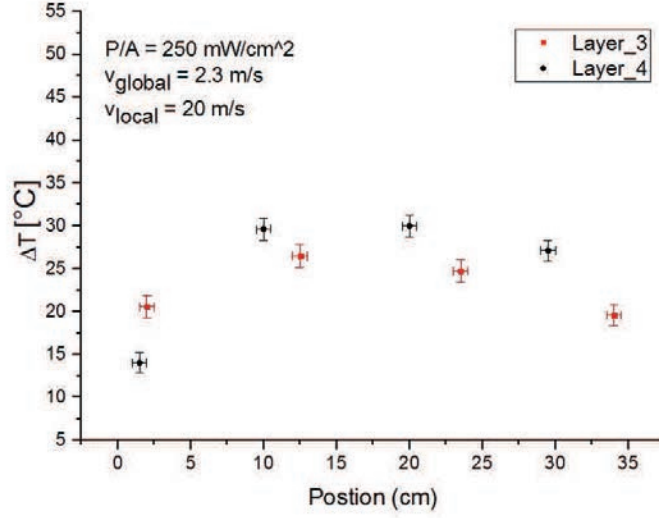
Figure 3.12: Temperature profile of layer 3 and 4 at power consumption of 250mW/cm^{-2} with $v_{global} = 2.3 \pm 0.2 m/s$ from the left and $v_{local} = 20 \pm 1 m/s$ from the right [2]
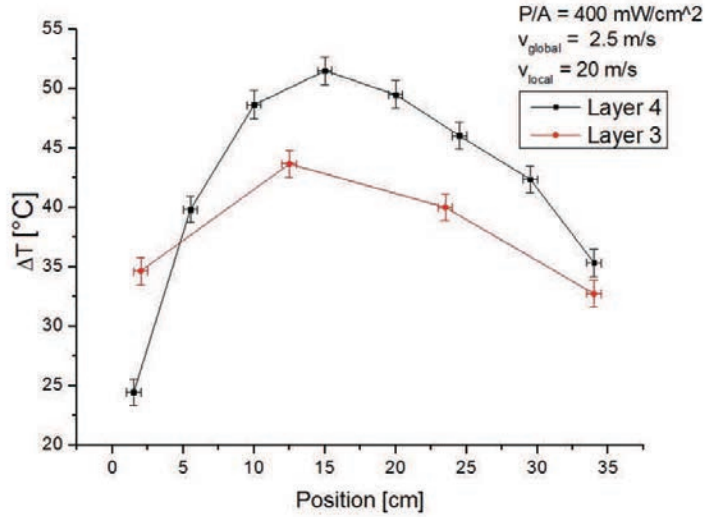
Figure 3.13: Temperature profile of layer 3 and 4 at power consumption of 400mW/cm^{-2} with $v_{global} = 2.5 \pm 0.2 m/s$ from the left and $v_{local} = 20 \pm 1 m/s$ from the right [2]

Beam-line Water Cooling System

A prototype of the thermal heat sink for the beam line water cooling system has been built. Only part of the heat sink is built to test for the cooling ability. The heat sink is mounted with 4 heating resistors to simulate the heating effect of the front-end FPGA chips. Four Pt1000 resistance thermometers are attached on top of the heating resistor for temperature measurement. Water coolant at 20 °C was applied through the heat sink. The measurement was carried out after the system has reached thermal equilibrium. Heating power is applied on the heating resistor ranging from 100W to 300W in total. A plot of the measured temperature profile from the measurement is shown on figure 3.15. The water temperature in the cooling device raised for 2 - 4 °C after reaching thermal equilibrium, depending on the heating power.
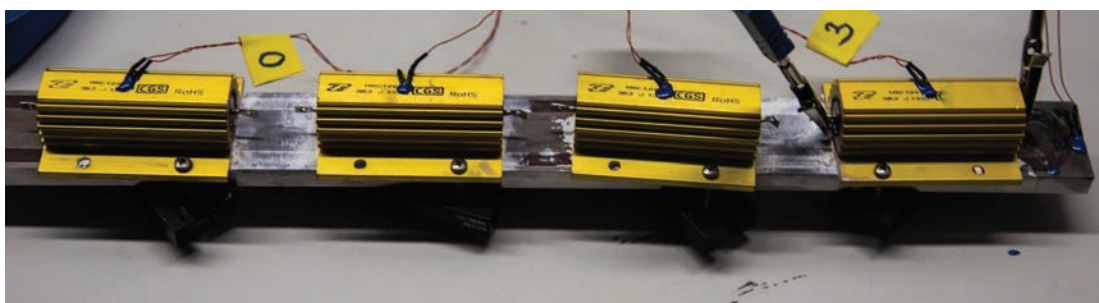
Figure 3.14: Setup for the water cooling test on beamline heat sink prototype
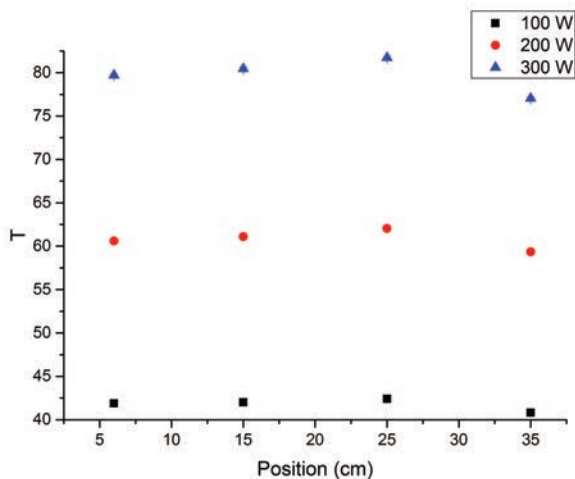
Figure 3.15: Temperature profile of the water-cooled heat sink on beam line with different heating power, $T_{water} = 20°C$

Chapter 4

Finite Element Analysis

Finite Element Analysis (FEA), also called Finite Element Method (FEM) is a numerical technique for finding approximate solution to field problems, which requires the spatial distribution of one or more dependent variables. For instance the problem can be the distribution of temperature of a heat engine, or deformation and stresses of a spring, or the velocity of fluid in a pipe. Mathematically speaking, a field problem can be described by differential equations or by integral equations which are used in finite element formulation. FEA splits up the complex field problem into a number of simpler ones by discretizing a domain into a finite number of individual sub-domains, named finite elements. The elements are connected to adjacent elements at points called nodes, and assembled to form a finite element structure, called a mesh. Each nodal unknown is the value of the field quantity and depends on the mathematical model. To obtain the solution to the unknown variables, the governing partial differential equation is broken into a set of algebraic equations at the nodes. In each finite element the field quantity is restrained in a simple spatial variation, described by polynomial terms up to second order. The solution of each quantities are combined together to determine the spatial variation of the field in that element. In other words the field quantities over the entire structure is approximated element by element. Although the solution of FEA is not exact, it can be improved by increasing the amount of elements to represent the structure.

FEA has advantages over most other numerical analysis method, in terms of versatility and physical appeal [24]:

- Applicable to any field problem, such as heat transfer, fluid flow, stress analysis, magnetic field, etc.

- No geometric restriction

- Boundary conditions are not restricted on a body

- Material properties are not restricted to isotropy

- Element types are not restricted in single model

- Actual body can be closely resembled by FE structure.

- Accuracy can be improved by grading the mesh

Simulation with Finite Element Method

Solving a practical problem by FEA involves problem learning, mathematical modeling, model discretization, computational calculation, and result verification [24]. In order to optimize the result, more than one cycle through these steps is generally required. The stages for simulation by finite element analysis are outlined in figure 4.1.

Problem Classification

The first step in solving a problem is to identify it. Without this step a proper model cannot be devised, nor can FEA software be told what to do. The identification of the objective generally involves the geometry, material, ambient condition, physical nature and so on. On the computation side, one ought to determine the required accuracy, format of result, iterative method and so on.

Mathematical Modeling

In FEA, an analytical method is applied to a model problem rather than to an actual physical problem. Therefore, a model for analysis with the capability to represent the physical nature and structure of the problem is need. In modeling, one must aim to exclude superfluous details but include all essential features, so that the analysis of the model is not unnecessarily complicated yet provides results that describe the actual problem with sufficient accuracy. The geometry model then becomes a mathematical problem with its behavior described by selected differential equations and boundary conditions. Because the mathematical modeling is only an approximation to the real problem, modeling errors are reducible but unavoidable. Therefore, modeling decisions are influenced by the information sought, the accuracy required, the anticipated expense of FEA, and its capabilities and limitations. Usually, initial modeling decisions are provisional. It is likely that result from first FE simulation will suggest refinements in geometry or applicable theory and so on.

Preliminary Analysis

Before going from a mathematical model to FE simulation, a preliminary solution should be obtained for the prediction of a result, and may even lead to a better mathematical model. It can be a simple analytical calculation, handbook formulas, trusted previous solution or experiment. Subsequently it will be used for the verification of the computational result.

Finite Element Simulation

FE simulation generally involve three step, preprocessing, numerical analysis and postprocessing. In preprocessing, geometry data, material, loads and boundary condition have to been input. With the selected element type and mesh density, the discretization of the model can be done automatically by the software. As the generated discrete mesh is a representation of a fully continuous field, it introduces the discretization error. Therefore, one must choose the suitable element formulation to the mathematical model, and also the size of the element in the FE model. The numerical analysis is carried out by software. Matrices that describe the behavior of each element are generated automatically. The combination of these matrices forms large matrix equations representing the FE structure. The field quantities at nodes can be obtained by solving the equations. The postprocessing is the step to illustrate the FE simulated result. This step is also carried out automatically, except that the analyst must instruct the software to select right format for result, such as the required physical quantities, method of display, etc.

Verification and Optimization

The next step of the simulation is to verify the result. The result can be examined in few aspects, such as convergence of the solution, misrepresented boundary conditions, abnormal quantities, etc. If the results are satisfactory, they can be compared with the solution from the preliminary analysis, and with any other useful information that may be available. An optimization can be considered after evaluating the simulated result.
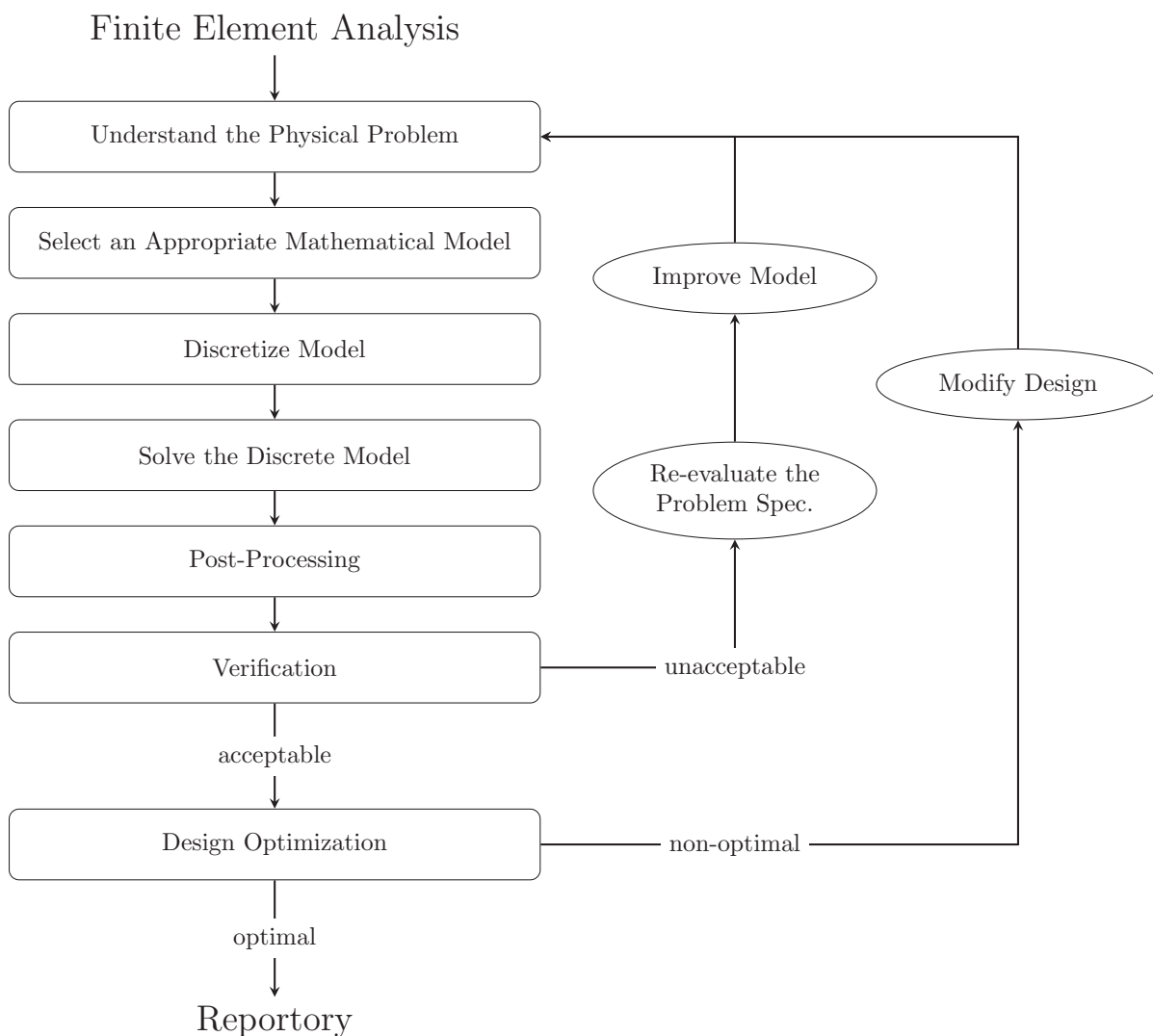
Finite Element Analysis

Understand the Physical Problem

Select an Appropriate Mathematical Model

Discretize Model

Solve the Discrete Model

Post-Processing

Verification

acceptable

Design Optimization

optimal

Reportory

Improve Model

Re-evaluate the Problem Spec.

Modify Design

unacceptable

non-optimal

Figure 4.1: Procedure for finite element analysis

Autodesk® Computational Fluid Dynamics

Computational Fluid Dynamics (CFD) is a branch of fluid mechanics using numerical analysis and algorithms to solve and analyze problems that involve fluid flow. Computers are used to perform the calculation for simulating the interaction of fluids constrained by boundary condition. Various discretization methods can be used to carry out the computational analysis, such as Finite Difference Method, Finite Volume Method and Finite Element Method. In the Autodesk® CFD, the program makes use of the Finite Element Method. The method is capable of predicting both laminar and turbulent flows and provides high flexibility and accuracy in treating complicated geometries. Streamline upwind approximation is used for discretization of the governing equations [26]. This approximation significantly reduces the numerical diffusion error, with a straightforward and computationally inexpensive implementation. Iterative matrix solvers are used to solve the matrix formed by the discretized algebraic equations at every node. The Tri-Diagonal Matrix Algorithm (TDMA)[27], a simplified form of Gaussian elimination, complemented with the Gauss-Seidel method [28] is used in Autodesk® CFD. Solution are obtained by post-processing the solved nodal unknown.

Governing Equations

The governing equation for heat transfer and fluid flow are the Navior Stokes momentum equation and the energy equation from the first law of thermodynamics. The governing partial differential equations of momentum for incompressible laminar flow in x, y, z direction with velocity u, v, w can be written as [25]:

Continuity Equation

$$\frac{\partial \rho}{\partial t} + \frac{\partial \rho u}{\partial x} + \frac{\partial \rho v}{\partial y} + \frac{\partial \rho w}{\partial z} = 0 \tag{4.1}$$

X-Momentum Equation

$$\rho \frac{\partial u}{\partial t} + \rho u \frac{\partial u}{\partial x} + \rho V \frac{\partial u}{\partial y} + \rho W \frac{\partial u}{\partial z} = \rho g_x - \frac{\partial p}{\partial x} + S_{DR} + S_\omega$$
$$+ \frac{\partial}{\partial x}\left[2\mu \frac{\partial u}{\partial x}\right] + \frac{\partial}{\partial y}\left[\mu\left(\frac{\partial u}{\partial y} + \frac{\partial v}{\partial x}\right)\right] + \frac{\partial}{\partial z}\left[\mu\left(\frac{\partial u}{\partial z} + \frac{\partial u}{\partial x}\right)\right] \tag{4.2}$$

Y-Momentum Equation

$$\rho \frac{\partial v}{\partial t} + \rho u \frac{\partial v}{\partial x} + \rho V \frac{\partial v}{\partial y} + \rho W \frac{\partial v}{\partial z} = \rho g_z - \frac{\partial p}{\partial y} + S_{DR} + S_\omega$$
$$+ \frac{\partial}{\partial x}\left[\mu\left(\frac{\partial u}{\partial y} + \frac{\partial v}{\partial x}\right)\right] + \frac{\partial}{\partial y}\left[2\mu \frac{\partial v}{\partial y}\right] + \frac{\partial}{\partial z}\left[\mu\left(\frac{\partial v}{\partial z} + \frac{\partial w}{\partial y}\right)\right] \tag{4.3}$$

Z-Momentum Equation

$$\rho \frac{\partial w}{\partial t} + \rho U \frac{\partial w}{\partial x} + \rho V \frac{\partial w}{\partial y} + \rho W \frac{\partial w}{\partial z} = \rho g_z - \frac{\partial p}{\partial z} + S_{DR} + S_\omega$$
$$+ \frac{\partial}{\partial x}\left[\mu\left(\frac{\partial u}{\partial z} + \frac{\partial w}{\partial x}\right)\right] + \frac{\partial}{\partial y}\left[\mu\left(\frac{\partial v}{\partial z} + \frac{\partial w}{\partial y}\right)\right] + \frac{\partial}{\partial z}]\left[2\mu \frac{\partial w}{\partial z}\right] \tag{4.4}$$

where ρ is the fluid density, p is the pressure, μ is the dynamic viscosity, and $g_{x,y,z}$ is the gravitational acceleration in x,y,z directions. S_{DR} and S_ω are the source term for distributed

resistance and rotation coordinates. The distributed resistance term can be written in general as :

$$S_{DR} = - \left(K_i + \frac{f}{D_H} \right) \frac{\rho v_i^{\,2}}{2} - \mu C v_i \tag{4.5}$$

where i refers to the global coordinate direction ($v_{x,y,z} = u, v, w$), f is the friction factor, D_H is the hydraulic diameter and C is the permeability. The K-factor terms K_i is the constant loss coefficient for pressure along each coordinate direction. The source term for rotation coordinates is

$$S_\omega = -2\rho\omega_i \times v_i - \rho\omega_i \times \omega_i \times r_i \tag{4.6}$$

where i refers to the global coordinate direction, ω is the rotational speed and r is the distance from the axis of rotation.

The governing partial differential equations of energy can be written as :

Energy Equation

$$\rho c_p \frac{\partial T}{\partial t} + \rho c_p u \frac{\partial T}{\partial x} + \rho c_p v \frac{\partial T}{\partial y} \rho c_p w \frac{\partial T}{\partial z} = \frac{\partial}{\partial x}\left[k\frac{\partial T}{\partial x} \right] + \frac{\partial}{\partial y}\left[k\frac{\partial T}{\partial y} \right] + \frac{\partial}{\partial z}\left[k\frac{\partial T}{\partial z} + Q_V \right] \tag{4.7}$$

where T is the temperature, c_p is the constant pressure specific heat, k is the thermal conductivity and Q_V is the volumetric heat source.

Turbulent Flow

The Navior-Stokes, continuity and energy equation can apply to laminar flow as well as turbulent flow. However, due to the infinite number of time and length scales inherent in turbulent flows, the solution of these equations requires a huge number of finite elements even for a simple geometry. As it is unreasonable to solve the model of the flow in this manner, in order to reduce the computational load, the governing equations are averaged over the scale present. In Autodesk CFD, the time-averaged governing equations is used. It is obtained by assuming that the dependent variables can be represented as a superposition of a mean value and a fluctuating value. Take the x-velocity component u as an example, it can be written as:

$$u = U + u' \tag{4.8}$$

where U is the mean velocity and u' is the fluctuation around the mean. By substituting this representation in the governing equation, the calculation for the turbulent model can be carried out. The time averaged governing equations can be found in the appendix B.

Chapter 5

Verification of the Test Measurement

As mentioned in section 3.2 , the test for the cooling system gives an satisfactory result in terms of cooling power. However, there are still questions to the actual performance of the cooling system. First of all, the test is based on a detector model with only a fraction of the outer layer. Due to the lack of adjacent module, the side transverse ends of the module form a open end, which allow exchange of heated and fresh helium coolant, providing an extra amount of cooling effect. If we consider a whole detector model with all of the modules connected, the helium flow pattern may change due to the closed structure. It is suspected that the complex flow pattern may lead to an accumulation of heat in the gap between the 2 sensor layers. Secondly, it is still unclear if a dead spot exists in the design and whether there is turbulent flow inside the station. In order to confirm the efficiency of the cooling design, it is necessary to perform a cooling test with the whole model. However, building such a model is time consuming and it is not simple for geometrical optimization. Therefore, a computational simulation for the cooling system is considered.

The software Autodesk® Inventor is used for modeling of the detector design and Autodesk® Simulation CFD is used to perform finite element analysis in fuild dynamics.

In this chapter, the modeling of the outer pixel station is discussed and simulation is carried out to verifty the test measurement in section 3.2. Different from the detector in Mu3e experent, heatable Kapton® modules is used in the cooling test to demonstrate the heating effect. With such configuration the heating location is different form the experiment. Therefore, the simulations in this chapter use this configuration in order to compare the reuslts with the measurement. The simulation with the configuration of the Mu3e experiment is discussed in the next chapter.

5.1   Modeling

To run a CFD simulation, a CAD model must first be built. Autodesk® Inventor is used for the 3D model Drawing. All of the parts of the detector are drawn separately in full scale with the design dimension and then assembled together. Simplification is applied to the model for minimization of computational load. In orderl to illustrate the performance of the exact cooling system, the drawn model is kept close to the mechanical model.

Sensor segment

The sensor module consist of three layer : the sensor, flexprint sector and the supporting layer. In the CAD model, the sensor chips are illustrated by a silicon segment with dimension of 19 x 360mm. The thickness of the silicon segment is 50μm, same as the MuPix. The flexprint with power and signal circuit are draw as a Kapton® segment. The dimension of the Kapton® segment is 19 x 390mm with thickness of 50μm. The supporting structure for the sensor is a folded Kapton® segment. The segment is folded into a V-shaped structure. The dimension of the segment is 19 x 360mm with thickness of 50μm. The V-shaped fold is a triangular channel with a equivalent triangle of 6mm. The model is shown on figure 5.1.

(a)

(b)

Figure 5.1: CAD model for the (a) Mupix sensor segment and (b) Kapton® segment with V-shaped supporting structure (also for local cooling channel)

End-Ring for Outer layer

Besides for the mechanical support and the mounting for the sensor segment, the end-pieces are also important components for the helium gas distribution system. This design consists of two parts : the supporting end-piece and gas inlet end-piece. The supporting end-piece provides a platform for gluing the Kapton® segment and a possibility of disassembly. The CAD model is shown on figure 5.2a. The end-piece is 15mm thick with a height about 5.5mm for layer 4 and 5.6mm for layer 3. To provide support for the Kapton® segment, the width of the end-piece is the same as the kapton segment, which is 19mm. The end-ring is constructed by mounting multiple end-pieces

together on a mechanical frame, six for layer 3 and seven for layer 4. The model is shown on figure 5.2b. The gas inlet end-piece is mainly responsible for distributing helium coolant into the local flow channel. The dimension of the gas inlet end-piece is similar to the supporting end-piece but with a thickness of 7.5mm. It has a rather complex structure for the gas distribution: an integrated gas distribution inlet which can provide gas flow to both the local flow channel and the gap region between layer 3 and 4. It is divided into two section with two separated chamber for the control of the flow rate. The CAD drawing of this gas inlet end-piece is shown in the figure 5.3 and the schematic for assembly is shown on figure 5.7. The drawing on figure 5.4 shows the flow pattern inside the gas distribution champer of this end-piece.

(a)

(b)
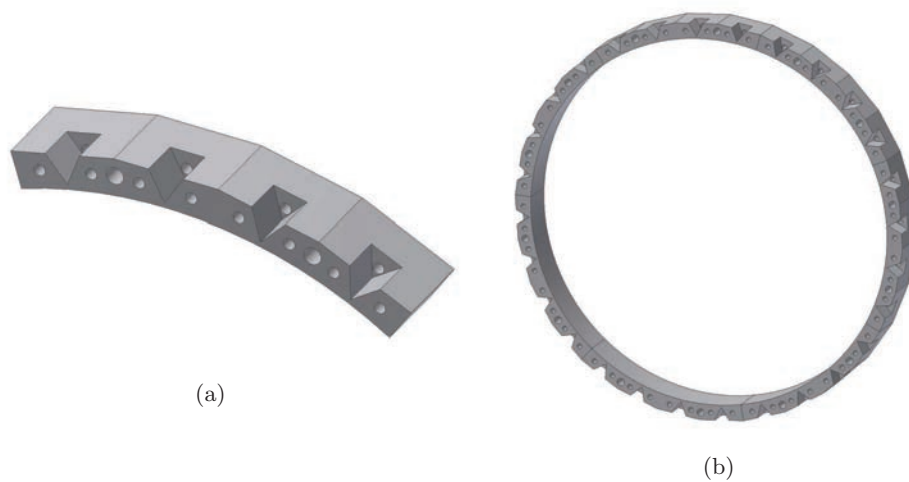
Figure 5.2: CAD model for (a) a single supporting end-piece and (b) the End-ring by assembling all end-pieces together
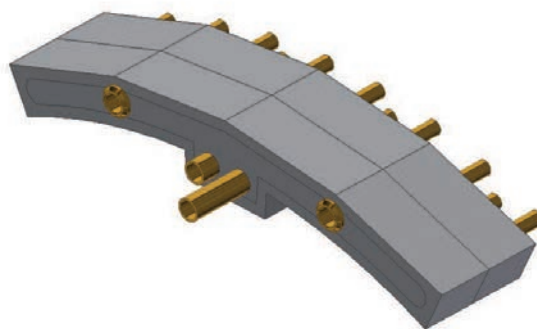
Figure 5.3: CAD model for gas distributing end-piece
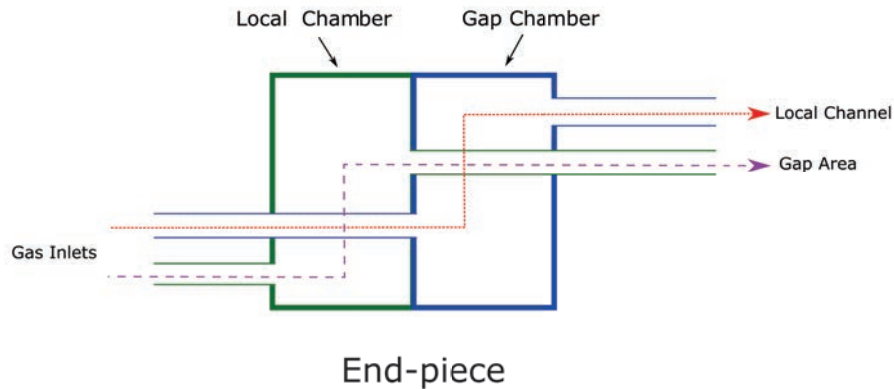
Figure 5.4: Schematics for the flow inside the gas distributing end-piece

Assembly and Simplification

As the layers of the detector station have a cylindrical symmetry, the drawn parts are duplicated and assembled to form modules. The CAD model of the single station with dimensions according to the Mu3e research proposal [1] is shown in figure 5.5. In order to optimize the computational time, part of the model is further modified.

The inlet end-piece for the helium gas distribution system is a complicated structure. This complexity consumes extra amount of computational power and increase significantly the time for simulation. As the main interest of the simulation is the heat distribution in the detector, simulation of the gas distribution within the gas inlet chamber is not necessary. Therefore, the end-piece for the gas distribution system is replaced by a rectangular pipe. This reduces the number of element significantly and also the time for computation. Another modification is applied to the alignment of the sensor segment. Due to the presence of dead zone on the edge of the pixel sensor segment, the sensors are aligned with a 1mm overlap to the adjacent sensor, see figure 5.6. From experience, as this feature would be insignificant to the simulation but only increase the complexity of meshing in this region, it is eliminated. Consequently, all sensors are aligned along the edge of the Kapton® segment. With these modifications, the components are assembled to form a model for simulation. It is shown on figure 5.9.
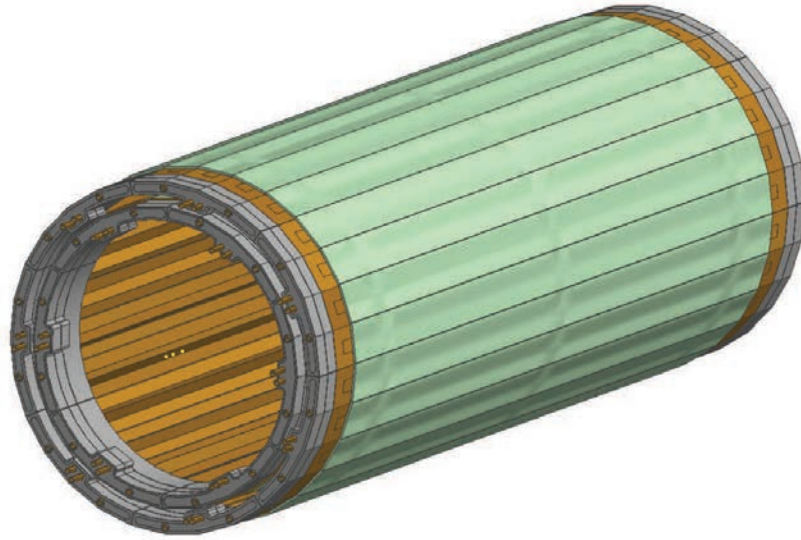
Figure 5.5: CAD model for the single station of the outer layer
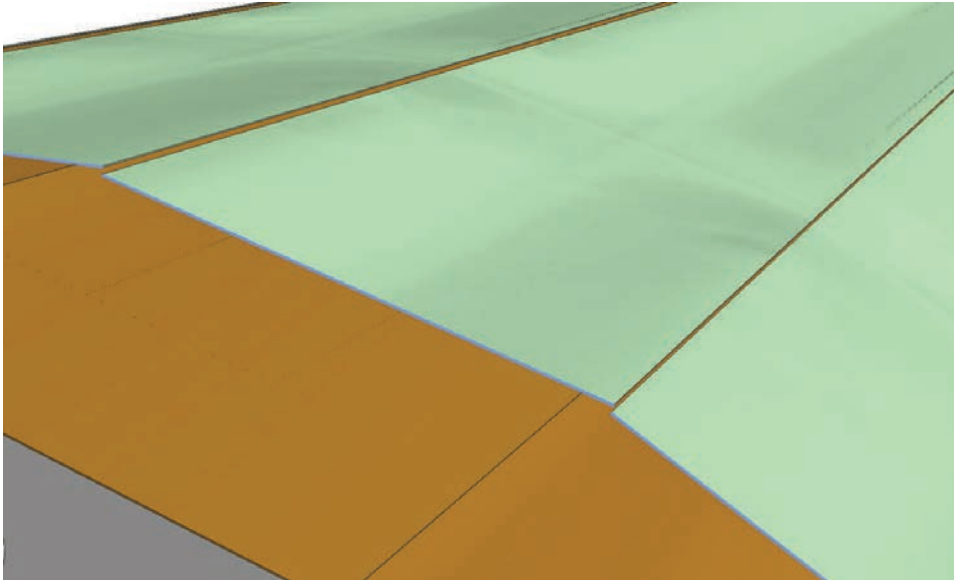
Figure 5.6: Offset alignment for the sensor segment
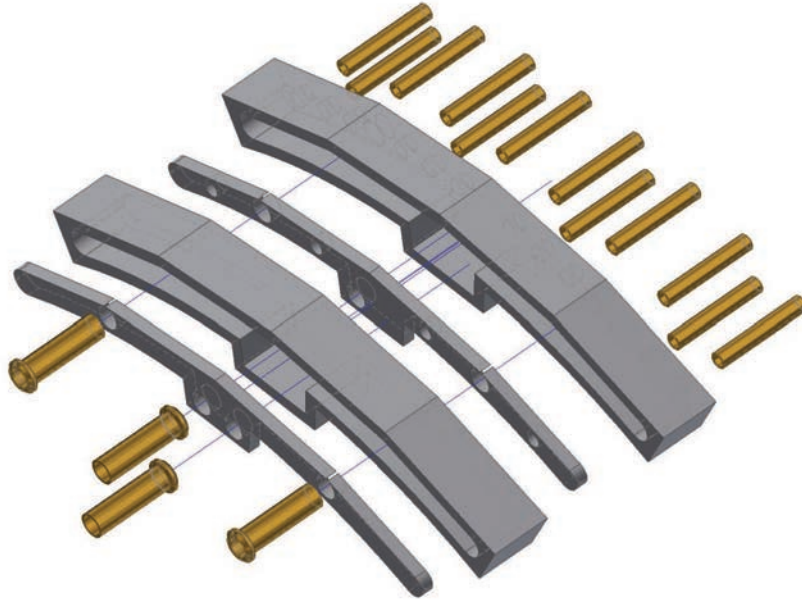
Figure 5.7: Schematics for assembly of the end-piece inlets

Figure 5.8: CAD model the Gas inlet for the simulation
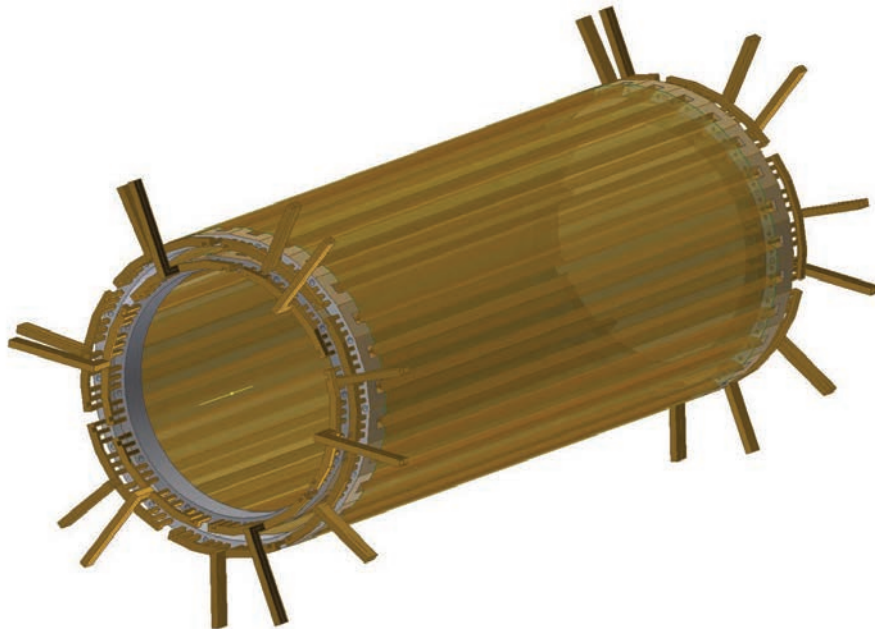
Figure 5.9: CAD model of the outer detector station for simulation

5.2 CFD Simulation

The CAD models are input into the software Autodesk® CFD simulation. Material properties are assigned to each of the components. Meshes are mapped onto the model and optimized for quality in a reasonable computational load. Boundary conditions for the simulation are set according to the situation in the experiment.

5.2.1 Meshing

The quality of meshing is a major factor to the quality of the CFD simulation. A poor mesh quality increases the chances for divergence and gives inaccurate solutions. It may even cause singularities. To avoid any numerical problem in the CFD process, a mesh with high quality is required in order to combine reasobale computational cost with sufficient robustmess for the solver to find a viable solution.

The mesh is first generated automatically by the program. Then, it can be modified the elements manually to optimize the mesh quality. Here, free mesh (nonuniform) with triangular planar structure is used for the element construction. The meshes of the detector model are shown in figure 5.10. One can see that the mesh is dense in the inlet region due to the small complex structure and the necessity of precise calculation for the gas distribution. In contrast, the mesh is less dense in the central body region as the flow is more uniform in the center region.

(a)   (b)
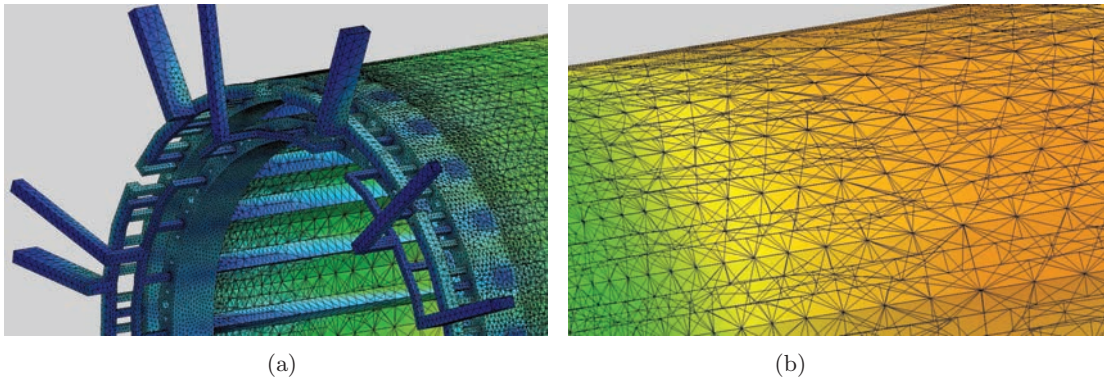
Figure 5.10: Mesh for the CAD model at the (a) gas distribution system and (b) center detector region

5.2.2 Boundary Condition

In order to demonstrate the heating and cooling effect of the system, boundary conditions have to be applied to the model. In order to compare the simulation result with cooling test performance, the boundary conditions are set according to the setting of cooling tests in section 3.2.

Helium Flow

Global helium flow is applied on one end of the station. To represent the flow, a velocity constraint is applied at the end of the helium cylinder into the station. Zero overpressure is applied at the other end to allow the free flow of helium. Velocities of the global helium flow v_{global} between 2.3 to 4 m/s is tested for the model.

The local helium flow with velocity v_{local} is applied from the opposite direction to the global helium flow direction. In order to compare to the test data, similar settings are applied in the simulation. As the local helium coolant for each of the module is supplied by one gas inlet, the velocity constraint v_{inlet} is calculated by the continuity equation for volume flow rate. Assuming incompressible flow, v_{inlet} is related to the local helium velocity v_{local}, area of the inlet A_{inlet} and the local flow channel A_{local} :

$$v_{inlet} \cdot A_{inlet} = \sum_{i=1}^{4} v_{local} \cdot A_{local} \tag{5.1}$$

For a local helium flow rate of 20m/s, the required inlet flow rate is $v_{inlet} = \frac{4 \times 20 \times 0.6^2 \cdot sin(60°)/2}{0.3 \cdot 0.3} \approx 141m/s$. Overpressure is applied at the open end of the opposite tube to allow free flow of helium.

Heating Power

The expected power consumption of the MuPix sensor is 250mW/cm^2. Although it is unlikely to reach this upper limit, the simulation covers the heating power up to 400mW/cm^2 in order to be on the safe side. For power consumption of 250mW/cm^2, the heating power on the sensor segment would be $P_{250} = 250 \times 1.9 \cdot 36 = 17.7W$ and $P_{400} = 400 \times 1.9 \cdot 36 = 27.32W$ for 400mW/cm^2 . The total heating power is evenly distributed on the whole sensor segment by setting the boundary condition over the whole volume.

Temperature Constraint

The Mu3e cooling system is designed to deliver coolant at temperature slightly above $0°C$. However, it is difficult to constantly supply helium at $0°C$ and maintain this temperature inside a container under normal laboratory condition. The alternative solution is to carry out the cooling test with helium coolant at $20°C \approx$ room temperature, as mentioned in section 3.2. So as to compare with the results, the temperature of the helium coolant is set at $20°C$ in the simulation.

Material Properties

To simulate heating effects, material properties such as specific heat capacity are crucial parameters. In the CFD analysis material types are assigned properly to each of the components. The sensor segments are assigned with silicon, and the gas distribution structure with ABS [1] plastic. Both of them are set to the default values provided by the software. As the material Kapton$^®$ does not exist in the data base of the software, it has to be imported manually. The material properties of Kapton$^®$ used for the Mu3e detector is listed on table 5.1 .

Thermal Property	Value
Thermal Coefficient of Linear Expansion	20 $ppm/°C$
Coefficient of Thermal Conductivity	0.12 $W/m \cdot K$
Specific Heat	1.09 $J/g \cdot K$
Density	1.43 g/cm^3

Table 5.1: The material properties of Kapton$^®$ of $25\mu m$ at 296K

---

[1] Acrylonitrile Butadiene Styrene, commen material for 3D printing

5.3 Verification of the Test Measurement

An imprtant question is if dead spots exist in the design whcih could be caused by turbulences. To predict the type of flow inside the model, the Reynolds number Re and the Mach number M of the two cooling channel in helium for $T = 20°C$, $\rho = 1atm$ is calculated by equation 5.2 [29] and 5.3. The values are listed in table 5.2

$$Re = \frac{vD}{\nu} \tag{5.2}$$

$$M = \frac{v}{a} \tag{5.3}$$

where v is the speed of flow, D is the diameter of the flow tube, ν is the kinematic viscosity, and a is the speed of sound in the medium.

Channel	Reynolds Number	Mach number
Local (20 m/s)	730	0.02
Global (4 m/s)	7500	0.004

Table 5.2: The Reynolds number and the Mach number of the two cooling channel

For Mach number < 0.3, incompressible flow can be assumed [28]. Turbulences are expected to occur at $Re \gtrsim 2300$ [29]. Therefore, the flow in local channel is predicated to be incompressible laminar flow, and incompressible turbulent flow in global channel. As only one type of flow model can be selected, the simulations are carried out with a turbulent and incompressible model. Iterative solver is used in Autodesk® CFD and results are monitored by convergence curve in the program to ensure convergence.

Simulation of Sensor Modules

To compare the simulation result with the cooling test, the model of the modules is simulated under a similar condition as the one in the cooling test. The model of modules of layer 3 and 4 for the simulation are shown in figure 5.11. Different form the situation of the Mu3e experiment, the cooling test made use of a heatbale Kapton® module to demonstrate the heating effect from the pixel sensors. Therefore, the heat source in the test is located on the kapton layer instead of the sensor layer. The simulations in this chapter follow the test setup. The boundary conditions for the simulation are set according to section 5.2.2 with the following parameter:

- $P/A = 400mW/cm^2$ at the kapton layer

- $v_{global} = 4m/s$ from the right

- $v_{local} \approx 20m/s$ for the left

- $T_{He} = 20°C$

- zero overpressure at all outlets

The relative temperature profile from the simulation is shown in figure 5.12. The temperature along the center line of the sensor segment is plotted against the distance from the left end of the segment. The simulation is compared with the test result. The results show a difference in maximum temperature of about $5°C$ between the simulation and test. Besides, the temperature

Figure 5.11: Modules of layer 3 and 4 for simulation

profile for layer 3 is higher than that for layer 4 in the simulation. This is different from the result in the cooling test, which is the other way around. Certain reasons can account for this difference.

First of all, it is a fact that the simulation is only an approximation to the reality. It is done with an isolated model within a helium chamber, which does not include all the influence from the reality, such as the heat conduction by the mechanical frame, heat conduction or radiation to the environment, uneven flux from the ventilation system, etc. They can potentially lower the temperature. Secondly, in the cooling test setup, the temperature sensor is localed on the glass plates, but not the heatable Kapton®. The indirect contact to the heat source and the exposure to the global flow may lower the measured temperature. Lastly, the flow velocity determined in the cooling test have uncertainties of 5%(local flow) to 20% (global flow). This is sufficient to significantly affect the temperature profile and potentially explains the mismatch of the curves.

The simulation with modules shows a peak temperature close to the cooling test, within the specification. To conclude, considering the complexity of the flow pattern in the module, the simulation gives a reasonable prediction for the cooling performance.
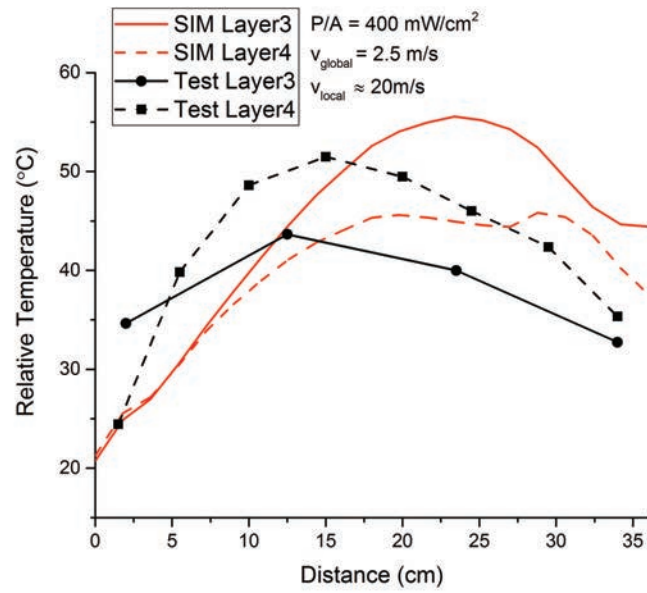
Figure 5.12: Temperature profile of module from the simulation with heating on Kapton® layer compared with cooling test, $P/A = 400mW/cm^2$, $v_{global} = 2.5m/s$, $v_{local} \approx 20m/s$, $T_{He} = 20°C$

Chapter 6

Simulation of the Mu3e Outer Pixel Station

In the cooling test setup, the heat source is located under the Kapton® foil, which is in direct contact to the local flow channel. This structure gives an advantage of efficient thermal conduction between the helium and the Kapton® layer. However, for the Mu3e detector, the heat source is the sensor, with a Kapton® foil separating it from direct contact to the local flow. Due to the poor thermal conductivity of Kapton®, the cooling ability of the local cooling channel may be less effective. To make this effect into account, heat flux is applied at the silicon in the simulation from now on. In this chapter, the simulations for one and three station are discussed. Another cooling channel for the gap area between layer 3 and 4 is introduced, named gap channel.

6.1 Single Detector Station

To see the influence on the cooling performance by putting several modules together, the model of the outer detector station (see figure 5.5) is used for simulation. The boundary conditions are set as follows :

- $P/A = 400mW/cm^2$ at the silicon layer

- $v_{global} = 2.3 - 4m/s$ from the right

- $v_{local} \approx 20m/s$ for the left

- $T_{He} = 20°C$

- zero overpressure at all outlets

To understand better the setup, a number of parameters is tested with the model. Table 6.1 shows the parameters of all simulations. Notice that, due to the integrated structure in the inlet end-piece, it is possible to provide an extra helium flow to the gap between layer 3 and 4. The flow in the gap region is now named gap flow with its velocity $v_{inlet(gap)}$. This gap channel is discussed in the following section.

The result for simulation 2 with heating power $P/A = 400mW/cm^2$, local flow $v_{local} \approx 20m/s$, global flow $v_{global} = 2.5m/s$ and helium coolant at $T = 20°C$ is shown in figure 6.1. The temperature profile is shown in figure 6.2 and the flow profile in figure 6.3 of the same simulation in cut view

Simulation	$P/A[mW/cm^2]$	$v_{global}[m/s]$	$v_{local}[m/s]$	$v_{inlet(gap)}$ [m/s]	v_{gap}[m/s]
1	250	2.3	20	0	1
2	400	2.5	20	0	1
3	400	2.5	20	125	2.5
4	400	4	20	0	1.5
5	400	4	20	200	4

Table 6.1: Parameter for the cooling simulation of a outer detector station

along the beam axis. Absolute temperature is given. A maximum temperature of $74.5°C$ is found at the middle of the gap between the two layers in the helium. The flow diagram indicates that the helium flow velocity is very low in the gap between the layers. The temperature profile of the sensor layer in the one station simulation is then compared with the module simulation in figure 6.4. It shows the relative temperature of the sensor layer plotted against the distance from the left end-ring. A maximum temperature of $\Delta T = 64°C$ is found on the sensor layer 3, $2°C$ higher than the simulation of the module. The right end of the layer 4 is also found to be higher by about $4°C$. The simulations with different parameter are then compared. Figure 6.5 shows the temperature profile of the detector in simulation 1 and 2 with heating power of $250mW/cm^2$ and $400mW/cm^2$ under the same global and local flow rate. An overall increase of $10°C$ to $25°C$ is observed on both layer 3 and 4 when the heating power is raised.

Figure 6.6 compares the temperature profile of the detector in simulation 2 and 4 with different global velocities. The increase in global velocity from 2.5m/s to 4m/s gives a significant decrease in temperature.
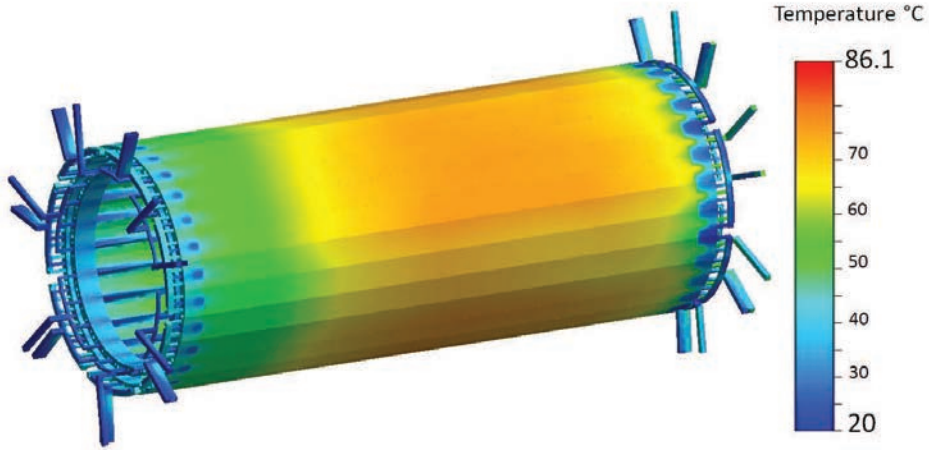
Figure 6.1: Absolute temperature for a single station for P/A $=400$mW/cm^2, v_{global} $=2.5$m/s, $v_{local} \approx 20$m/s, $T_{He} = 20°C$
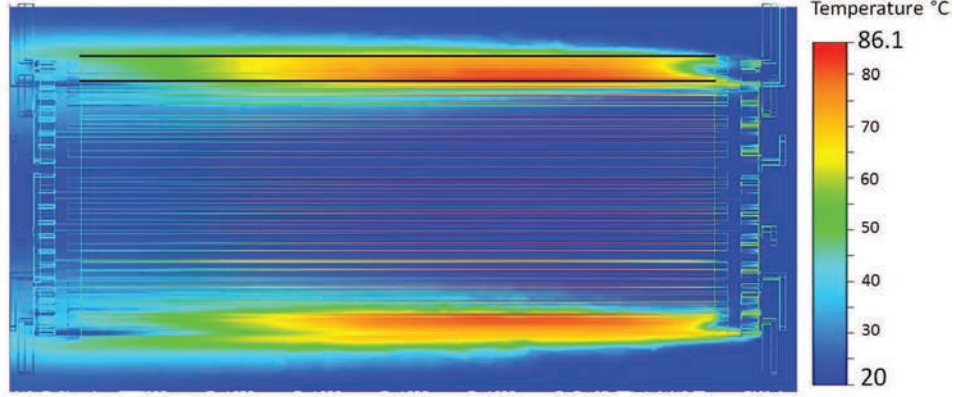
Figure 6.2: Temperature profile for the simulation of a single station, P/A =400mW/cm^2, v_{global} = 2.5m/s, $v_{local} \approx$ 20m/s, $T_{He} = 20°C$
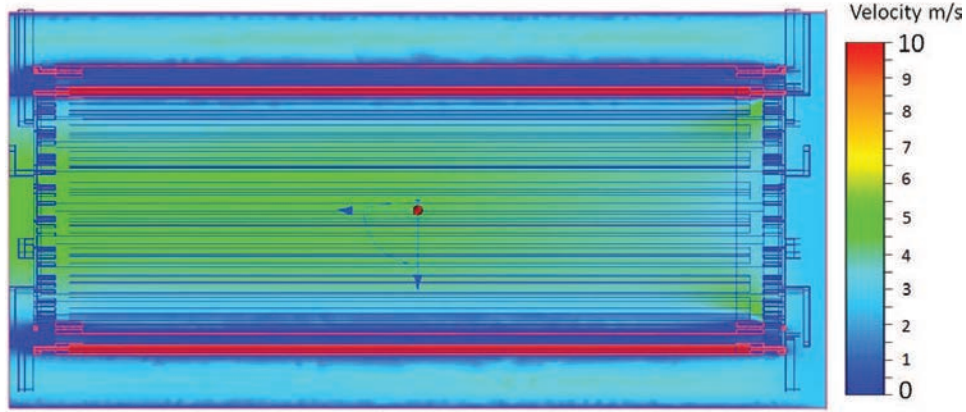
Figure 6.3: Flow profile of the the simulation 4 ,P/A =400mW/cm^2, v_{global} =2.5m/s, $v_{local} \approx$ 20m/s, $T_{He} = 20°C$

6.2   Single station with Gap Flow Inlet of Endring

As mentioned in the previous discussion and shown in figure 6.3, the helium flow within the gap between layer 3 and 4 is weak, compared to the center region. The narrow gap can be accounted for this situation. The idea to improve the cooling between layer 3 and 4 is to make use of the integrated inlet structure, which is able to provide extra helium flow to the area. From here on this cooling channel for the gap flow is introduced and named gap flow channel. In the following simulation, helium flow is applied from the gas distribution inlet to the gap from the right hand side. The target is to increase the gap flow velocity v_{gap} to the value of the boundary condition of the global flow v_{global}. The required inlet velocity for the gap flow $v_{inlet(gap)}$ is related to the simulated velocity in the gap $v_{gap(sim)}$ and the area of the gap A_{gap} by

$$v_{inlet(gap)} = \frac{(v_{global} - v_{gap(sim)}) \cdot A_{gap}}{number\ of\ inlet \times area\ of\ the\ inlet} \quad (6.1)$$

43
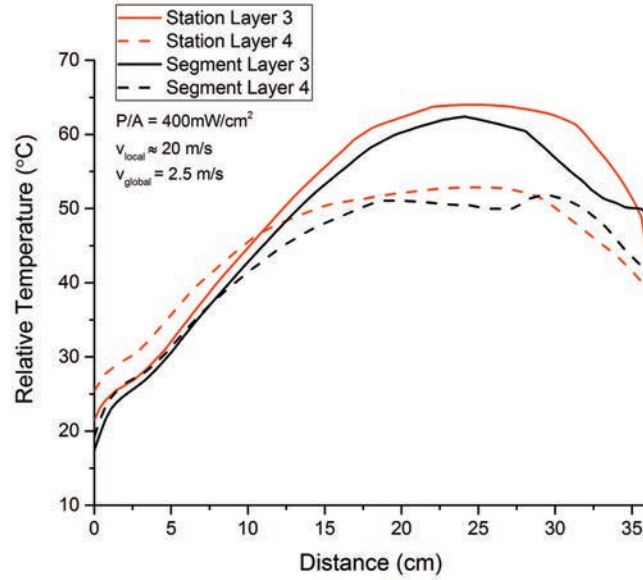
Figure 6.4: Temperature profile of single detector station with module, $P/A = 400mW/cm^2$, $v_{global} = 2.5m/s$, $v_{local} \approx 20m/s$, $T_{He} = 20°C$
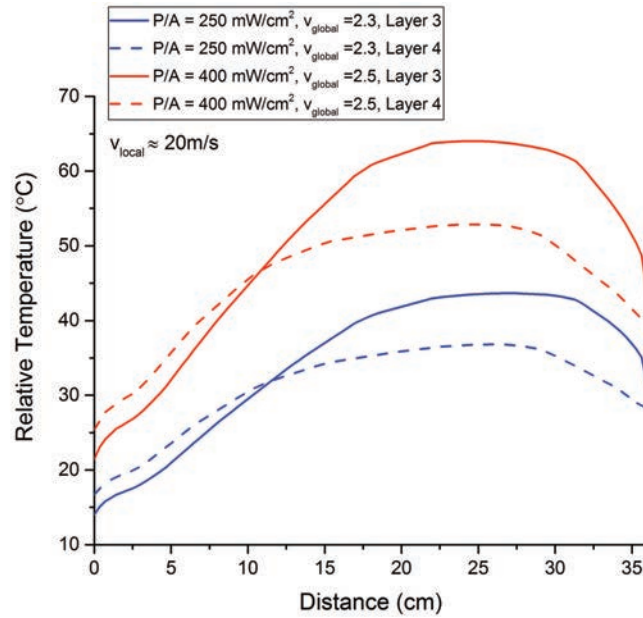
Figure 6.5: Temperature profile of single detector station with different heating rate, $v_{global} = 2.5m/s$, $v_{local} \approx 20m/s$, $T_{He} = 20°C$
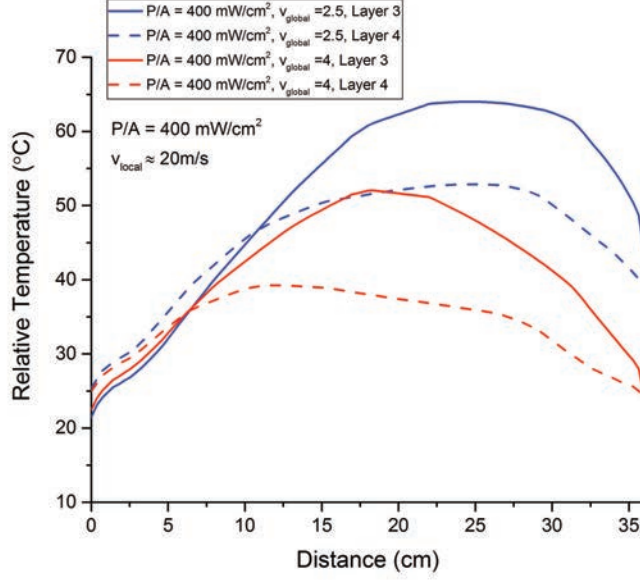
Figure 6.6: Temperature profile of single detector station with different global flow rate, $P/A = 400mW/cm^2$, $v_{local} \approx 20m/s$, $T_{He} = 20°C$

The approximate velocity at the global inlet for $v_{gap} = 2.5m/s$ and $4m/s$ are $v_{inlet(gap)} = 125m/s$ and $200m/s$. This boundary condition is added to the previous simulation. The result of the simulation with global inlet is plotted in figure 6.8 with relative temperature against distance from the left end-ring. It can be seen that the additional flow successfully decrease the maximum temperature by about $20°C$ in both case.

6.3 Three Detector Station

By adding two more detector stations to the single detector, the outer detector system for phase Ib is illustrated. This simulation provides a preliminary view for the cooling ability for the outer detector of phase I. The figure 6.9 shows the absolute temperature of the simulation for three stations with piping. A power consumption of $400mW/cm^2$ is applied on the silicon sensor. Global flow of 4m/s is applied from the right hand side and local flow of 20m/s is applied into the local channel from the left hand side. A flow is applied to the channel channel to maintain the gap flow velocity at 4 m/s. Helium of 20°C is used as coolant. A maximum temperature of 73.35°C is found in the gap between 2 layers of the left region of the first station. The relative temperature of the sensors is plotted against the distance from the left station and can be found in figure 6.10. The temperature (ΔT) profile of the right most station appears similar to the single station in previous section with similar boundary condition (see figure 6.8). There is a steady increase of temperature across the station in about $5°C$, due to the heating up of global helium along the detectors. So far no dead spot is found inside the outer detectors.
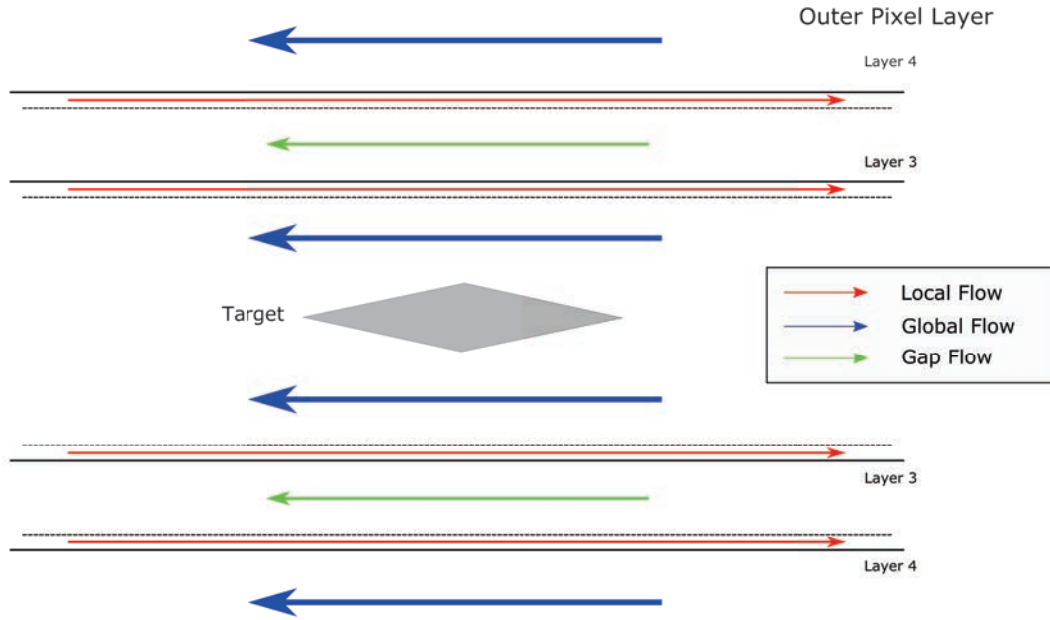
Figure 6.7: Flow pattern of the outer pixel detector
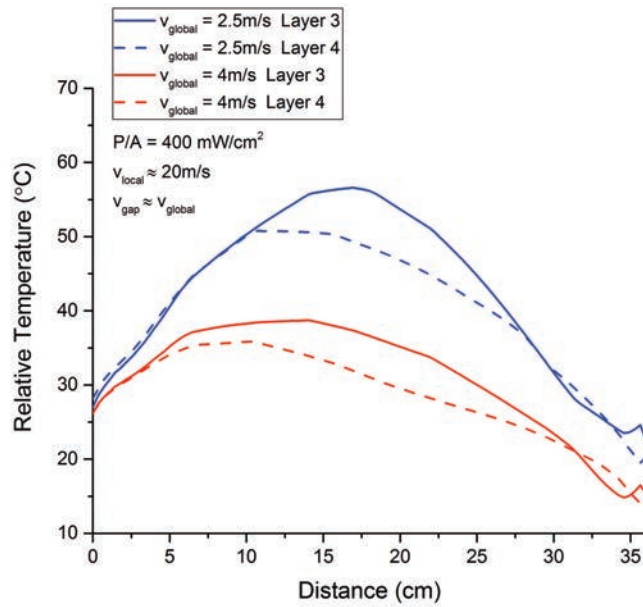
Figure 6.8: Temperature profile of detector station with helium supply from gap inlet at end-ring, $P/A = 400mW/cm^2$, $v_{local} \approx 20m/s$, $T_{He} = 20°C$
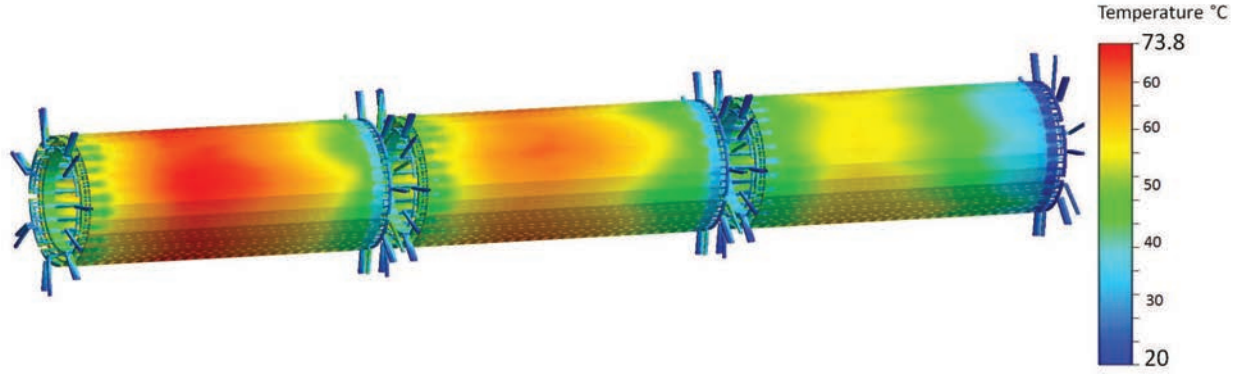
Figure 6.9: Simulation for three station, temperatures are actual temperatures, P/A =400mW/cm^2, $v_{global} = 4$m/s, $v_{local} \approx 20$m/s, $T_{He} = 20°C$
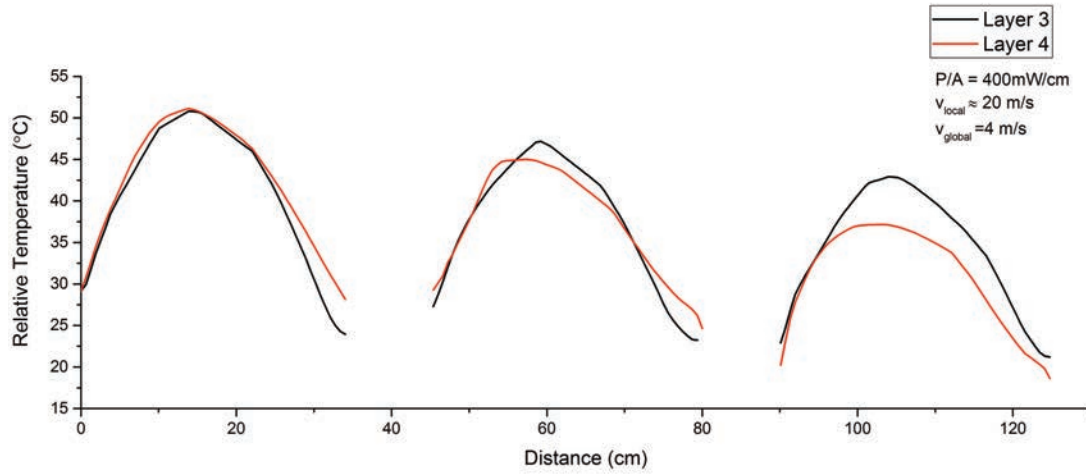
Figure 6.10: Temperature profile for three detector station, P/A =400mW/cm^2, $v_{global} = 4$m/s, $v_{local} \approx 20$m/s, $v_{gap} = 4$m/s, $T_{He} = 20°C$

Chapter 7

Optimization of the Gas Distribution System

The full phase II Mu3e detector is divided into 5 stations. The inlets of the cooling system are located at the ends of each detector station. As the end-rings are not covered with sensors, there is a inactive region between detector stations. In addition to the separation for mechanical assembly between each station, there would be a dead zone with a width of approximately 10cm (for the design in section 6.) Moreover, for the reason of easy assembly and disassembly, the detector station is divided into several sensor modules. Each of the modules carries its inlet and outlet. Altogether there would be a total of 52 gas pipes for each station and there are no enough space for all of them. Therefore, a modification for the end-ring design is necessary.

In this chapter, the compact design for the end-ring with integrated gaseous distribution is introduced. A model will has been built and simulated under the Autodesk® CFD for the optimization of the flow pattern.

7.1 Modeling

Compact End-Piece and End-Ring

In order to minimize the separation between detector stations and to reduce the number of gas pipes, the idea is to integrate the inlet end-piece into a gas distribution end-ring and reduce the tickness of all the components in the end-structure. Instead of using one inlet end-piece to supply helium gas into one module, the compact design makes usage of a end-ring to supply helium flow into the entire detector station. All of the inlet end-piece is integrated into one hollow end-piece with only one chamber for gas distribution and helium gas is supplied by few inlet pipes. This geometry greatly reduces the number of inlet pipes. The end-ring is specialized for either local or gap flow distribution by alternating arrangement of outlet holes. The design is shown on figure 7.1. The geometry of the supporting end-piece remains as the the previous design but with a relocated inlet hole. The end-pieces on the 2 ends of the module are no longer identical. They are distinguished by the function for either local flow or gap flow. Hence the flow pattern is redesigned. The design is shown on figure 7.2. The local helium flow enter the V-shaped fold from the local flow end-ring. Instead of guiding out the heated gas on the other end, the gas is release into the gap flow channel at the gap flow end-piece. As in the earlier design, gap end-pieces provide extra helium to the channel between the layer 3 and 4 to increase the cooling. The flow pattern for the compact design is shown in figure 7.3. The thickness of the gas distribution end-ring is reduced to

11mm and for supporting end-piece to 9mm. The dead zone of the detectors station is reduced by 20mm.

Figure 7.1: The CAD model (with 3 gaseous inlet) for an compact end-ring
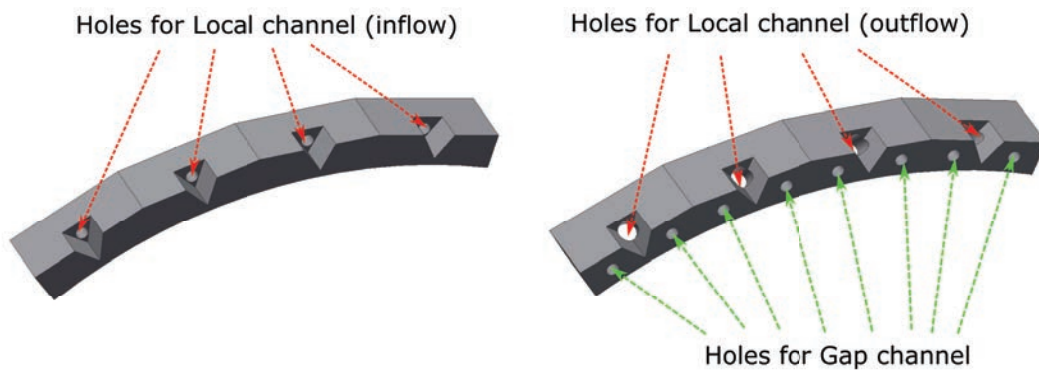
Figure 7.2: The CAD model of a compact end-piece for local channel (left) and a compact end-piece for gap channel (right)

Assembly

The modified component are assembled to form a detector station. The CAD model with 3 gas inlets can be found in figure 7.4. All components have been redrawn with corrected geometry. Same as the model in section 5.1, the offset detail of the sensor segment is omitted in this drawing. As we want to study the flow pattern inside the end-ring, no further simplification is applied on it.
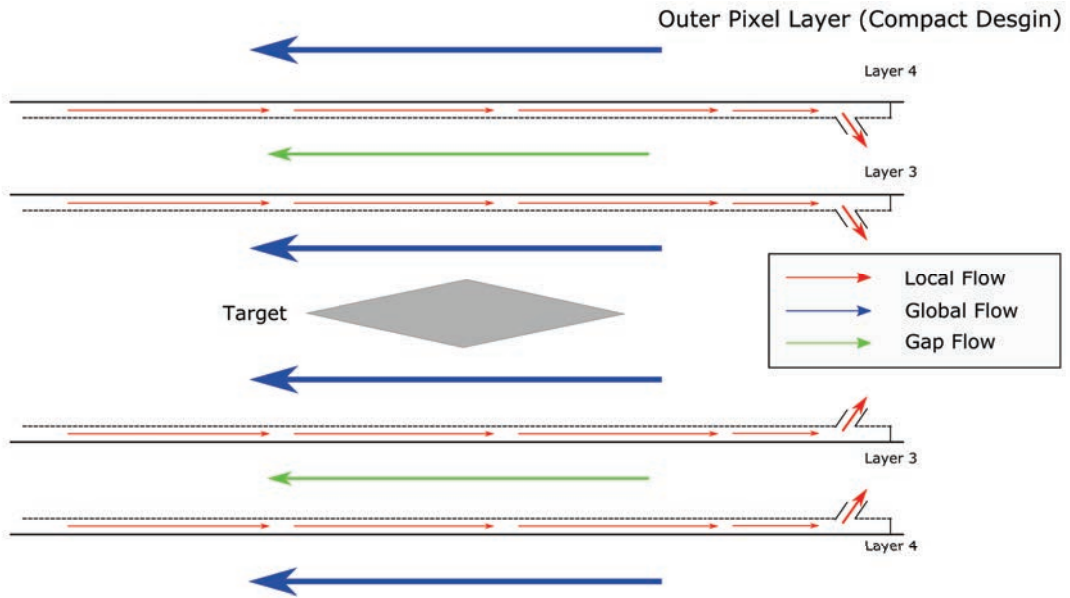
Figure 7.3: Flow pattern for the compact gas distribution design
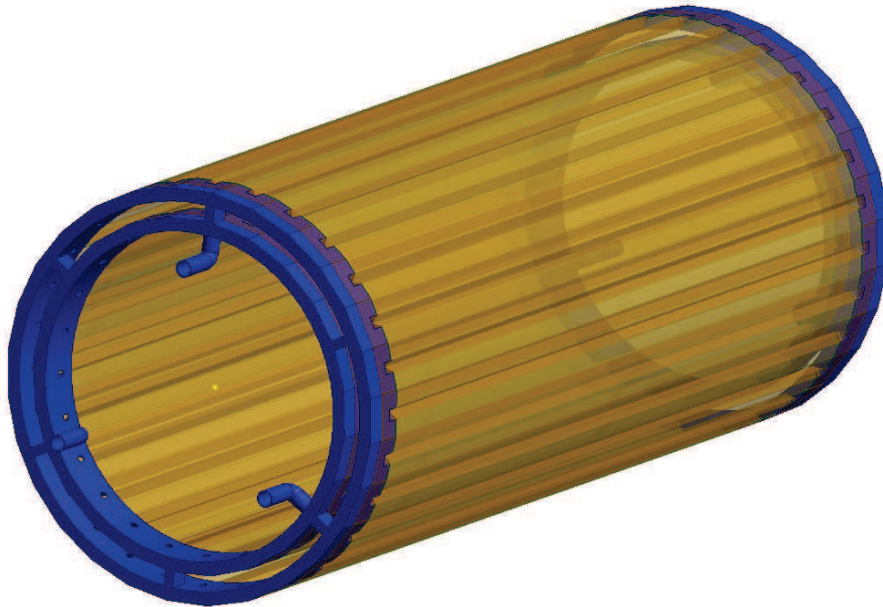
Figure 7.4: CAD model for the single station of the outer layer with integrated end-ring

7.2 Simulation

Gas distribution Optimization

Due to the decrease of number of inlets and the all- in-one design of the end-ring, nonuniform flow patterns may be found at the outlets. In order to study the performance of the compact gas distribution system, the end-ring is simulated under Autodesk® CFD with a set of different parameters. The end-ring is equipped with a number of inlet pipe with a inner diameter of 6mm. The end-ring is contained in a cylinder of helium. The following boundary condition is applied to the model :

- constant velocity is applied in all inlets

- zero overpressure is applied to both of the open end for the free flow of helium.

The schematics of the setting is shown on figure 7.5. The flow direction is indicated as arrow (c) and the pressure constraints are highlighted in red at the back (b).
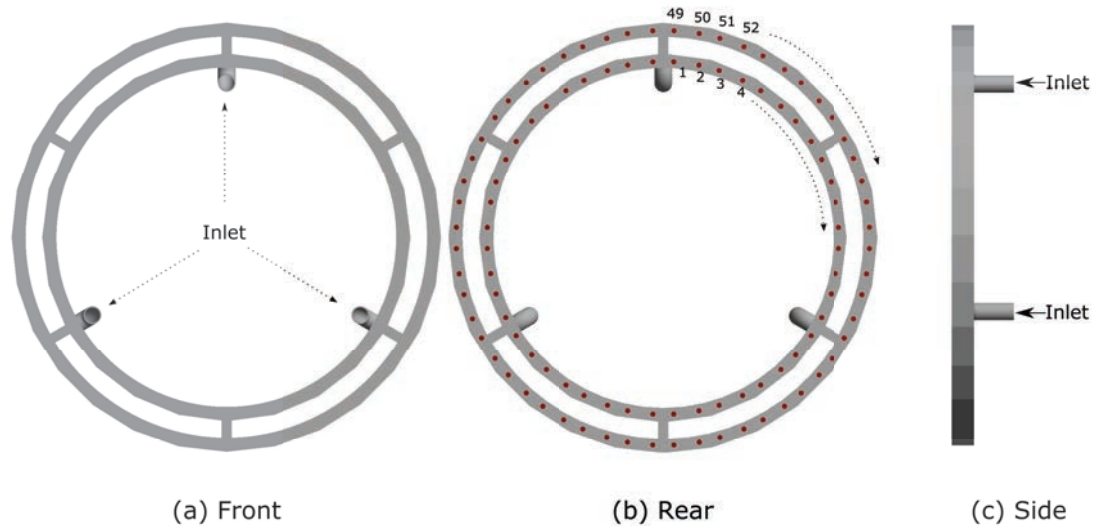
Figure 7.5: schematics for the boundary condition of the simulation with compact end-ring

As the geometry of the end-ring for local cooling and for gapl cooling are almost identical and only differ in outlet number, the outlet patterns of the two end-rings are expected to be similar. It is sufficient for the study of flow patterns to simulate only one of the models. Here, the end-ring of the gap channel cooling is chosen. The target of the design is to establish a uniform gas distribution in the flow channel with a minimal number of inlets. In the simulation, models with 2, 3 and 6 inlets are investigated. The models are simulated under the same condition, such that the total volume flow rate is the same for all model.

The flow velocity at the outlet holes of the setups are plotted in figure 7.6. The outlet number represents the position of the outlet holes. Outlet numbers 1-48 present the outlet holes on layer 3 and 49-104 for the layer 4, as shown in figure 7.5(b). For the model with 2 and 6 inlets, a large drop is found across the outlet of different layer (at outlet number around 50), which indicates a different flow rate at the outlet for the two layers. Only the model with 3 inlets gives an insignificant

drop in outlet velocity across the layers. The enormous fluctuation of velocity in the 2 inlet model shows an extreme uneven flow rate among outlets, even in the same layer. When the flow leaves the local channel, it will disturb the flow in global channel. An uneven flow increases the chance of turbulent flow. Therefore this 2 inlets model is not suggested. The plots for models with 3 and 6 inlets show a relatively small fluctuation. Considering the number of inlet and the flow pattern across layer, it is suggested to use the model with 3 inlets, under this geometry constrain.
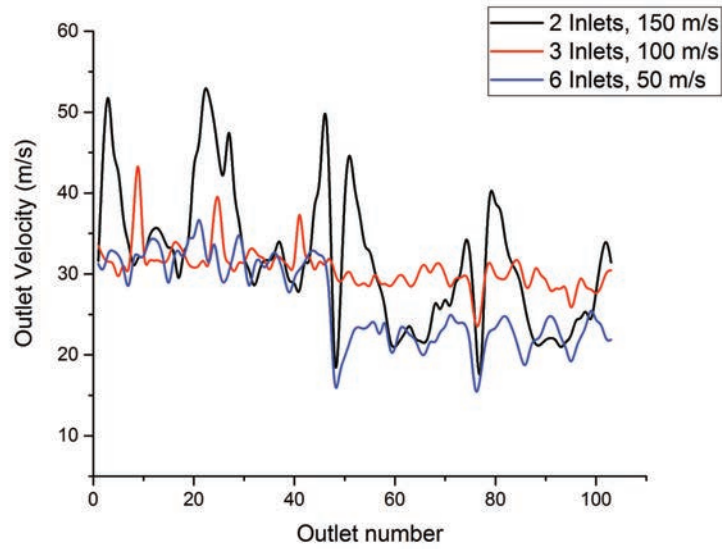
Figure 7.6: Flow rate at outlet with different number of inlets; the outlet number 1-48 represents the outlet of layer 3 and 49-104 for layer 4

To understand how the design behaves for various conditions, the model with 3 inlets is then tested with different inlet velocities v_{inlet}. The result is plotted in figure 7.7. Although the end-ring with 3 inlets gives a comparatively homogeneous output at inlet velocity of 100m/s, the uniformity starts to break down once at 150 m/s. The output flow becomes completely uneven at 200m/s. Therefore, it is suggested that the inlet velocity should not excess 150m/s. In figure 7.8, the flow pattern inside the end-ring is shown with flow direction indicated as arrow.

Single Outer Detector Station

In the above section, it has been concluded that the end-ring with 3 gas inlets is sufficient to provide a uniform gas distribution under for designed geometry. Further studies use this gas distribution design. The detector model shown in figure 7.4 is contained in a helium tunnel. The boundary condition are set as follows :
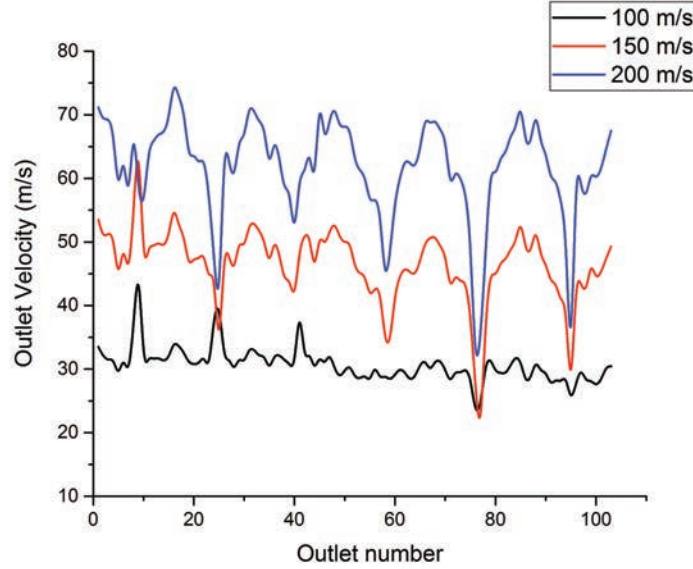
Figure 7.7: Flow rate at outlet with different flow rate at inlet with 3 inlets

- no slip on all walls of the flow tunnel, i.e. $\vec{v} = 0$ at the surface of the helium cylinder

- uniform heat flux along the silicon segment, corresponding to $250mW/cm^2$, $400mW/cm^2$ and $500mW/cm^2$

- constant velocity at all end-ring inlet, $v_{inlet} = 100$ - 150 m/s

- constant velocity at the right end of the flow tunnel, $v_{global} = 4m/s$

- constant temperature for all helium inputs, $T_{He} = 0°C$

- zero overpressure at the left end of the flow tunnel at helium outlet

As we no longer compare the simulation with the data, the temperature of the coolant is set to $0\,°C$. Therefore, the relative temperature ΔT in the following simulation is the same as the actual temperature on the detector T in $°C$. Notice that due to the high speed of sound in helium, the Mach number for a 100m/s flow is about 0.1 only. Therefore the assumption on incompressible flow still holds. In figure 7.9, the temperature profile of the single detector station with the compact gas distribution system is plotted against the distance from the left end. Simulations with various setting of the heating power are shown in the diagram. Besides the gradual increase of the temperature profile with the heating power, the temperature difference between the two layers increases significantly.

To study the performance of the compact gas distribution system, the model is tested with different gas velocities at the inlet. The plot for the temperature profile is shown in figure 7.10. To see the effect on the local and gap cooling clearly, the velocity at the two end-rings are varied separately. In the graph, the inlet velocity at the local end-ring is indicated as v_L and at the gap

(a)   (b)
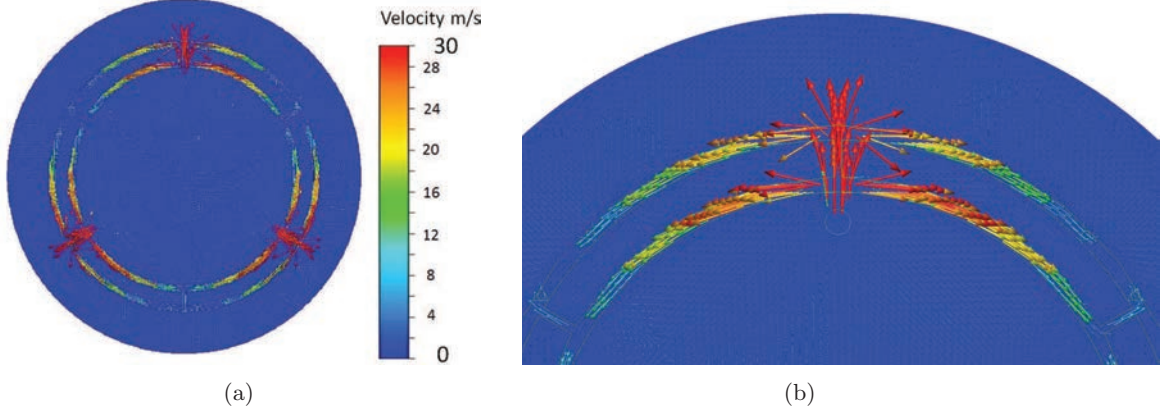
Figure 7.8: Flow pattern inside the end-ring with $v_{inlet} = 100m/s$

$v_G or v_L$ [m/s]	v_{local} [m/s]	v_{gap} [m/s]
100	3.5	16
150	4	27

Table 7.1: Relation between inlet velocity and flow velocity in local and gap channel

end-ring as v_G. Table 7.1 shows the relations between velocity at the inlet and that inside the channel.

By increasing the inlet velocity of gap flow v_G from $100m/s$ (black curve) to $150m/s$ (red curve), the temperature of both layers decreases significantly. As the gap flow inlet provides fresh helium to the gap between the layer 3 and 4, the increase of the flow improves the cooling in the gap which eventually reduces the temperature difference between the two layers.

The effect of increased inlet velocity for the local flow is interesting. After increasing v_L from 100ms (red curve) to 150ms (blue curve), the maximum temperature on layer 3 decreases but the temperature at the right end region increases. As the gas outlet for local cooling is removed from the compact design, the warmed gas from the local channel is released into the global channel after passing through the fold in the supporting structure. The outcoming gas from the local channel blocks the gas of the global channel from flowing into the gap between layer 3 and 4, resulting in a decrease of the flow between the layers. The flow is indicated with arrows in figure 7.11. The released gas also heats up the fresh incoming helium near the region. Although the hot helium will be cooled down after further mixing, it is enough to slightly increase the temperature around the region. This effect becomes more significant once the flow rate of the local channel increases, which explain the temperature profile of the blue curve. In figure 7.12, the flow pattern at the end-ring with adjacent station from simulation in section 9.3 is shown. It shows that turbulences form near the outlet of the local flow. Also, the outcoming local flow increase the speed of the global flow.

Another concern is the overpressure inside the end-ring. It is important to make sure that the end-ring structure can hold the pressure of the flow. It is investigated by extracting the pressure data from the simulation. In figure 7.13a and 7.14a, the pressure profile in side the end-ring with the inlet velocity $100m/s$ and $150m/s$ is shown. Due to the use of low density helium, the pressure is only in the order of 10 $mbar$ even with an inlet velocity of 100m/s.
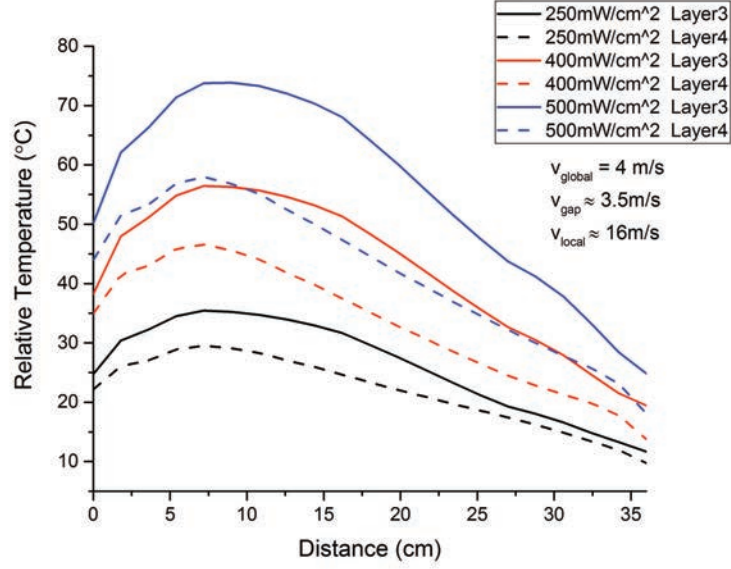
Figure 7.9: Temperature profiles with different power consumption; $v_{global} = 4m/s$, $v_{local} \approx 16m/s$, $v_{gap} \approx 3.5m/s$, $T_{He} = 0°C$
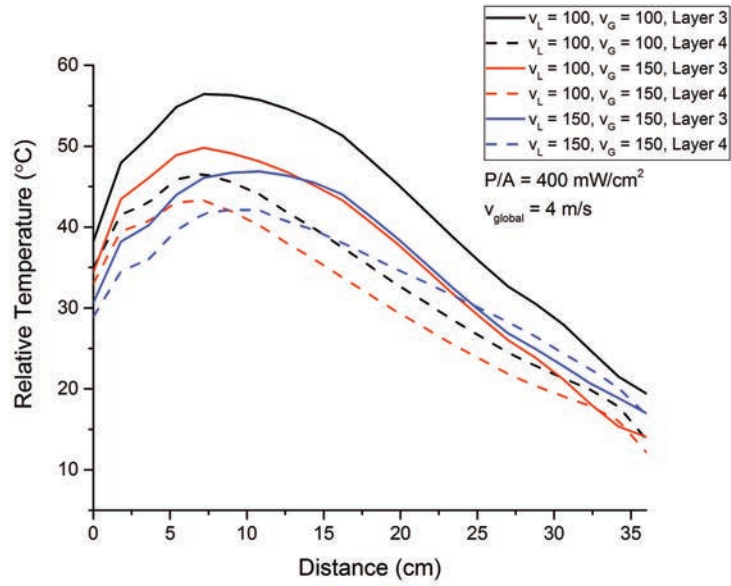
Figure 7.10: Temperature profiles with different inlet flow rate; $P/A = 400mW/cm^2$, $v_{global} = 4m/s$, $T_{He} = 0°C$
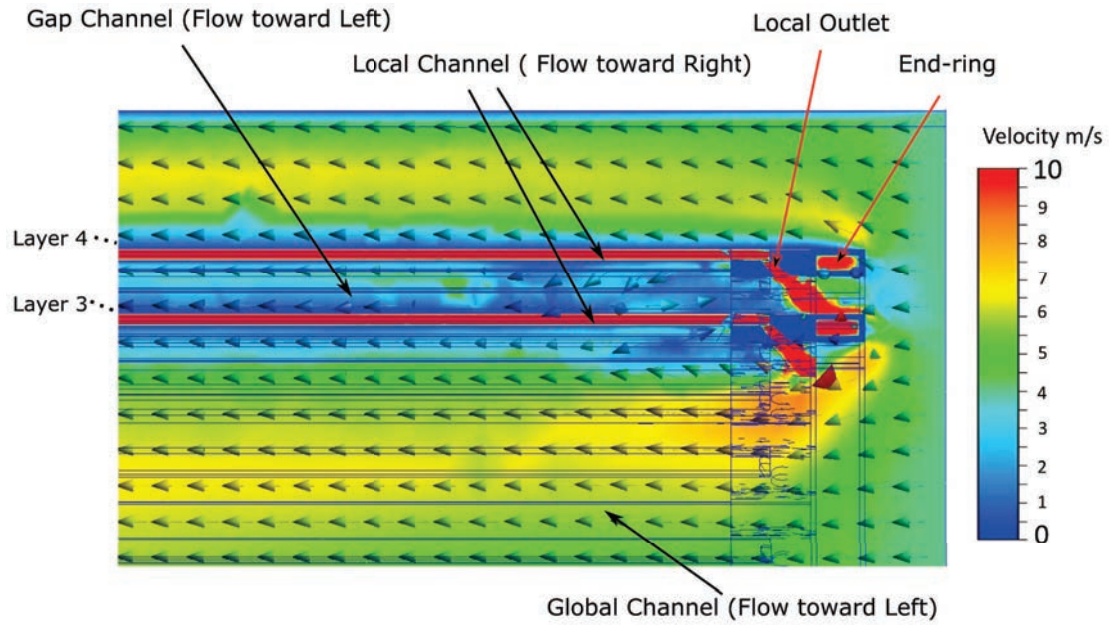
Figure 7.11: Flow pattern at the global end-ring, $v_{local} \approx 16m/s$, $v_{gap} \approx 3.5m/s$, $v_{global} = 4m/s$. The outcoming gas from the local channel blocks the gas of the global channel from flowing into the gap between layer 3 and 4. Black lines are the projection of the detector.
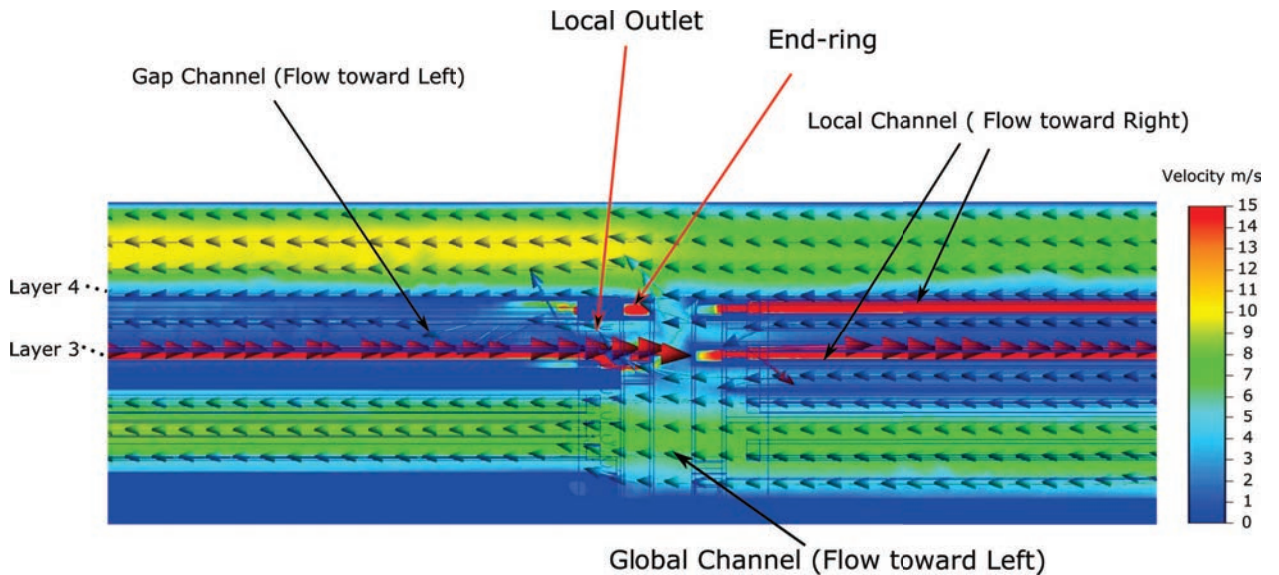
Figure 7.12: Flow pattern at the global end-ring, with adjacent station, $v_{local} \approx 16m/s$, $v_{gap} \approx 3.5m/s$, $v_{global} = 4m/s$

(a) $v_{inlet} = 100m/s$ ($v_{gap} \approx 3.5$)

(b) $v_{inlet} = 150m/s$ ($v_{gap} \approx 4$)
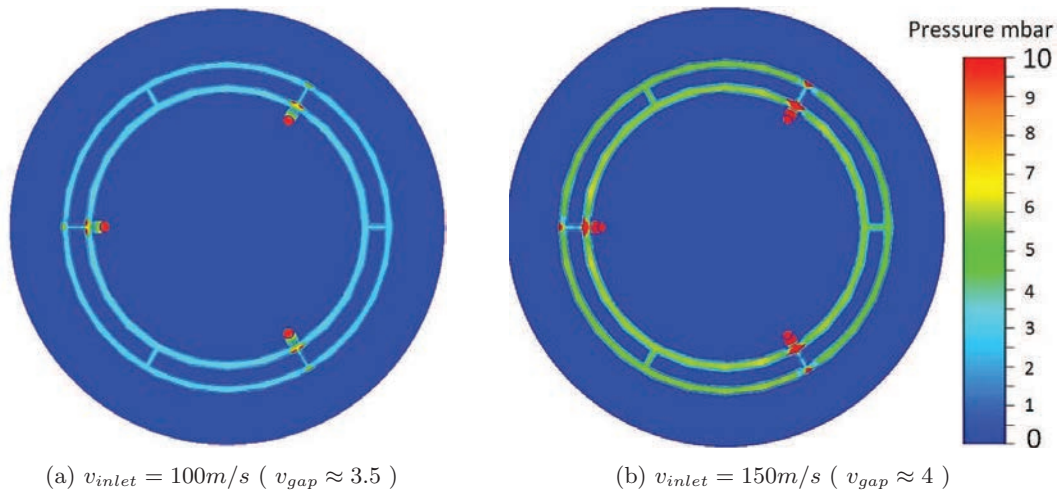
Figure 7.13: Pressure profile in end-ring for gap flow

(a) $v_{inlet} = 100m/s$ ($v_{local} \approx 16$)

(b) $v_{inlet} = 150m/s$ ($v_{local} \approx 27$)
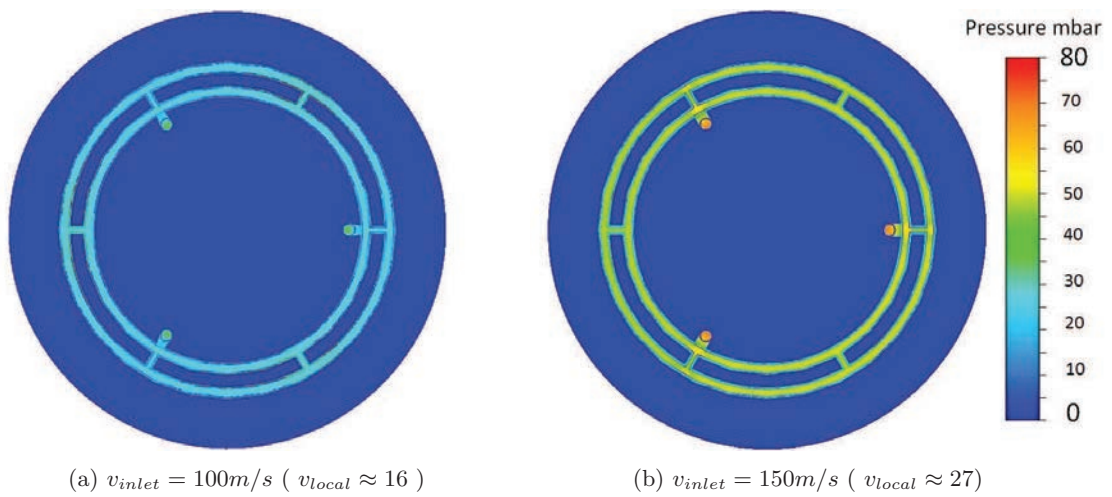
Figure 7.14: Pressure profile in end-ring for local flow

Thickness Reduction of End-Ring

In the discussion in this section, the thickness of the end-ring and end-pieces are reduced to 11mm and 9mm respectively, but the limit to the thickness is not known. Therefore, simulation with thinner end-structure is carried out. The thickness of the end-ring is further reduced to 6mm and 4 mm for the end-piece. The total thickness of the end-structure is then 10mm and gives a reduction of 20mm in separation between the sensors of adjacent station. Thickness reduction of the end-ring means reduction in volume of the gas distribution chamber, leading to possibly nonuniform gas distribution and an increase in pressure. To test how it would affect the flow, the model is tested in CFD simulation. The result shows that the pressure in the gas distribution chamber doubles its value (figure 7.15a) and a balanced flow into the local flow channel (figure 7.15b) can be maintained.

(a) Pressure profile   (b) Flow profile
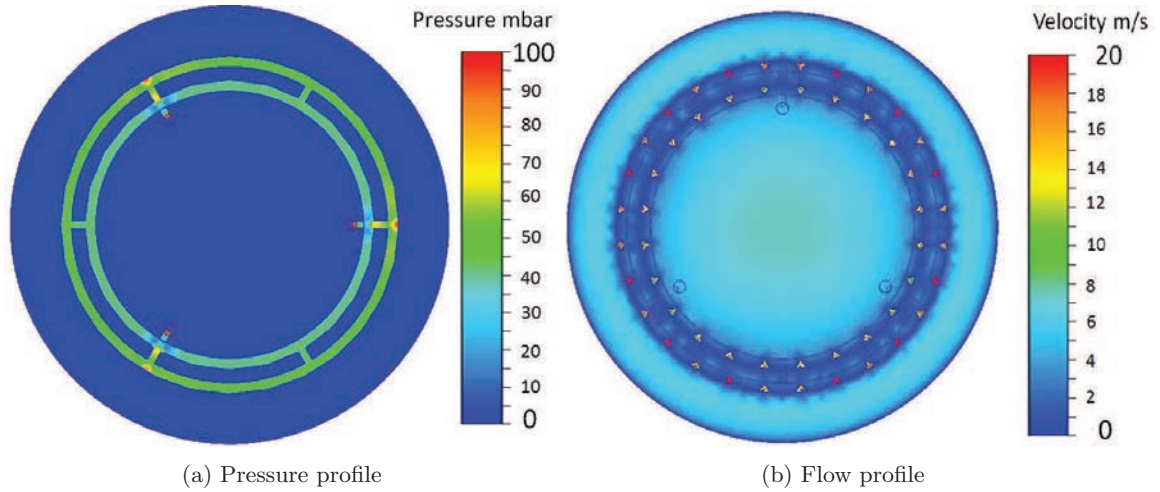
Figure 7.15: Pressure and flow profile of 4mm end-ring

Chapter 8

Simulation of Inner Detector Components

The results of the simulation from section 6 are satisfying. However, the model only represents part of the detector with the inner detector components not included in the simulation. In this section, the simulation goes beyond the tests in the laboratory and include most of the inner components of the Mu3e detector. The model of the inner components is shown and the CFD simulation is applied to this model.

8.1 Inner Sensor Station with Target

Inner Detector

The components for the inner detector are drawn in Audtodesk inventor and put together. The CAD model for the inner detector is shown in figure 8.1. Sensor segments of size 12 cm x19 mm are attached and aligned on a Kapton® segment of 14 cm x19 mm. The layer 1 and 2 consists of 8 and 10 of these Kapton®-sensor segments. The sensor segments are mounted on end-ring with 1cm thickness. The components are assigned with proper material types as the outer detector.

Stopping Target

The stopping target of the Mu3e experiment is double cone shaped. It is made of mylar for suppression of multiple coulomb scattering. It is hollow double cone with a thickness of 30μm in the front part and 80μm aluminum in the back part. The total length of the target is 100mm and the diameter for the base is 20mm. For the CFD simulation, this model is included as an obstacle for the possible helium flow in the central region of the inner detector, which means the hollow feature is not necessary for the simulation. Therefore, the CAD model of the stopping target is drawn in a solid cone shaped.

Simulation

By adding the inner detector to the outer detector station, the Mu3e pixel detector model for phase Ia is complete (figure 8.3). The simulation of this model only includes the pixel detector and target but not beam pipe and water cooling system. Therefore, this simulation represents an unrealistic situation of the experiment but a valuable reference for the study.

Figure 8.1: CAD model of inner detector

Figure 8.2: CAD model of target

The model is simulated under the following boundary condition:

- $\vec{v} = 0$ at the wall of the helium tunnel

- total heat flux on the silicon segment corresponds to $P/A = 250mW/cm^2$ and $400mW/cm^2$

- $v_{inlet} = 100m/s$ for each inlet ($v_{local} \approx 16m/s$ and $v_{gap} \approx 3.5m/s$)

- $v_{global} = 4m/s$ at the right end of the flow tunnel

- $T = 0°C$ for all inflowing helium

- zero overpressure at the left end of the flow tunnel

The result for the simulation with heating power of $250mW/cm^2$ is plotted in figure 8.4. The temperature profile of each layer is plotted in one diagram, against the distance form the left end of the outer detector. The temperature profile for a heating power of $400mW/cm^2$ can be found in figure 8.5. The presence of the inner detector, acting as extra heat source, gives a raise in peak
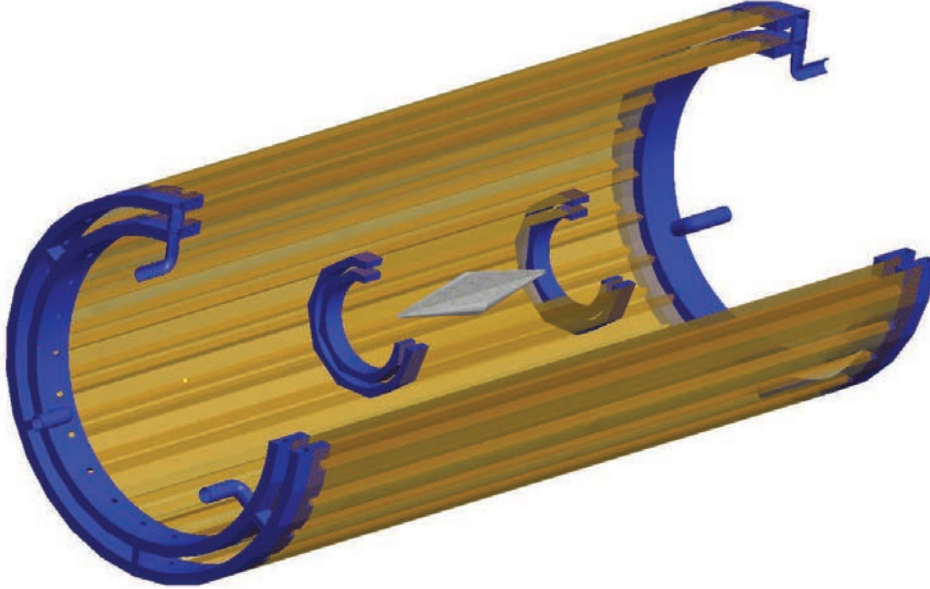
Figure 8.3: CAD model of the phase Ia pixel direction and target for simulation

temperature of around 5 $^{\circ}C$. As the inner detector is located in the center of the outer detector station, where fresh helium flows in without obstacle, the inner detector is well cooled down in both simulations. Note in phase 1b a SciFi detector will be added between inner and outer pixel layers.

8.2 Beam Line

Besides the inner detector, there is the beam line with FPGA boards, scintillating fibers and scintillating tiles inside the Mu3e detector. It is crucial to add these to the simulation in order to know how the cooling system behaves exactly. In the following section, the modeling and analysis of the beam line is discussed. The beam pipe consist of three parts of different shape. Nearest to the inner detector station, there is a hexagonal pipe with a width of 36 mm. At the other end there is the heptagonal pipe with integrated water cooling. The heptagonal port has a width of 28 mm on each side. Lastly there is a short octagonal pipe in the middle, with a width of 26 mm.

Beam Line as an Obstacle

In figure 8.6 a 3D printed model for the beam pipe is shown. The beam pipes are placed in the central region along the axial direction in front and behind the inner detector. It is expected that the global helium flow to the inner detector will be blocked by the beam pipe and hence affect the cooling efficiency on the inner detector. In order to study the effect, a CFD simulation with the beam pipes is performed. A CAD model of the beam pipe is drawn in full scale according to the 3D printed model, see figure 8.7. To simplify the simulation, the water cooling system is not included in this model at this moment. The octagonal structure at the middle of the pipe is eliminated in this model as well. The model is attached on both ends of the inner detector. It acts simply as an
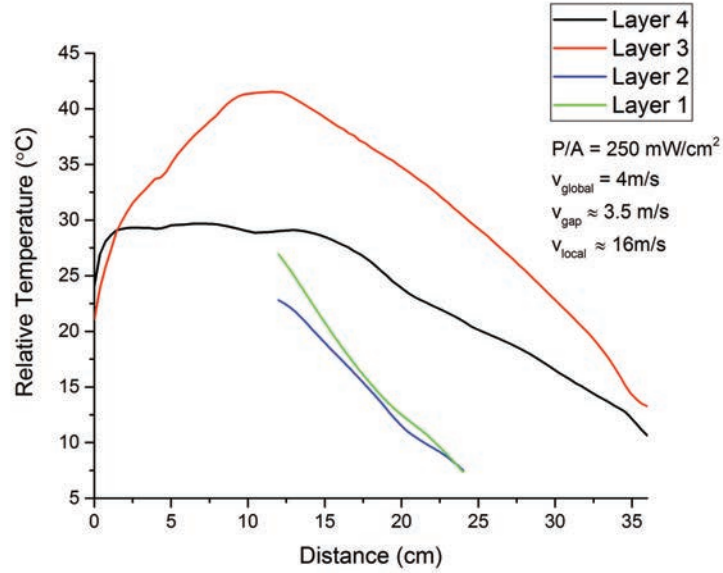
Figure 8.4: Temperature profile for the central detector station with inner detector and target ;
$P/A = 250mW/cm^2$, $v_{local} \approx 16m/s$, $v_{gap} \approx 3.5m/s$, $v_{global} = 4m/s$, $T_{He} = 0°C$
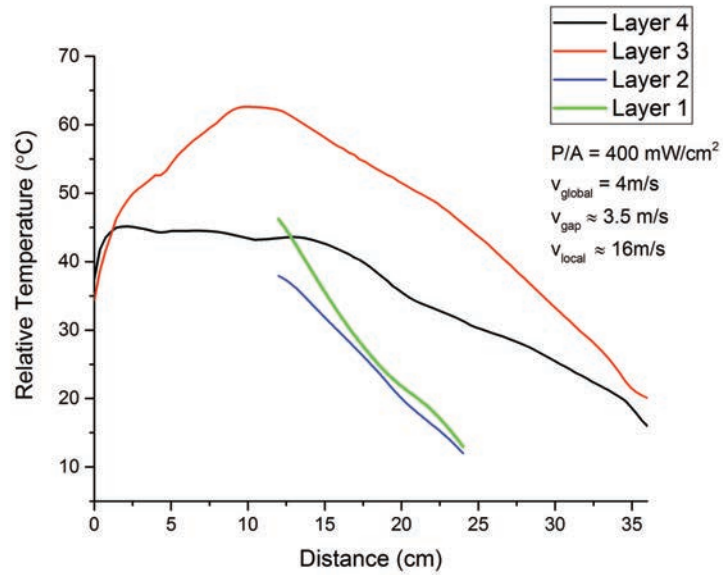
Figure 8.5: Temperature profile for the central detector station with inner detector and target ;
$P/A = 400mW/cm^2$, $v_{local} \approx 16m/s$, $v_{gap} \approx 3.5m/s$, $v_{global} = 4m/s$, $T_{He} = 0°C$

obstacle for the global helium flow inside the detector stations. Here, the model is tested with the outer detector station and inner detector station, under the same condition as in section 8.1.

The temperature profiles of the phase 1a detector with $250mW/cm^2$ and $400mW/cm^2$ heating power are shown in figure 8.8a and 8.8b. The temperature profile for the outer detector layer behaver similarly to the simulation in section 8.1. However, the temperature profile for the inner detector raises vigorously. It can be explained by the factor that the beam pipes are located very close to the inner detector, which blocks most of the helium global flowing into the inner station. Therefore, a extra flow channel is needed for the inner detector.
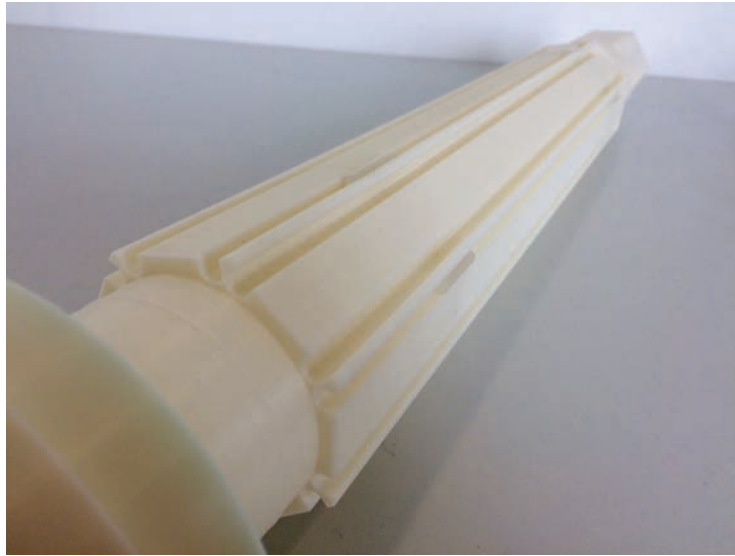
Figure 8.6: 3D printed model for the preliminary design of the water cooling system
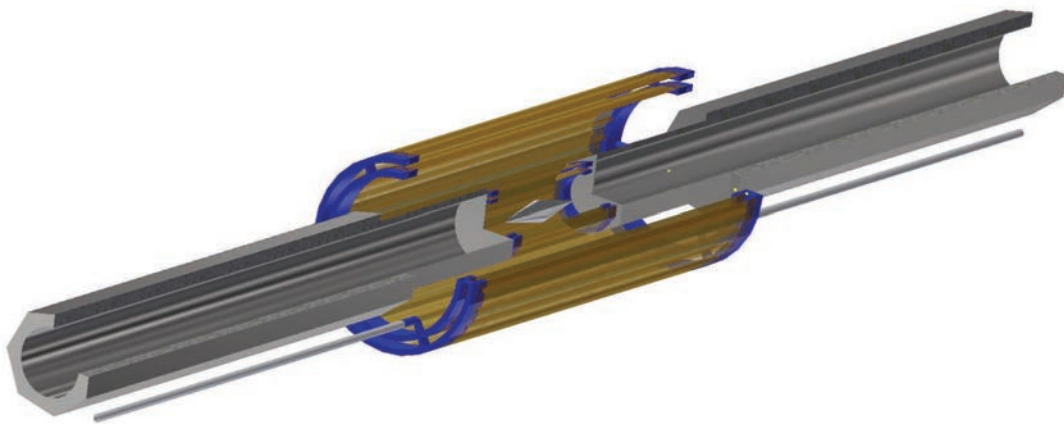
Figure 8.7: Model of the pixel detector station with a beam pipe as obstacle

(a)   (b)
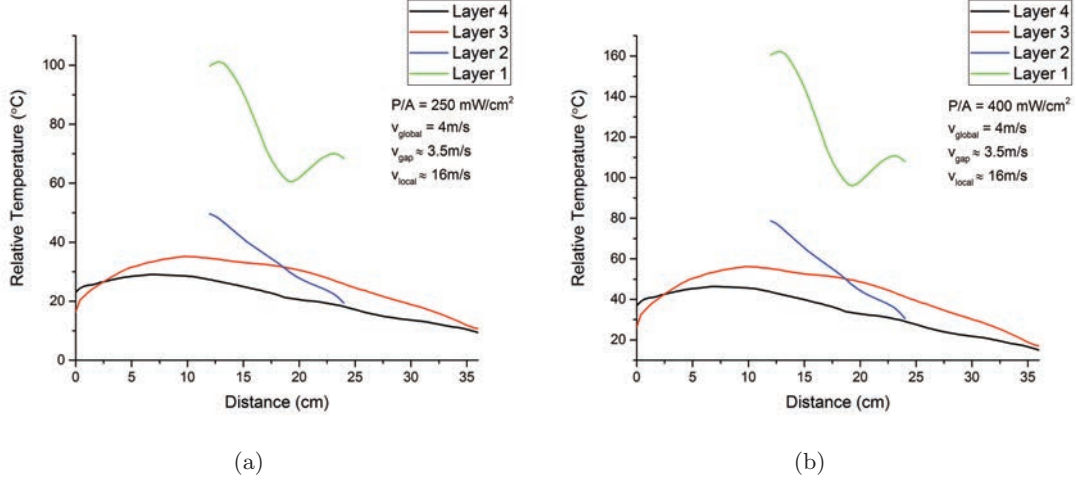
Figure 8.8: Temperature profile of outer and inner with beam pipe as obstacle; P/A = (a) $250mW/cm^2$ and (b) $400mW/cm^2$, $v_{local} \approx 16m/s$, $v_{gap} \approx 3.5m/s$, $v_{global} = 4m/s$, $T_{He} = 0°C$

Beam Line with gas distribution system

From the previous simulation, it has been learned that the global helium flow is unable to reach the inner detector effectively to provide sufficient cooling power. Therefore, it is proposed to design a extra helium inlet to provide cooling for the inner detector. So as to demonstrate the extra helium input, a channel is integrated into the CAD model of the beam line. The channel will provide a helium flow rate of 4m/s to the inner detector, which is the same as the global flow rate as the outer layer. The flow velocity of this extra channel is labeled as v_{inner} One ought to mention that this design is a premature solution which has the purpose to demonstrate a flow inside the inner detector station. The inlet will be implemented with a different structure for the real detector but the condition will be similar to the simulation. Figure 8.9 shows the central detector equipped with the modified beam line. The flow channel for the inner detector is located at the center along the beam line.

The model is simulated under the same boundary condition as in section 8.1 with one additional constraint :

- $v_{inner} = 4m/s$ at the right end of the beam pipe inlet

The temperature profiles of the simulation with heating power of $250mW/cm^2$ and $400mW/cm^2$ are shown in the figure 8.10a and 8.10b. By adding the helium cooling channel for the inner detector, the temperature around the center is efficiently cooled down. However, the temperature at the left end of layer 1 is still higher than the upper limit of the working temperature for the $400mW/cm^2$ simulation. It can be explained by the lack of flow inside the layer 1 detector barrel. With the current design, it is insufficient to provide enough cooling power to the inner station, which will become the hottest region in the Mu3e detector. Therefore, a cooling channel for the inner detector is needed in order to provide extra cooling power. However, the design must be designed with caution as a gas flow inside the inner station may induce vibration on sensors and even stopping target, eventually influencing the vertex resolution of the detector.
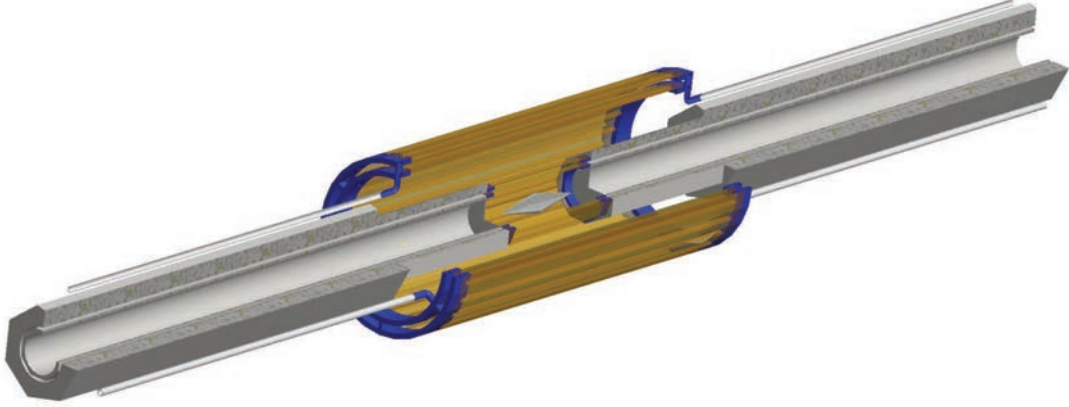
Figure 8.9: CAD Model of the central detector station (outer and inner) and beam pipe with global distribution

(a) (b)
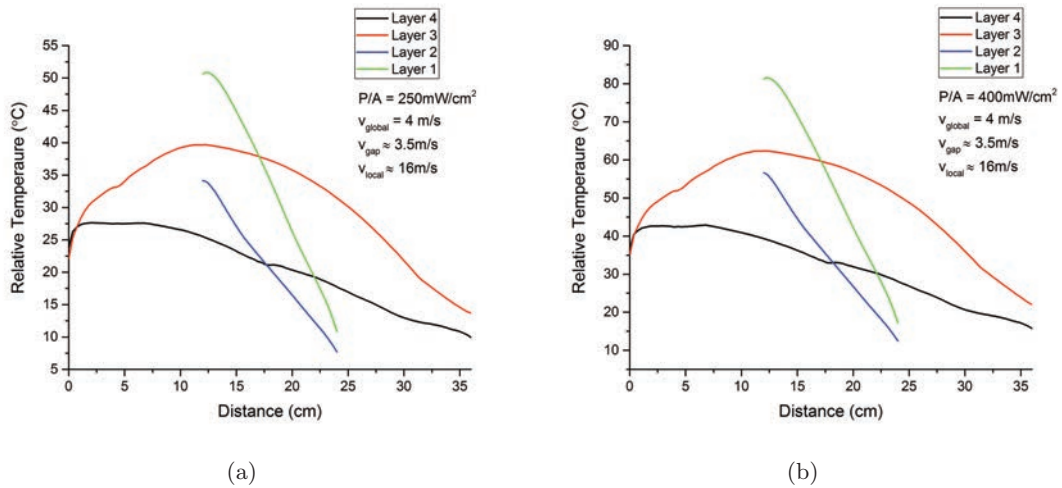
Figure 8.10: Temperature profile of outer and inner detector with global cooling channel in beam pipe; $P/A =$ (a) $250mW/cm^2$ and (b) $400mW/cm^2$, $v_{global} = 4m/s$, $v_{local} \approx 16m/s$, $v_{gap} \approx 3.5m/s$, $v_{inner} = 4m/s$, $T_{He} = 0°C$

8.3 Time of Flight Detector

The Time of Flight detector consists of cylindrical stations of scintillating fibers and scintillating tiles. The scintillating fiber station is located inside the layer 3 in the central station, and the scintillating tile stations are located inside each of the recurl station. Both of the stations are in a barrel shape with 24 sides. For the cooling system, the geometry acts as a flow guide for the global flow in the center region. To understand how these barrels would affect the cooling, a preliminary model of the fiber and tile stations are used to simulate the helium flow inside the detector.

The scintillating fiber detector is a 24 sided barrel. It is constructed by putting 24 fiber ribbons

together. Each of the ribbons has a size of 16mm x 360cm, with a thickness of 750 μm. The CAD model of the fiber detector is shown in figure 8.11. The scintillating tile detector has a similar structure as the fiber detector, it is only different in thickness. The detector will be about 5mm thick. The CAD model of the scintillating tile detector is shown in figure 8.12.

Figure 8.13 shows the Phase Ib detector model without the water cooling system by adding 2 recrul station and time of flight detectors. The simulation of this model gives a preliminary prediction to the cooling performance in Phase Ib. Simulations with the same boundary conditions as section 8.1 have been carried out. The temperature profiles of the sensor layer with heating power of $250mW/cm^2$ and $400mW/cm^2$ are plotted in figure 8.14 and 8.15. A maximum of $60°C$ is found in the central station in the $250mW/cm^2$ simulation, which fall within the upper limit of the working temperature of MuPix. However, with such boundary condition, the maximum temperature for the $400mW/cm^2$ simulation exceed the upper limit of $70°C$ and reach $91°C$.
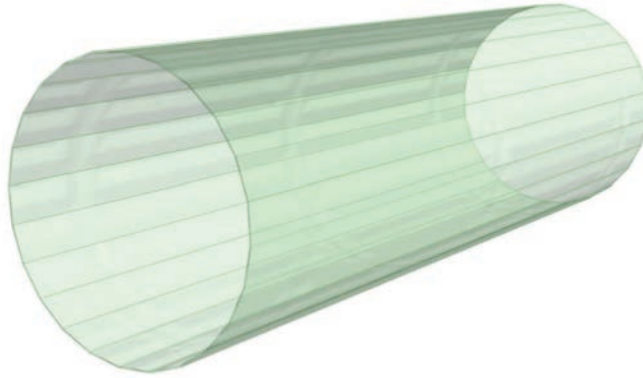
Figure 8.11: Model of the scintillating fibre detector

Figure 8.12: Model of the scintillating tile detector
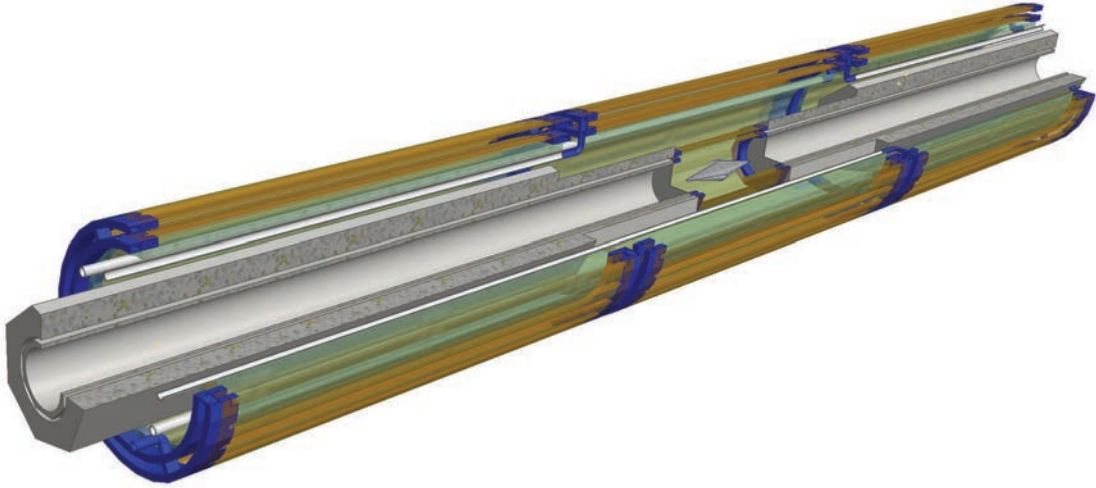
Figure 8.13: Model of the Phase Ib detector
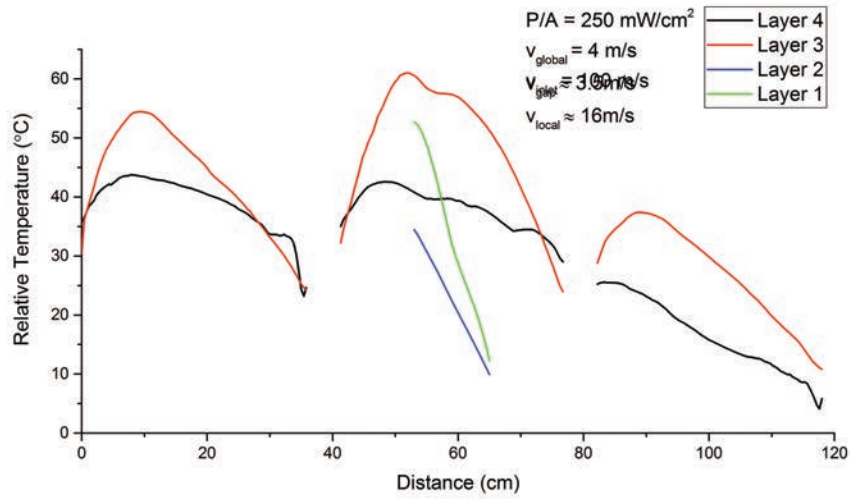
Figure 8.14: Temperature profile of Phase Ib detector without water cooling system; $P/A = 250mW/cm^2$, $v_{global} = 4m/s$, $v_{local} \approx 16m/s$, $v_{gap} \approx 3.5m/s$, $v_{inner} = 4m/s$, $T_{He} = 0°C$
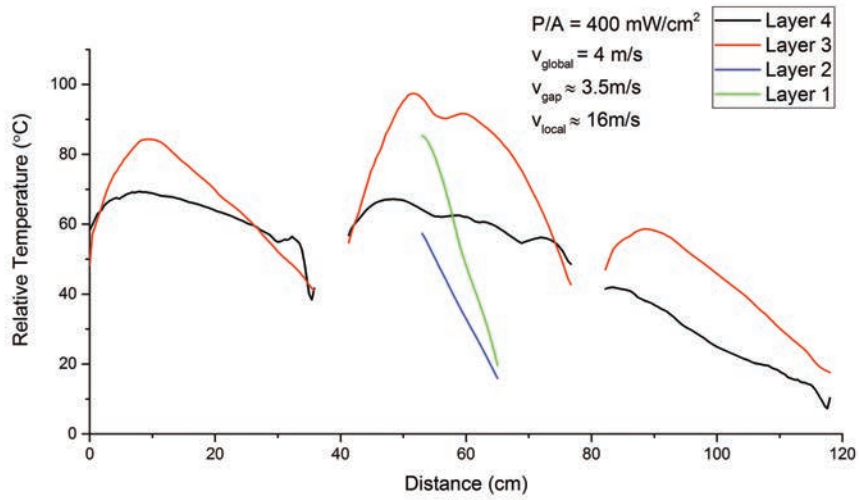
Figure 8.15: Temperature profile of Phase Ib detector without water cooling system; $P/A = 400mW/cm^2$, $v_{global} = 4m/s$, $v_{local} \approx 16m/s$, $v_{gap} \approx 3.5m/s$, $v_{inner} = 4m/s$, $T_{He} = 0°C$

Chapter 9

Water Cooling System

In order to provide cooling power to the FPGA Chips, a water cooling system is designed.

9.1 Single Heat Sink

A prototype of a heat sink for the water cooling system with only one block of the heat sink is built and tested in section 3.2. In order to compare with the test result, the CFD simulation for the water cooling system is first carried out with the model with the dimensions of the prototype of the heat sink. The CAD model of the prototype is drawn under Autodesk® Inventor. The heat sink is a steel block with dimension of $410mm \times 36mm \times 10mm$. An U shaped channel is milled in the block to act as the water flow channel.

Heating with Heating Resistor

The heat sink is equipped with 4 heating resistors with heatable aluminum core surrounded by a copped shell, see figure 9.1. The material type for the model is set corresponding to the prototype with default values provided by the program. To compare the results with the cooling test in section 3.2, the simulation conditions are similar to the ones in the lab-test. As the cooling test is performed in laboratory with room temperature of $20°C$, the temperature of the coolant is set to $20°C$. In the simulation the model is contained in a chamber of air with boundary condition of $20°C$ and supplied with water coolant at $20°C$. The flow rate of water coolant inside the heat sink is adjusted to the laboratory test. In the cooling test, the water is pumped by a cooler. The model was first tested with the flow rate value according to the factory specification of the device, but the resulting temperature is far below the one in the experiment. Considering that the water doesn't flow directly in the heat sink, the flow rate may be much lower than the value listed in the specification. Therefore a measurement of the flow rate in the heat sink is done. It is carried out by counting the time the water pump takes to fill a measuring cylinder. The water pipe at the inlet is unplugged and inserted into a 1 liter measuring cylinder. As the water pump is located at the floor and the heat sink is on a table, the flow rate of the water at the inlet is affected by the height of the table. In order to get a proper result, the mouth of the cylinder is place near the level of the heat sink and the water pipe is fixed horizontally on the mouth of the cylinder. The flow rate v_{water} is calculate by dividing the volume of the cylinder V by the record time t and area of the water pipe A_{pipe}:

$$v_{water} = \frac{V}{t \cdot A_{pipe}} \tag{9.1}$$

By timing the filling process for five times, the average time for filling the 1L vessel is found to be $46.35s$. Hence, the flow speed in the 4.5mm inlet is calculated to be $v_{water} = \frac{1000/46.36}{0.225^2\pi} = 135.69cm/s = 1.36m/s$. Therefore, the boundary is set as following :

- heat flux on each resistor core, distributed over the whole volume : $P = 50W$

- constant velocity on water inlet : $v_{water} = 1.36m/s$

- zero overpressure on water outlet

- constant temperature on the water inlet : $T_{water} = 20°C$

- constant temperature on each side of the air chamber : $T_{air} = 20°C$
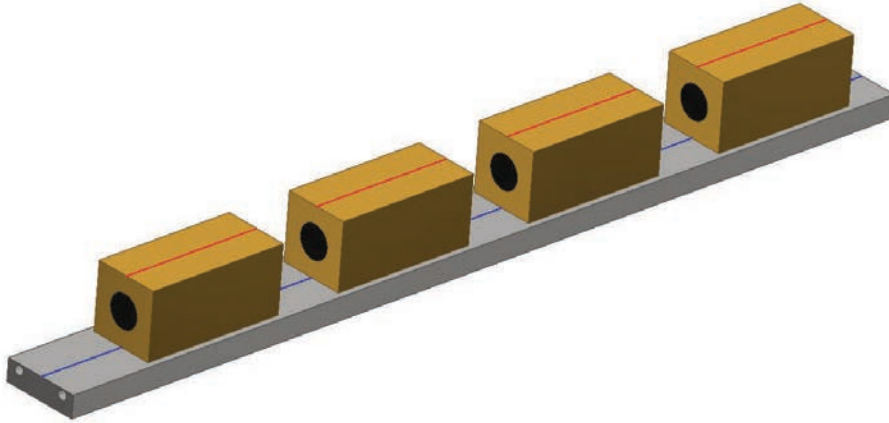
Figure 9.1: CAD model of a single beamline heat sink with heating resistor as heat source

The temperature profile of the heat sink and the heating resistors is plotted against distance from inlet in figure 9.2. Here, the value is shown as the exact temperature. The red line represents the temperature on the top of the resistor, which is the same location as for the temperature sensor in the cooling test in section 3.2. The blue line represents the temperature on the surface of the heat sink, along the center line. The locations are indicated with corresponding colored lines in figure 9.1. The simulation is compared with the cooling test result. It shows a temperature difference of about $27°C$ between the test and the simulation. Such large difference can be explained by two factors. First, the heat sink prototype in the cooling test has a very rough surface. As the heating resistor is attached on the heat sink by mechanical mounting with thermal cooling paste in between, it is possible to leave some air in the contact area which results in to a poor heat conduction. This can significantly raise the temperature of the resistor. The simulation suggests that the cooling ability of the heat sink can be potentially increased by improving the contact surface. Referring to the design of the heat sink for computer processor, it is also suggested to add a copper layer with polished surface on the contact area to increase the thermal conductivity. Second, the cooling capability is somehow limited by the cooling device. As the maximum cooling power of the cooling device is only 150W, which is 50W lower than the total heating power, it is insufficient to carry away all the heat dissipated on the heat sink. In fact the temperature of the water coolant in the cooling tank raises by $3°C$ after reaching equilibrium, despite it is programed to keep the coolant

at $20°C$. This can be simply improved by using cooling device with higher cooling power or adding extra cooling devices. The simulation indicates that the efficiency of the water cooling in the test is inconclusive. One has to repeat the water cooling test with better prototype and cooling device. A heat sink with fine contact surface and a cooling device with sufficient cooling power are required.
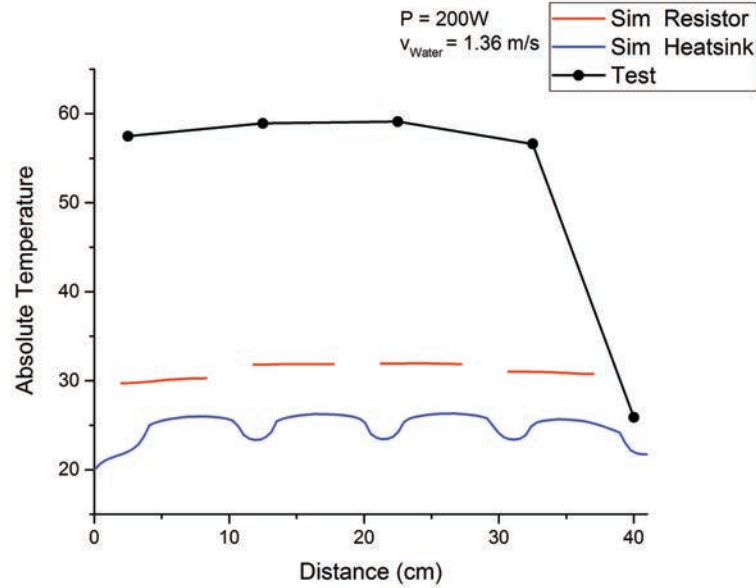
Figure 9.2: Temperature profile for the single heat sink heated with resistor, $v_{Water} = 1.31 m/s$, $P_{resistor} = 200W$, $T_{water} = 20°C$, compare with cooling test

Simulation with FPGA Chip

To describe the situation more close to the design of the Mu3e water cooling system, the heating resistor CAD model is replaced by a FPGA chip model. The FPGA chip model is a silicon segment with the size of 36mm x 400mm and a thickness of 1mm.

The model is simulated in similar boundary conditions as the previous section, except the heat flux and the environment constrain :

- Instead of a discrete heat source, the total heat flux is dispersed over the FPGA chip, ranging from 100W to 300W

- To study the cooling ability of the heat sink, the model is simulated alone and isolated from the environment, i.e. no environment constraint is added

- Water at $T_{water} = 0°C$

In figure 9.4, the relative temperature of the heat sink to several heating assumption are plotted against the distance from the water inlet. A gradual increase in temperature is observed with the increase of heating power for each 100W intervals. The temperature profile for the 200W simulation is lower than the one with heating resistor (figure 9.2). This can be explained by the factor that the heat source is in direct contact to the heat sink with a larger contact area.

71
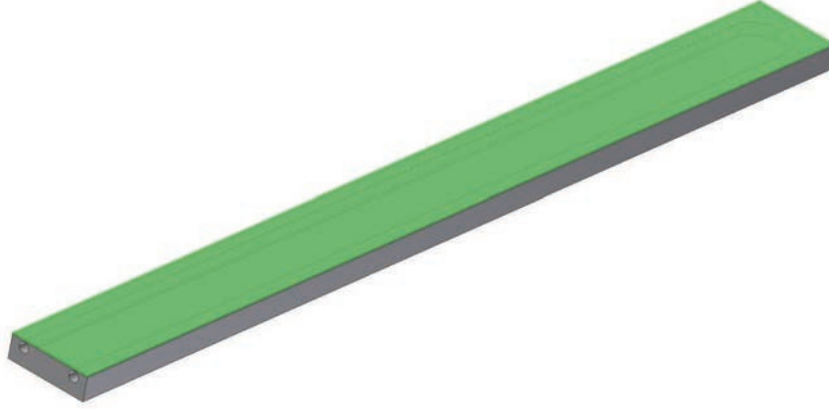
Figure 9.3: CAD model of a single beamline heat sink with a FPGA segment as heat source
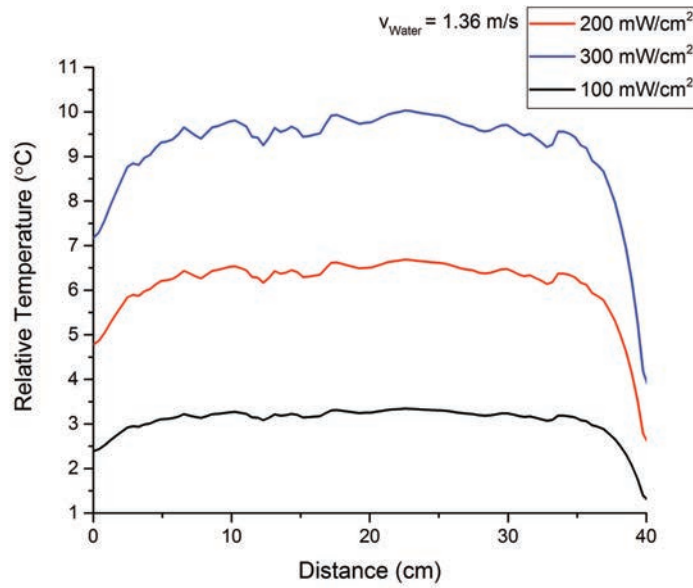
Figure 9.4: Relative temperature for the single heat sink heating with segment, $v_{Water} = 1.31 m/s$, $T_{water} = 0°C$

9.2 Integrated Heat Sink

To investigate the cooling ability of the water cooling system in the experiment, the heat sink is integrated into the beam pipe model in section 8.2. There are 7 sets of water cooling pipes in the beam pipe right under the FPGA chips. The water pipes are in U shaped with a size identical as for the single heat sink model. The in- and outlets are located at the end of the beam pipe,

and will be outside the detector stations. FPGA segments are attached on each of the sides of the heptagon and act as a heat source. The integrated heat sink is made of steel and FPGA segments are assigned with silicon to simulate the cooling effect. The same boundary conditions as in section 9.1 are applied to the model. The result is illustrated in figure 9.6 with relative temperature. In figure 9.7, the temperature profile of one of the heat sinks at a heating power of 200W is plotted against the distance from the water inlet. The temperature is slightly higher than the one with a single heat sink (figure 9.4) but similar shape.
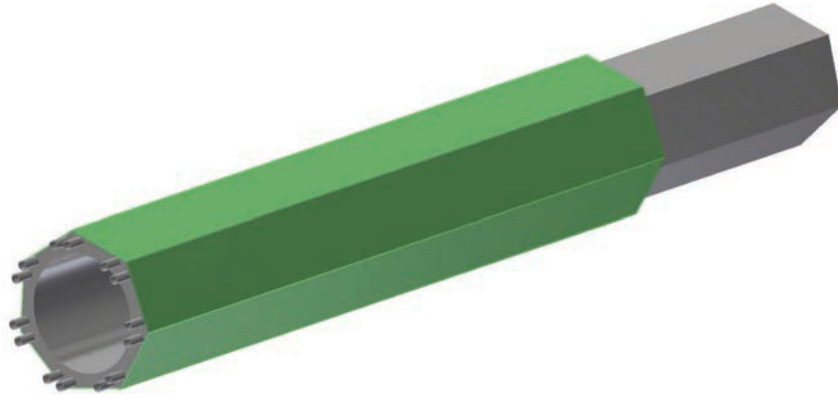
Figure 9.5: CAD model of the beamline integrated with heat sink and FPGA segment
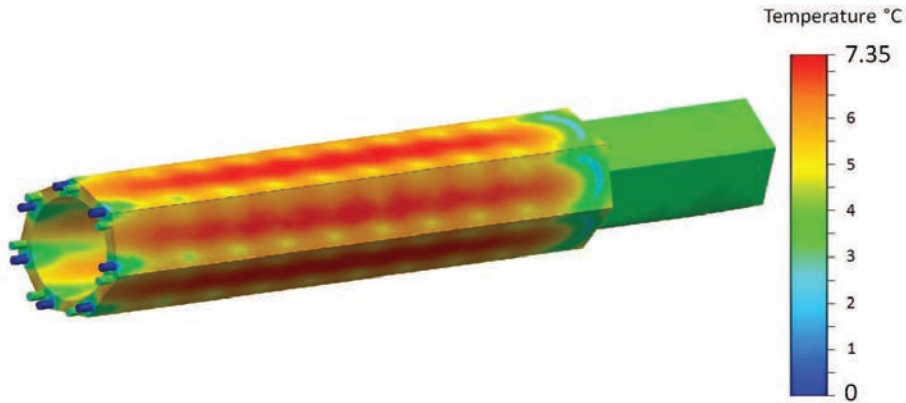
Figure 9.6: Simulation of beam pipe with FPGA chip and water cooling system, $v_{Water} = 1.31 m/s$, $P_{resistor} = 200W$, $T_{water} = 20°C$, compare with cooling test
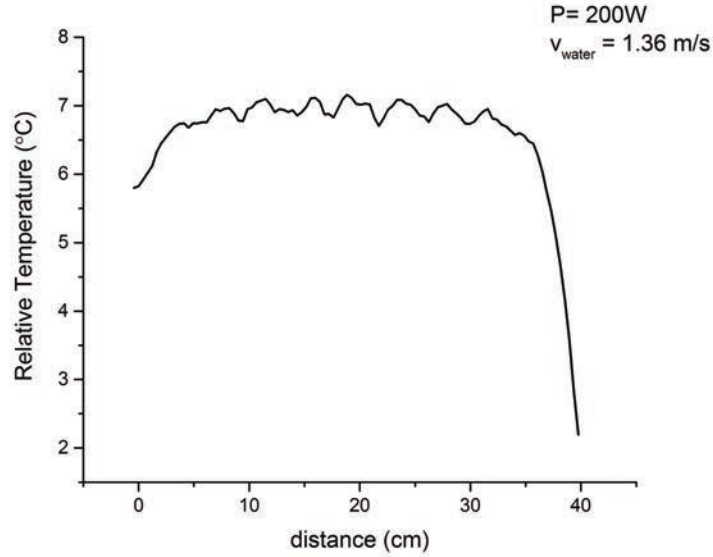
Figure 9.7: Temperature profile for the integrated heat sink, $v_{Water} = 1.31m/s$, $P_{resistor} = 200W$, $T_{water} = 0°C$, compare with cooling test

9.3 Simulation for Phase I Mu3e Detector

Up to this point, the model has included all of the major components of the Mu3e Detector. It includes the outer detector station (central and recurl), the inner detector station, the stopping target, the time of flight detector (scintillating fiber detector and scintillating tile detector), FPGA chips and beam pipe with water cooling system. Here, the detector models for the Phase I of the Mu3e experiment are simulated. The results can give a preliminary picture of the performance of the cooling system and be a reference for further improvements of the design.

The Phase I experiment is divided into two stage. Phase Ia is to study the technology and verify the concept of the experiment using the detector with minimal configuration, while already pushing the sensitivity down to $\mathcal{O}(10^{-14})$. The phase Ia detector consists of the central station (outer and inner detector station), stopping target, FPGA chips and the beam pipe. The CAD model for the phase Ia detector is shown in figure 9.8. Phase Ib will be completed by adding two outer detectors upstream and downstream as recurl stations, and the time of flight detectors. The configuration will significantly enhance the momentum and time resolution, thus improving the suppression of backgrounds. The sensitivity will be pushed to $\mathcal{O}(10^{-15})$ in this phase. The CAD model for the phase Ib detector is shown in the figure 9.9.

Each of the detector models is simulated under the boundary condition :

- Total heat flux on silicon sensors, corresponding to $P/A_{sensor} = 250mW/cm^2$ and $400mW/cm^2$

- Total heat flux on each FPGA segment, $P_{FPGA} = 200W$ per segment

- constant velocity at each end-ring helium inlet, $v_{inlet} = 100m/s$ ($v_{local} \approx 16m/s$ and $v_{gap} \approx 3.5m/s$)

- constant velocity at the right end of the flow tunnel, $v_{global} = 4m/s$, $v_{inner} = 4m/s$

- constant velocity at each water inlet on the beam pipe, $v_{water} = 1.36m/s$

- zero overpressure for all outlets

- Temperature constraint on all helium and water inlets, $T_{He} = 0°C$; $T_{Water} = 0°C$
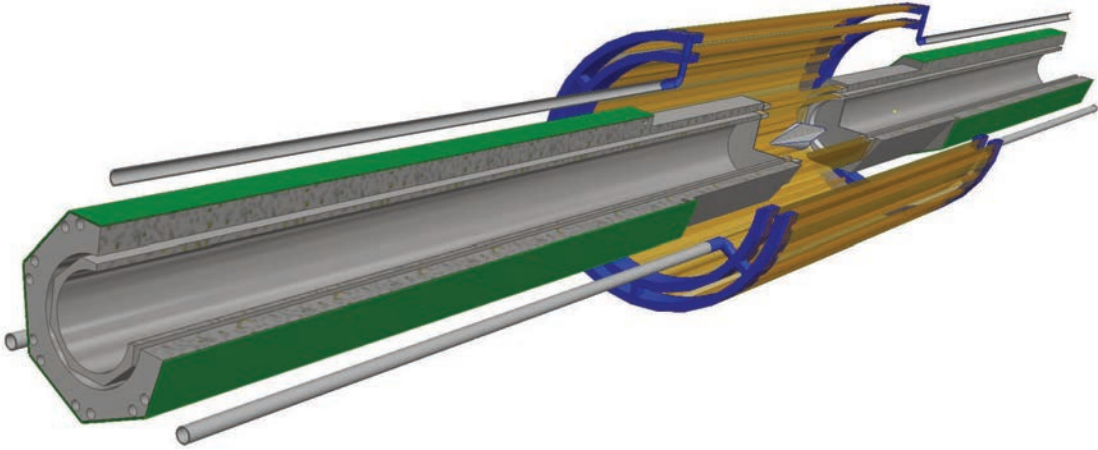
Figure 9.8: Model of the Phase Ia detector with water cooling system

The result of simulation for phase Ia and Ib models at $250mW/cm^2$ is shown in figure 9.10 and 9.11 with temperature indicated as color. The temperature of the both detectors for above parameters fall within the upper limit of $70°C$. The temperature profiles for each simulation are plotted in figure 9.12 and 9.15. The flow profiles for each simulation are shown in figure 9.13 and 9.14.

The result of simulation for phase Ia and Ib models at $400mW/cm^2$ is shown in figure 9.12b and 9.15b. In this condition the peak temperature of both detector exceed $70°C$. For the case of phase Ia model, only the temperature of layer 1 exceed the limit. Therefore, it can be solved by improving the flow in the inner layer by implementing a local flow channel in the detector. For the case of phase Ib model, as the layer 3 in all station reach a temperature above $70°C$, the cooling design for the outer station also has to be improved. Two ideas of the improvement in local cooling are discussed in chapter 10.

In conclusion, the cooling design is sufficient for the phase I experiment only if the power consumption is less than $250mW/cm^2$. For the case of $400mW/cm^2$ the cooling has to be improved.
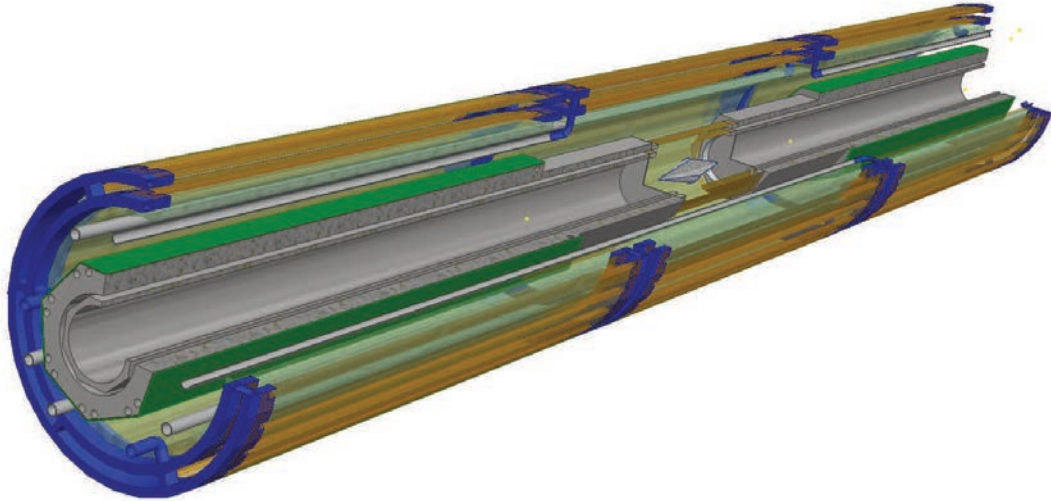
Figure 9.9: Model of the Phase Ib detector with water cooling system
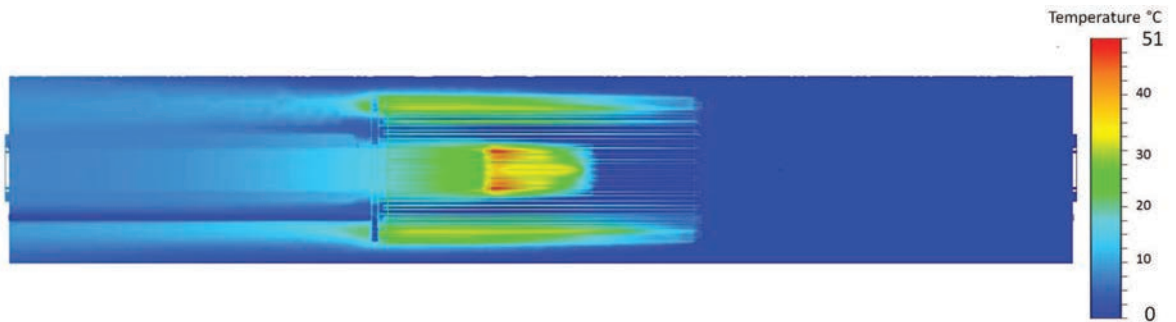
Figure 9.10: The result of simulation with the phase Ia detector, $P/A_{sensor} = 250mW/cm^2$, $P_{FPGA} = 200W$, $v_{global} = 4m/s$, $v_{local} \approx 16m/s$, $v_{gap} \approx 3.5m/s$, $v_{inner} = 4m/s$, $T_{He}, T_{Water} = 0°C$
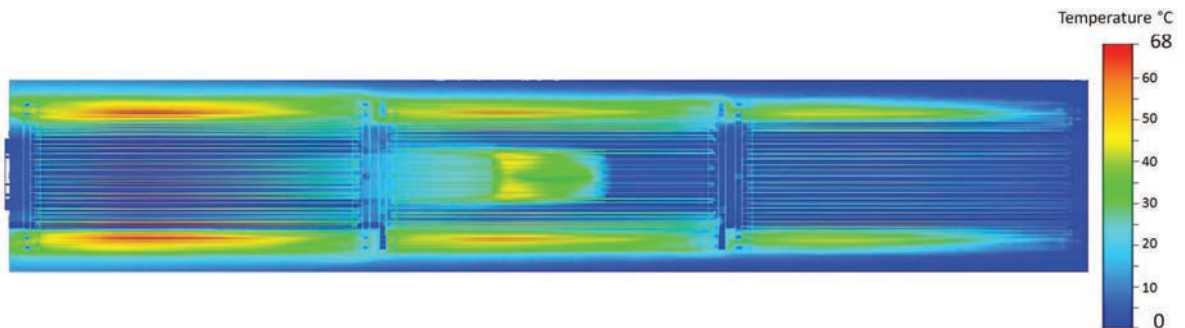
Figure 9.11: The result of simulation with the phase Ib detector, $P/A_{sensor} = 250mW/cm^2$, $P_{FPGA} = 200W$, $v_{global} = 4m/s$, $T_{He}, T_{Water} = 0°C$

76

(a)

(b)
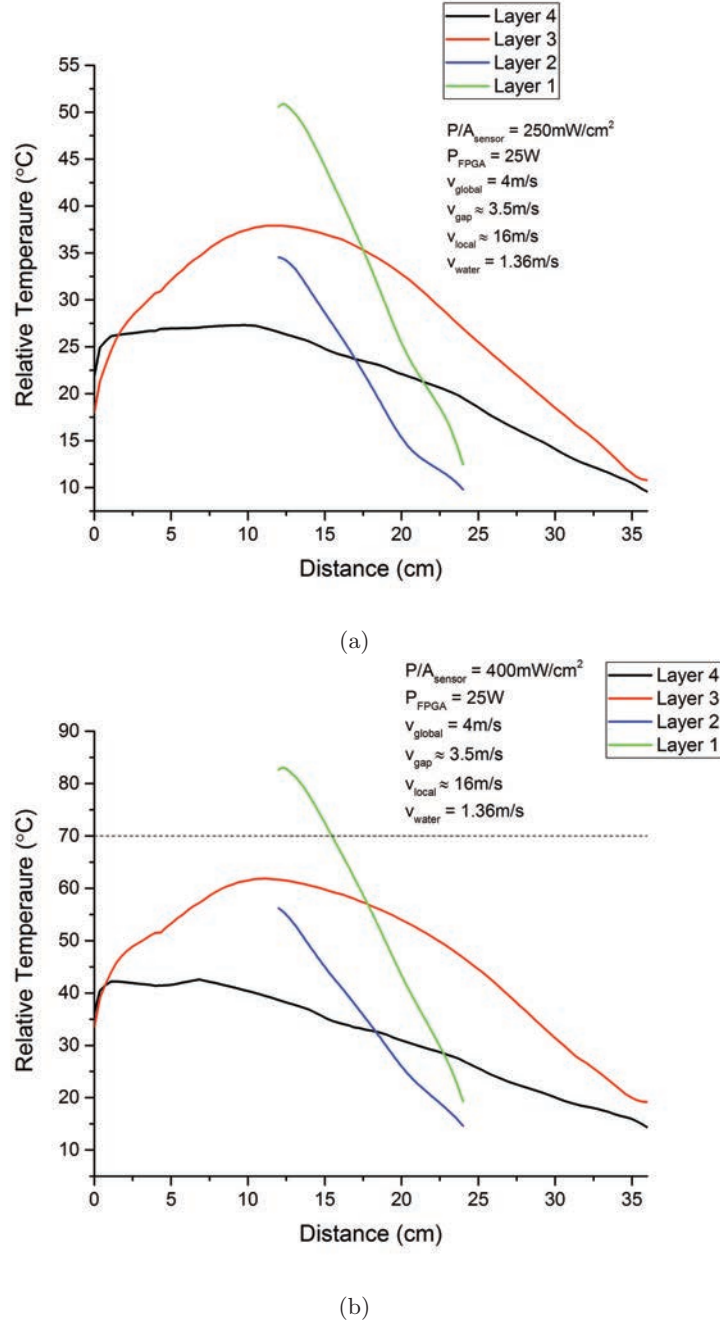
Figure 9.12: Temperature profile of the simulation with phase Ia detector, $P_{FPGA} = 200W$, $v_{global} = 4m/s$, $v_{local} \approx 16m/s$, $v_{gap} \approx 3.5m/s$, $v_{inner} = 4m/s$, $T_{He}, T_{Water} = 0°C$, $P/A_{sensor} = 250mW/cm^2$ (a) and $400mW/cm^2$(b)
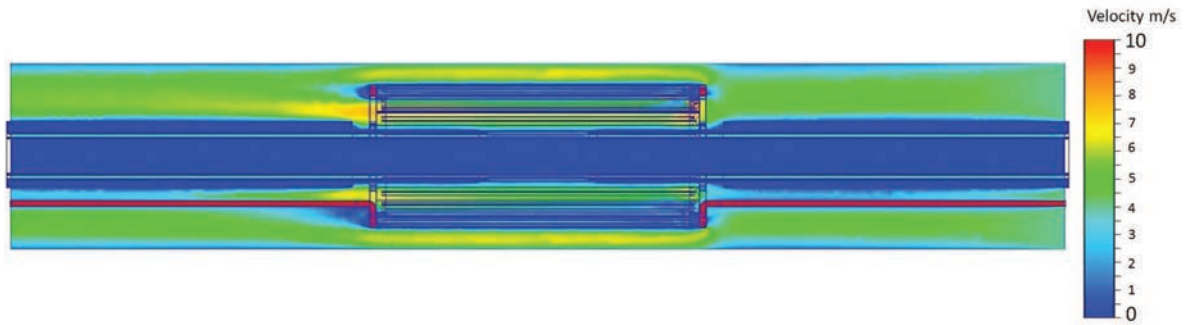
Figure 9.13: The flow profile of the simulation with the phase Ia detector, $P/A_{sensor} = 250mW/cm^2$, $P_{FPGA} = 200W$, $v_{global} = 4m/s$, $v_{local} \approx 16m/s$, $v_{gap} \approx 3.5m/s$, $v_{inner} = 4m/s$, $T_{He}, T_{Water} = 0°C$
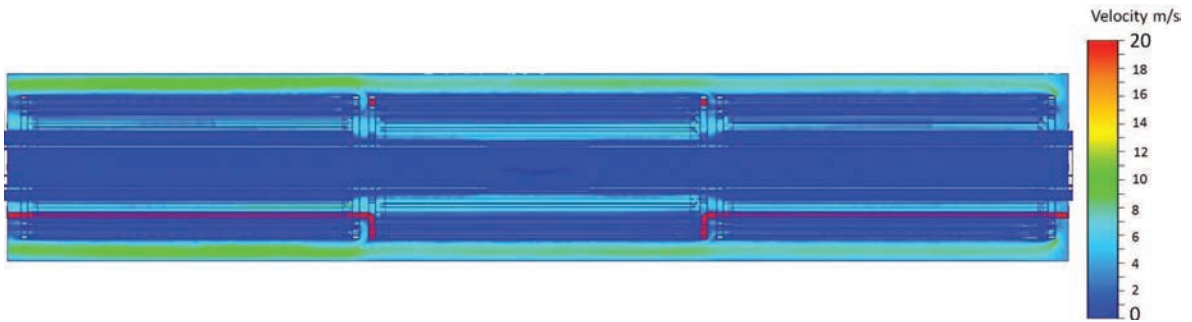
Figure 9.14: The flow profile of the simulation with the phase Ib detector, $P/A_{sensor} = 250mW/cm^2$, $P_{FPGA} = 200W$, $v_{global} = 4m/s$, $v_{local} \approx 16m/s$, $v_{gap} \approx 3.5m/s$, $v_{inner} = 4m/s$, $T_{He}, T_{Water} = 0°C$
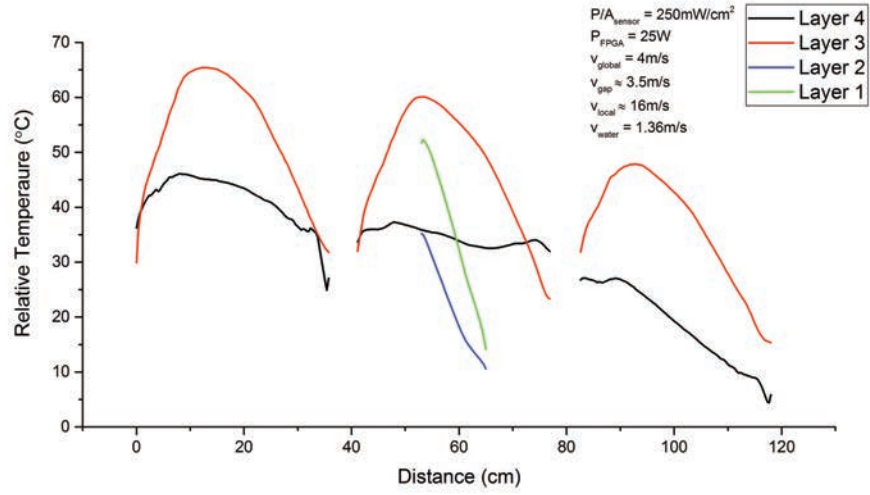
(a)
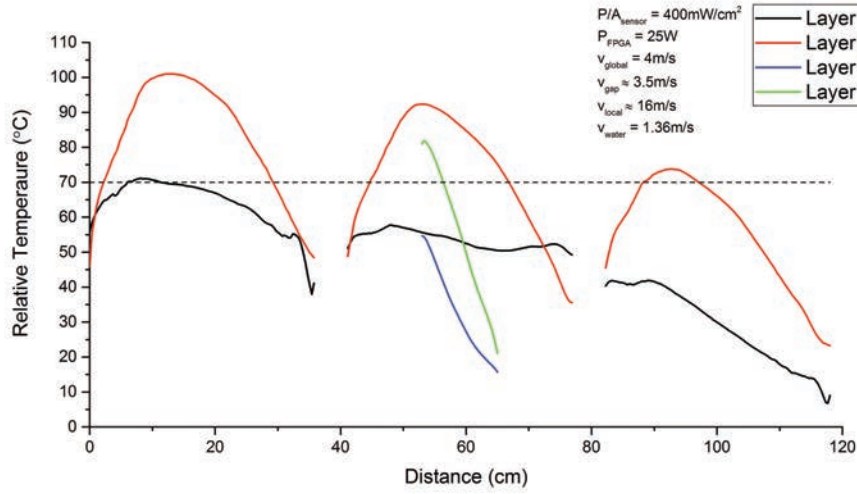
(b)

Figure 9.15: Temperature profile of the simulation with phase Ib detector, $P_{FPGA} = 200W$, $v_{global} = 4m/s$, $v_{local} \approx 16m/s$, $v_{gap} \approx 3.5m/s$, $v_{inner} = 4m/s$, and $T_{He}, T_{Water} = 0°C$, $P/A_{sensor} = 250mW/cm^2$ (a) and $400mW/cm^2$ (b)

Chapter 10

Modification of the Local Flow Channel

The local flow channel plays an important role in the performance of the cooling system. Together with the global flow coming from the opposite direction, the cooling system can lower the temperature of the Mu3e detector significantly [2]. The local flow channel consists of two main components: the gas distribution system in the supporting end-structure and the V-shaped Kapton® foil. The gas distribution system in end-ring has been redesigned and optimized for material budget and uniform gas distribution, see chapter 7. However, the design for the V-shape design has never been reviewed. To improve the cooling ability of the V-shapes, the concept is to increase the contact area to the heat source. It can be achieve by either increasing the number of V-shaped folds or by enlarging the structure. In this chapter, two of the proposed modifications to the V-shaped structure will be discussed : the double fold Design and the Large fold design. Both designs have been drawn in CAD format and simulated under Autodesk® CFD. The results will be compared with the original design.

10.1 Double Fold Design

To improve the cooling ability of the Kapton® supporting structure, the idea is first to increase the number of such V-shaped folds to two per sensor segment. The double amount of V-shaped folds increases the contact area between the coolant and sensor segment. This design also allows two local flows in opposite direction under each sensor segment. A model for a module of the design is shown in figure 10.1. The size of the module is the same as the baseline design, but with twice the number of local flow channels. The original channel is label as local channel 1 and the additional channel with opposite flow direction as local channel 2. The dimensions of the fold is kept the same.

Analysis

The model for one station is constructed by duplicating cylindrically the module in axial direction. The flow pattern is shown in figure 10.2. As the gas in the double fold design will flow in pairs with opposite direction, another gas inlet is needed for the reverse channel at the other end. The first attempt is to integrate the inlet into the gap end-ring by adding outlet holes on the gas chamber and double the flow rate at the inlet. This integrated end-ring is renamed as Local+Gap end-ring. The model is contained in a helium flow tunnel for simulation. The model is simulated under the
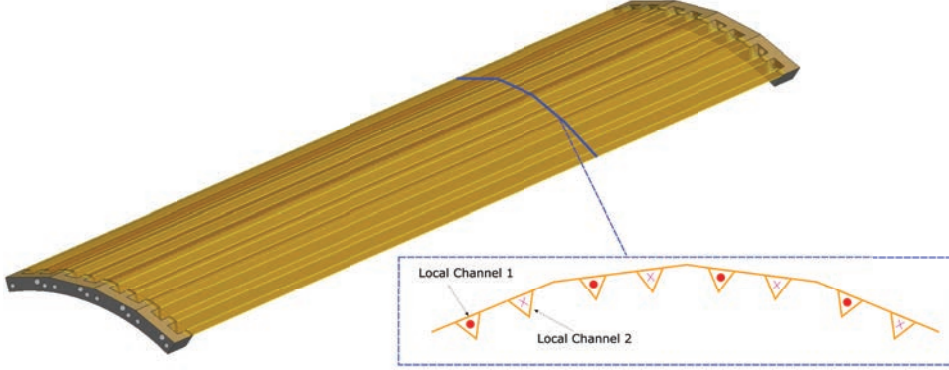
Figure 10.1: CAD model for a module for the double local cooling design

following boundary condition :

- Total Heat Flow on the silicon segment, corresponds to $P/A = 400 mW/cm^2$

- $v_L = 100 m/s$ for inlet at local end-ring

- $v_{G+L} = 200 m/s$ for inlet at local+gap end-ring

- $v_{global} = 4 m/s$ at the right end of the flow tunnel

- $T_{He} = 0°C$ for all inflowing helium

- zero overpressure at the left end of the flow tunnel

The temperature profile of the simulation is plotted in figure 10.3. Despite the increase in flow rate and number of local channels, the change in temperature profile is smaller than expected. The temperature at the right end decreases due to the extra local flow channel following form the right, but the maximum temperature remains unchanged. From figure 10.4, one can see that the flow velocity at the additional local channel (b) is much lower than for the others (a). A significant decrease in flow velocity at the gap between 2 layers is observed as well. This explains the inefficiency of this design. It can be accounted to the nonuniform output of the gas distribution system, which is an outcome of the increase of inlet velocity, as indicated in section 7.2. The flow velocity at the outlet of the right endring is shown in figure 10.5. It can be seen that the output into the local flow channel is very limited. Also, the output into the global channel is concentrated in the inner ring, which goes to the center region instead of the gap between 2 layers.
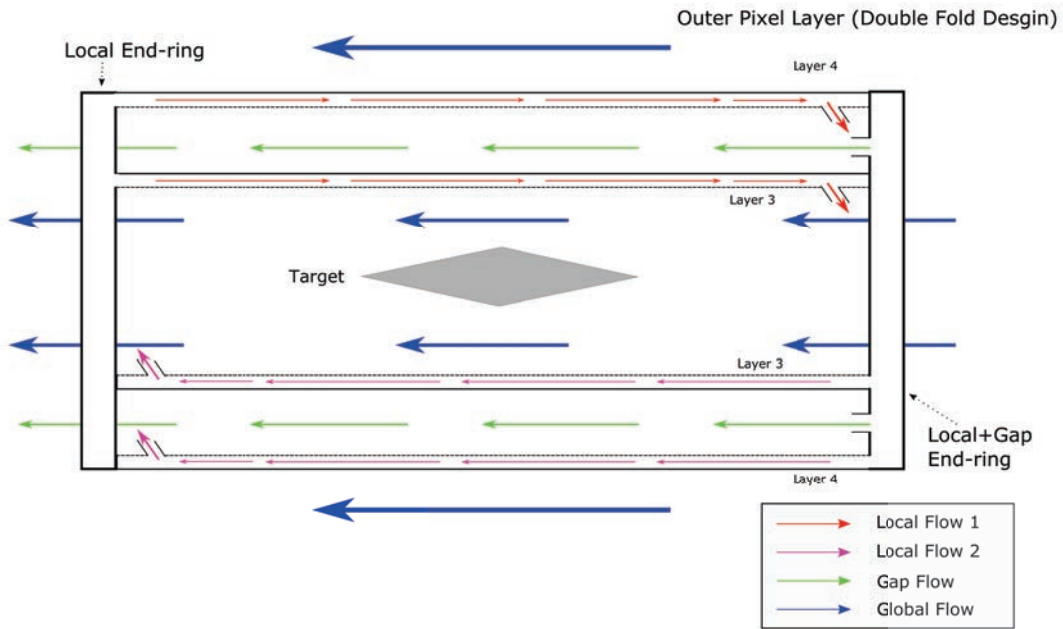
Figure 10.2: Schematics for the flow pattern of the double flow design
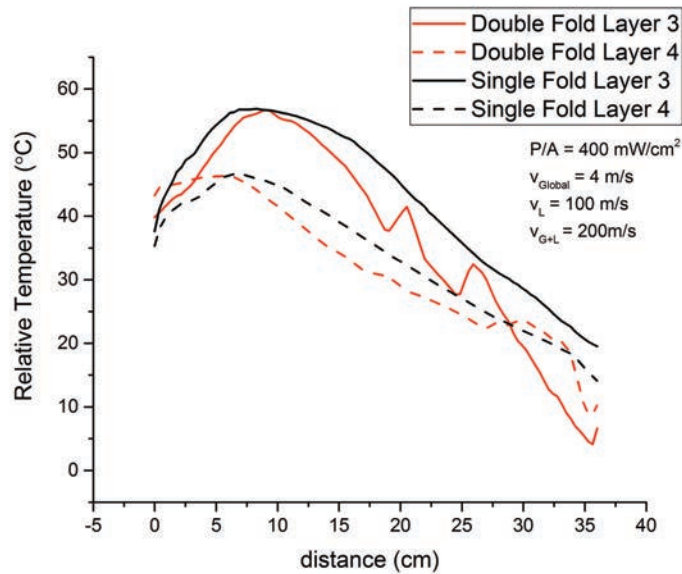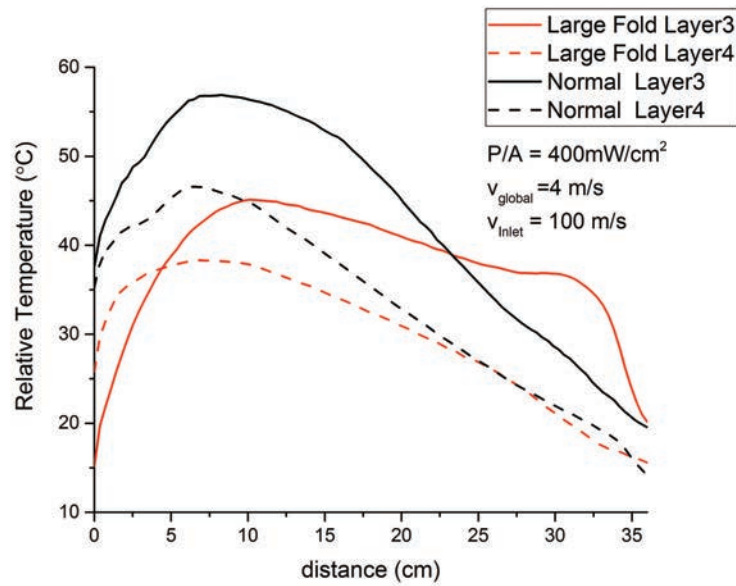

Figure 10.3: Temperature profile of the detector station with double fold design, $P/A = 400mW/cm^2$, $v_{global} = 4m/s$, $v_{G+L} = 200m/s$, $v_L = 100m/s$ and $T_{He} = 0°C$
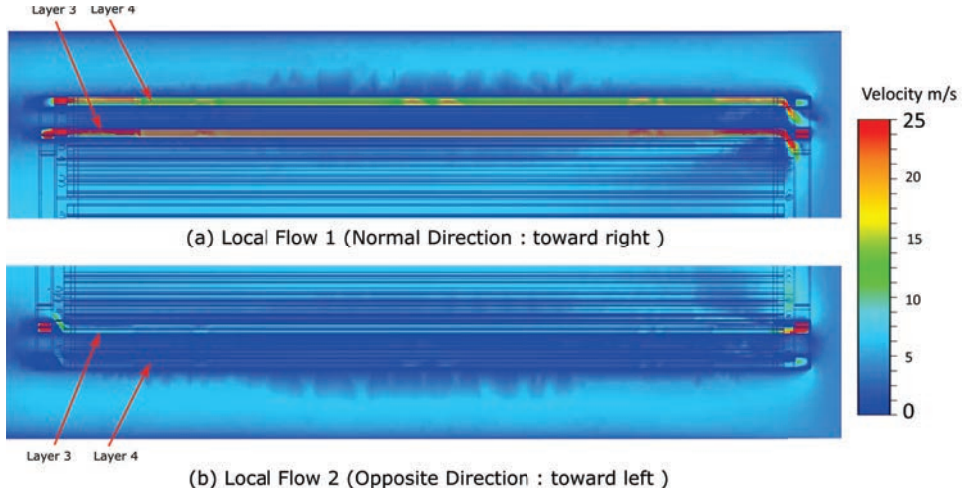
Figure 10.4: Flow profile of the detector station with double fold design, $P/A = 400mW/cm^2$, $v_{global} = 4m/s$, $v_{G+L} = 200m/s$, $v_L = 100m/s$ and $T_{He} = 0°C$. (a) shows the local flow coming from local end-ring, (b) shows the addition local flow from the gap+local end-ring
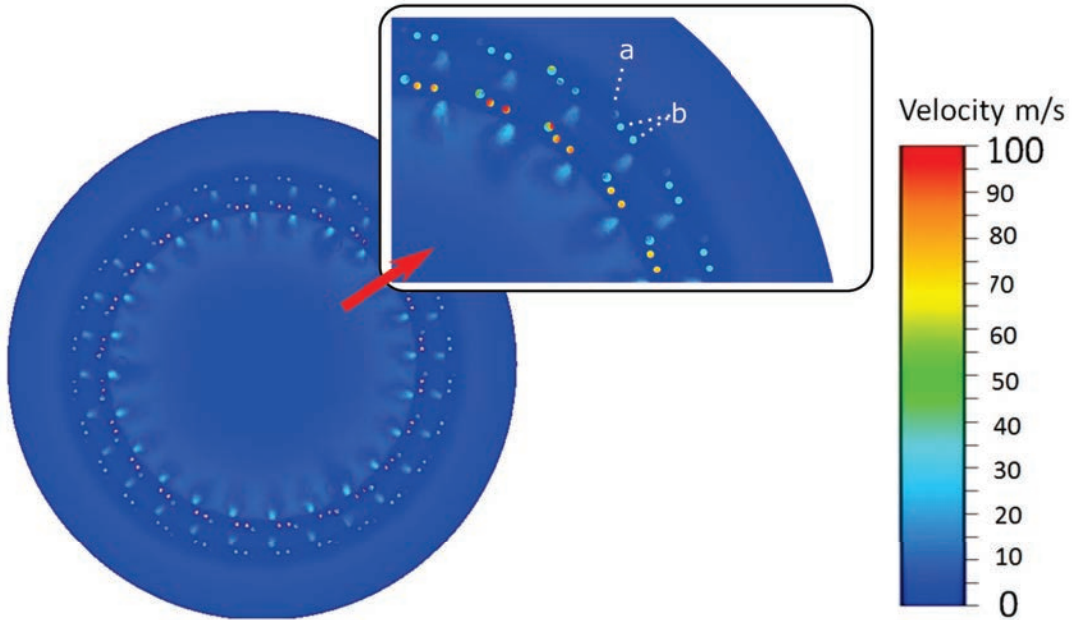
Figure 10.5: Flow profile at the outlet, with inlet velocity $v_{G+L} = 200m/s$. The hole type (a) is the outlet of the gap channel and (b) is the local channel 2

Double End-Ring

The conclusion is that the end-ring with the current structure fails to deliver a uniform gas distribution. The second attempt is to decouple the local flow channel from the gap end-ring. By adding an extra local end-ring between the gap end-ring and the end-piece, it is possible to control the flow velocity into the two channel separately. The design is shown in figure 10.6. The flow pattern with the end-ring configuration can be found in figure 10.7. The model is simulated with the same boundary conditions as in the previous section, except the velocity in the inlet, where $v_{inlet} = 100m/s$ for all inlets of all end-ring. The temperature profile of the sensors is shown in figure 10.8. The temperature profile is significantly decreased by about $20°C$ compared to the single fold design. Here, the simulation gives a maximum temperature of $38°C$. The flow profile is shown in figure 10.9. Uniform flows in the channels are achieved with this design.
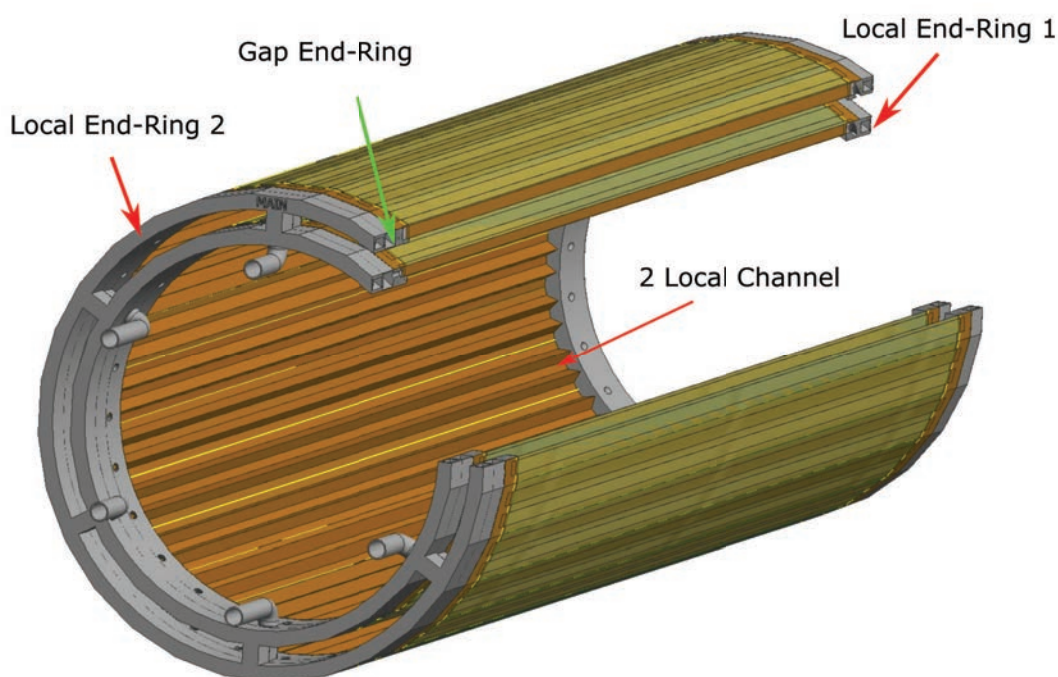
Figure 10.6: Detector model of the double flow design and double end-ring

In this design, the additional local channel for the reverse flow reduces the overall temperature significant only if one can design an end-ring structure which gives uniform and efficient gas distribution. Until further optimization, the gas distribution system in the baseline design would be unusable due to the limited number of gas inlets. As one of the aims for the end-ring design is to minimize the dead zone between stations by reducing the thickness of the structures, despite the excellent cooling performance, the addition end-ring in the double end-ring compromises this concept. Also, one has to point out that twice the amount of helium in the double fold design is used, compare with the single fold design.
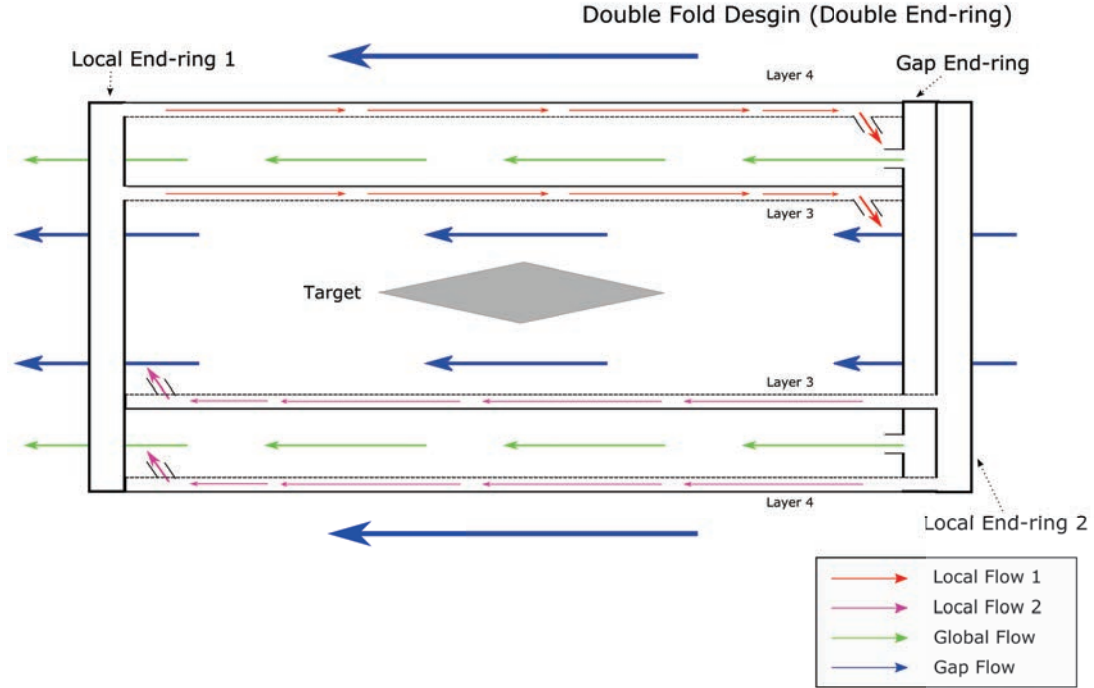
Figure 10.7: Schematics for the flow pattern of the double flow design with double end-ring
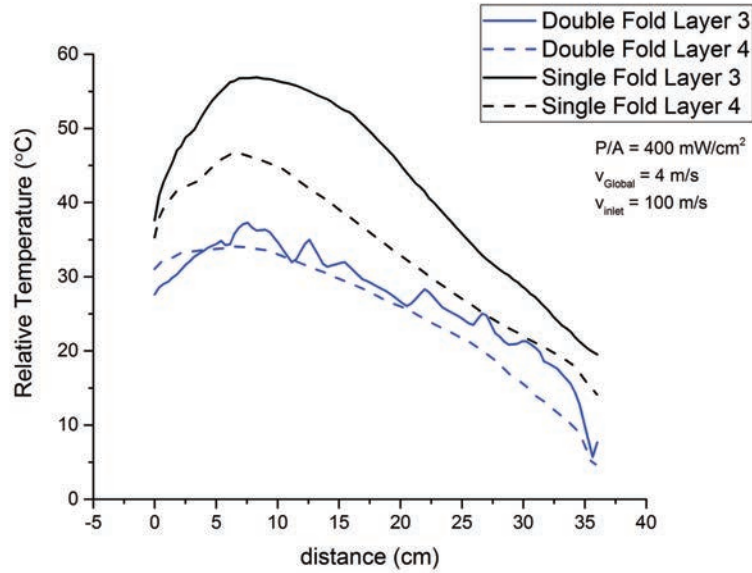
Figure 10.8: Temperature profile of the detector station of double flow design with double end-ring, $P/A = 400mW/cm^2$, $v_{global} = 4m/s$, $v_{inlet} = 100m/s$ ($v_{local} \approx 16m/s$ and $v_{gap} \approx 3.5m/s$) and $T_{He} = 0°C$
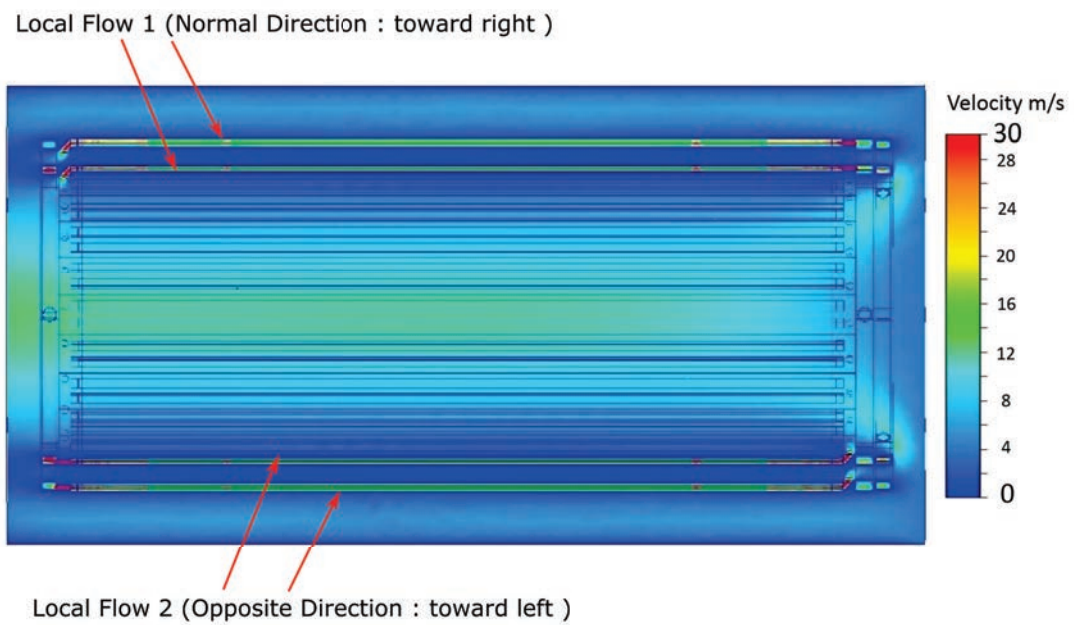
Figure 10.9: Flow profile of the detector station of double flow design with double end-ring, $P/A = 400mW/cm^2$, $v_{global} = 4m/s$, $v_{inlet} = 100m/s$ ($v_{local} \approx 16m/s$ and $v_{gap} \approx 3.5m/s$) and $T_{He} = 0°C$

10.2 Large Fold design

The Large Fold design is proposed as an alternative solution for the optimization of the local flow channel. Besides the increase the number of V-shaped structures, one can simply increase the size of the V-shape. A module with such design is shown in figure 10.10. The height of the triangle is increased from 5.2 to 6 mm with a base from 6 to 7.5 mm. Due to the increase in height of the V-shaped fold, the end-piece has to be enlarged as well. This module is duplicated to form a barrel station and attached to the same end-ring as in section 7.2, but with 3 mm outlet hole.

Figure 10.10: CAD model for a module of the large flow design

Analysis

The model is simulated under the same boundary conditions as the single V-shaped model in section 7.2 :

- Total Heat Flow on the silicon segment, corresponds to $P/A = 400 mW/cm^2$

- $v_{inlet} = 100 m/s$ for all inlets

- $v_{global} = 4 m/s$ at the right end of the flow tunnel

- $T_{He} = 0°C$ for all inflowing helium

- zero overpressure at the left end of the flow tunnel

The result is illustrated in figure 10.11. A detailed plot of the temperature profile for the sensor layers is shown in figure 10.12. A significant decrease in maximum temperature by $10°C$ is observed in layer 3. A rise in temperature of layer 3 is observed at the right end. As the helium in the local channel carries away more heat from the sensor, it is hotter when it leaves the local channel. Therefore, the released local helium heats up the fresh global helium and lead to a reduced cooling on the right side. Despite that, the design gives still an excellent cooling performance considering that it is using the same flow rate at the inlet as the baseline design discussed earlier.
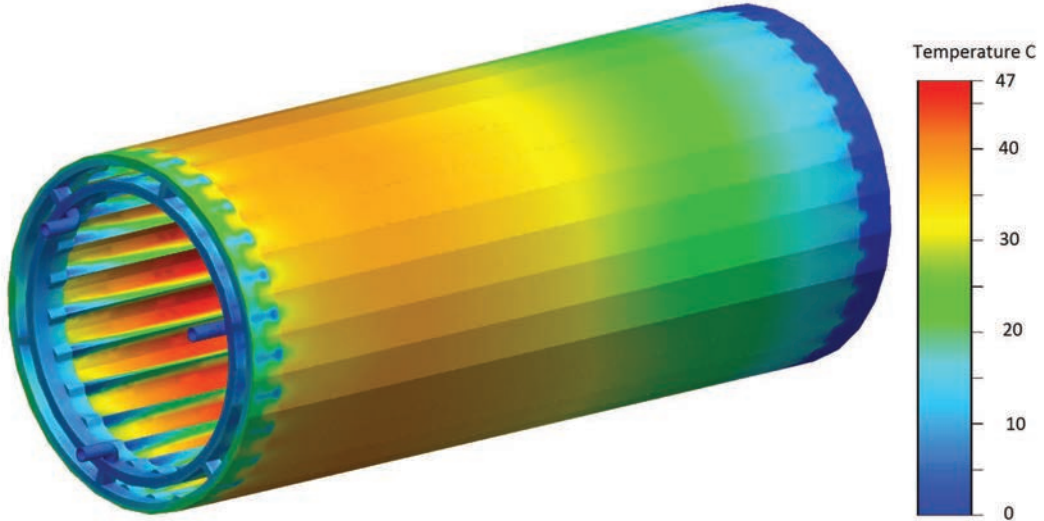
Figure 10.11: Simulation for one outer detector station of Large fold design, P/A $= 400\ mW/cm^3$, $v_{global=4m/s}, v_{inlet} = 100m/s; v_{local} \approx 10m/s$

Figure 10.12: Temperature profile of the detector station of Large fold design, $P/A = 400mW/cm^2$, $v_{global} = 4m/s$, $v_{inlet} = 100m/s$ and $T = 0°C$

Chapter 11

Summary

The goal of the Mu3e experiment is to search for the charged lepton flavor violating muon decay $\mu^+ \to e^+ e^- e^+$ with a sensitivity to the branching ratio of 10^{-16}. As the decay is strongly suppressed in the Standard Model, the signal decay will be a clear sign of New Physics Beyond the Standard Model.

To reach the desired sensitivity a detector with high resolution is needed to suppress background from the decay signal. The Mu3e detector makes use of High Voltage-Monolithic Active Pixel Sensors (HV-MAPS) to provide precise momentum and vertex resolution, complemented by a time of flight systems for precise timing resolution. As the muon has a relatively small mass of $m_\mu = 105.6 MeV/c^2$, its decay products are reconstructed in the low energy regine, where multiple coulomb scattering will be the dominating limitation to the resolution. Therefore in order to minimize the radiation length of the detector a low material budget is required. This can be fulfilled by thinning down the HV-MAPS chips to $50 \mu m$.

A HV-MAPS chip was designed for the Mu3e experiment named MuPix. The power consumption of MuPix is expected to be approximately $250 mW/cm^2$. To keep the temperature of the sensor below $70°C$ and at the same time minimize the use of extra material, a gaseous helium cooling system operated at 0 °C is used in the acceptance region, complemented by a water cooling system in the inactive region.

In order to study the Mu3e cooling concept, a series of Computational Fluid Dynamics (CFD) simulations is performed using Finite Element Method (FEM). 3D CAD models of the Mu3e detector are constructed using Autodesk® Inventor. The CFD simulation is carried out using Autodesk® CFD with the 3D CAD models under various condition.

In chapter 5, a simulation of modules of Mu3e outer detector is carried out. The boundary condition is set identical as the cooling test carried out in a previous thesis in order to compare and verify the result.

In chapter 6, the simulation is carried out with the Mu3e design situation. A simulation of one outer pixel detector station shows a maximum relative temperature at around 37 °C for a power consumption of $400 mW/cm^2$ on the sensors, and a combination of global helium cooling with flow velocity $v_{global} = 4m/s$, gap helium cooling with flow velocity $v_{gap} \approx 4m/s$ and local helium cooling with flow velocity $v_{local} \approx 20m/s$. Two outer detector stations are then added upstream and downstream to the model. With the same boundary conditions, maximum relative temperatures of around 53 °C are found. Both of the results show that the design is sufficient for cooling up to three outer detector station with power consumption of $400 mW/cm^2$, 60% higher than the expected value of $250 mW/cm^2$.

To minimize the use of material of the gaseous inlet and the dead zone between stations, a modification is applied on the helium gas distribution system. A compact end ring with end-structures integrated and thickness reduced to 20mm is introduced. The simulation in chapter 7 shows that a uniform gas distribution is possible with 3 gas inlets for the tested geometry. The model of the outer detector station is equipped with the compact end-ring and simulated with power consumption of $250mW/cm^2$ and $400mW/cm^2$ respectively. Cooling with global flow velocity of $v_{global} = 4m/s$ and inlet flow velocity of $v_{inlet} = 100m/s$ (equivalent to $v_{local} \approx 16m/s$ and $v_{gap} \approx 3.5m/s$) is applied. The temperature of the simulations lies within the limitation of $70°C$. The temperature can be reduced by adjusting the flow velocity at the inlets. Simulations indicate that further reduction in thickness of the end-structure to 10mm is possible, with the price of rapid increase in pressure in the gas distribution system.

In chapter 8 and 9, the Mu3e detector for phase I is simulated including the inner detector, target, beam pipe, recurl stations, time of flight detectors, FPGA chip and the water cooling system. The detector configuration for phase Ia and phase Ib are simulated separately with power consumptions of $250mW/cm^2$ and $400mW/cm^2$ on sensor and 25W per FPGA chip. The result for the $250mW/cm^2$ scenarios indicate that the cooling concept is capable of cooling down the detector by using helium global cooling with flow velocity $v_{global} = 4m/s$, helium flow velocity at the end-ring inlets $v_{inlet} = 100m/s$ (equivalent to $v_{local} \approx 16m/s$ and $v_{gap} \approx 3.5m/s$) and water cooling with flow velocity $v_{water} = 1.36m/s$ at $0°C$. The cooling performance can be improved by increasing further the flow velocity at the helium gas inlet. The simulation of $400mW/cm^2$ scenario is carried out under the same conditions. However, the simulations indicate that the cooling system will be incapable of cooling down the detector for both phase Ia and Ib. For the phase Ia detector with only central and inner detector, sensors on layer 1 excess the maximum working temperature of $70°C$. For phase Ib, layer 1 and also layer 3 of the central station will reach a temperature over $70°C$. Therefore, a improvement in the cooling design is necessary for the power consumption at $400mW/cm^2$. One may consider improvement in the local cooling design and the global cooling between layer 3 and 4, buy adding helium local cooling in the inner detector.

In chapter 10, two designs for improving of local cooling are studied : the " Large Fold " design with an increase of the size of the flow channel and the " Double Fold" design by using a pair of flow channels under each sensor segment. The results from simulation using the outer detector indicate that both designs improve the cooling performance significantly. The cooling performance of " Double Fold design " is more efficient than " Large Fold design ", because of the additional helium flow. However, for the " Double Fold " Design, the gas distribution system will be hard to engineer. Also, an increase of the inactive region at the end-ring structure may be required. Therefore, unless the cooling performance becomes critical for the detector, this design is not recommended. For the case of the " Large Fold " design, the performance is excellent considering that all the boundary conditions are the same as in the simulation for the baseline design, without the necessity of modification of the gas distribution system .

Appendix A

Experiments in CLFV Searches

The SINDRUM Experiment

The *SINDRUM* experiment was carried out from 1983 to 1986 at the Paul Scherrer Institute (PSI) in Switzerland. The goal was to search for the decay $\mu^+ \to e^+e^-e^+$. Low energy mouns of 28 MeV/c were stopped by a hollow double-cone shaped target under a solenoidal magnetic field of 0.33T. The decayed electrons were detected by multiwire proportional chambers and a trigger hodoscope. The sensitivity of the experiment to the deacy $\mu^+ \to e^+e^-e^+$ was mainly determined by the decay $\mu \to eee\nu\nu$ and estimated as $5 \cdot 10^{-14}$ [9]. The limit for the branching ratio was $BR(\mu^+ \to e^+e^+e^-) < 1 \cdot 10^{-12}$ at 90% CL and no signal was found. The obtained limit was given by the limited number of muon stops.

The MEG Experiment

The *MEG* experiment has been carried out since 2008 at the PSI, searching for the decay $\mu^+ \to e^+\gamma$. Low energy mouns are stopped by a thin target. The decay positrons are detected by the drift chambers and the photons in a liquid xenon calorimeter. The sensitivity is limited by accidental background. The current limit on the branching ratio of this experiment is $B(\mu^+ \to e^+\gamma) < 5.7 \cdot 10^{-13}$ at 90% CL[11]. No signal was found so far.

Muon Conversion Experiments

Muon to electron conversion experiments $\mu \to e$ make use of the signature of decay monochromatic electrons [12]. Several experiments has been carried out for the search of the decay with various nuclei. The strongest limit has been set using gold target $Br(\mu Au \to eAu) < 7 \cdot 10^{-13}$ by the *SINDRUM II* Experiment [10]. New experiments have been planned at Fermilab (Mu2e [13]) and at J-PARC (COMET[14] and PRISM [15]), aiming for branching ratio of 10^{-16}.
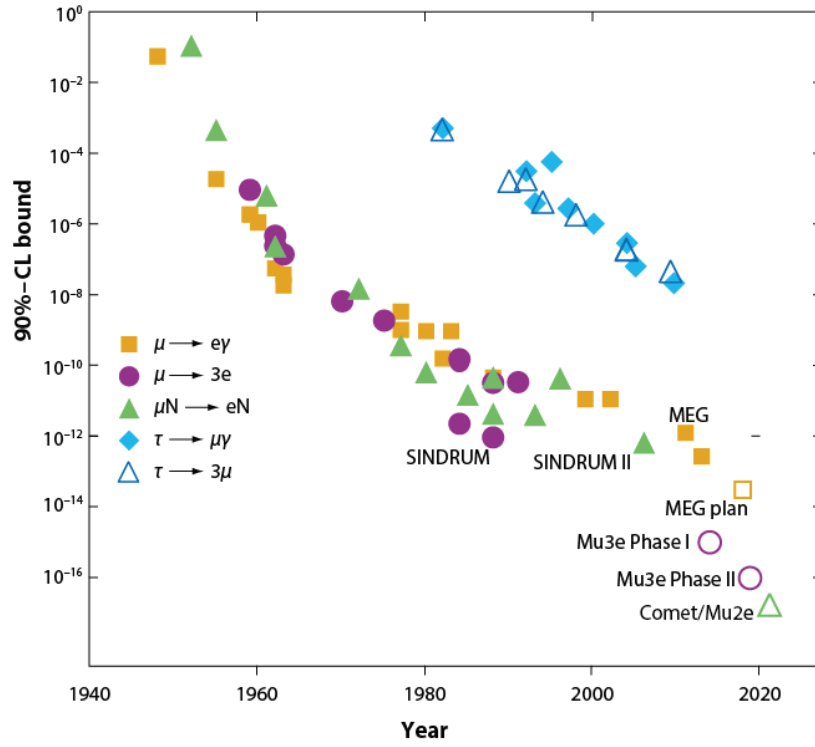
Figure A.1: Overview of experiment for the search in CLFV decay over the last 70 years [8]

Appendix B

Governing Equation in Autodesk® CFD

Th In Autodesk CFD, the time-averaged governing equations is used [26]. It is obtained by assuming that the dependent variables can be represented as a superposition of a mean value and a fluctuating value. Take the x-velocity component u as an example, it can be written as:

$$u = U + u' \tag{B.1}$$

where U is the mean velocity and u' is the fluctuation around the mean. By substituting this representation, the time averaged governing equations can be obtained. The time averaged governing equations for the incompressible turbulent model can be written as :

Continuity Equation

$$\frac{\partial \rho}{\partial t} + \frac{\partial \rho u'}{\partial x} + \frac{\partial \rho v'}{\partial y} + \frac{\partial \rho w'}{\partial z} = 0 \tag{B.2}$$

X-Momentum Equation

$$\rho \frac{\partial U}{\partial t} + \rho U \frac{\partial U}{\partial x} + \rho V \frac{\partial U}{\partial y} + \rho W \frac{\partial U}{\partial z} = \rho g_x - \frac{\partial p}{\partial x} + S_{DR} + S_\omega$$
$$+ \frac{\partial}{\partial x} \left[2\mu \frac{\partial U}{\partial x} - \rho u'u' \right] + \frac{\partial}{\partial y} \left[\mu \left(\frac{\partial U}{\partial y} + \frac{\partial V}{\partial x} \right) - \rho u'v' \right] + \frac{\partial}{\partial z} \left[\mu \left(\frac{\partial U}{\partial z} + \frac{\partial W}{\partial x} \right) - \rho u'w' \right] \tag{B.3}$$

Y-Momentum Equation

$$\rho \frac{\partial V}{\partial t} + \rho U \frac{\partial V}{\partial x} + \rho V \frac{\partial V}{\partial y} + \rho W \frac{\partial V}{\partial z} = \rho g_z - \frac{\partial p}{\partial y} + S_{DR} + S_\omega$$
$$+ \frac{\partial}{\partial x} \left[\mu \left(\frac{\partial U}{\partial y} + \frac{\partial V}{\partial x} \right) - \rho u'v' \right] + \frac{\partial}{\partial y} \left[2\mu \frac{\partial V}{\partial y} - \rho vv \right] + \frac{\partial}{\partial z} \left[\mu \left(\frac{\partial V}{\partial z} + \frac{\partial W}{\partial y} \right) - \rho v'w' \right] \tag{B.4}$$

Z-Momentum Equation

$$\rho \frac{\partial W}{\partial t} + \rho U \frac{\partial W}{\partial x} + \rho V \frac{\partial W}{\partial y} + \rho W \frac{\partial W}{\partial z} = \rho g_z - \frac{\partial p}{\partial z} + S_{DR} + S_\omega$$
$$+ \frac{\partial}{\partial x} \left[\mu \left(\frac{\partial U}{\partial z} + \frac{\partial W}{\partial x} \right) - \rho u'w' \right] + \frac{\partial}{\partial y} \left[\mu \left(\frac{\partial V}{\partial z} + \frac{\partial W}{\partial y} \right) - \rho v'w' \right] + \frac{\partial}{\partial z}] \left[2\mu \frac{\partial W}{\partial z} - \rho ww \right] \tag{B.5}$$

where ρ is the fluid density, p is the pressure, μ is the dynamic viscosity, and $g_{x,y,z}$ is the gravitational acceleration in x,y,z directions. S_{DR} and S_{ω} are the source term for distributed resistance and rotation coordinates.

Energy Equation

$$\rho c_p \frac{\partial T}{\partial t} + \rho c_p U \frac{\partial T}{\partial x} + \rho c_p V \frac{\partial T}{\partial y} \rho c_p W \frac{\partial T}{\partial z} =$$
$$\frac{\partial}{\partial x}\left[k\frac{\partial T}{\partial x} - \rho C_p u'T'\right] + \frac{\partial}{\partial y}\left[k\frac{\partial T}{\partial y} - \rho C_p v'T'\right] + \frac{\partial}{\partial z}\left[k\frac{\partial T}{\partial z} - \rho C_p w'T'\right] + Q_V \quad \text{(B.6)}$$

where T is the average temperature, T' is the temperature fluctuation, c_p is the constant pressure specific heat, k is the thermal conductivity and Q_V is the volumetric heat source.

The averaging process produces extra terms in the momentum and energy equations : $\rho u'u'$, $\rho u'v'$, $\rho u'w'$, $\rho v'v'$, $\rho v'w'$, $\rho C_p u'T'$, $\rho C_p v'T'$, $\rho C_p w'T'$. These terms are combinations of fluctuating quantities resulting from averaging the non-linear inertia or advection terms. These extra terms are called Reynolds stress terms.

The further formulation of the PDEs and calculations of the matrix solver can be found in the dissertation of Rita Jane Schnipke [26] and will not be covered in this thesis.

List of Figures

List of Tables

Bibliography

[1] N. Berger et al., [Mu3e Collaboration], *"Reseach Propossal for an Experiment to Search for the Decay $\mu \to eee$ "*, 2013, arXiv:1301.6113 [physics.insdet].

[2] A. Herkert, *Gaseous Helium Cooling of a Thin Silicon Pixel Detector for the Mu3e Experiment*, Institute of Physics, Master's thesis, 2015

[3] H. Augustin, *"Characterization of a novel HV-MAPS Sensor with two Amplification Stages and first examination of thinned MuPix Sensors*, Master thesis, Institute of Physics, Heidelberg University, 2014.

[4] R. Philipp, *"Characterisation of High Voltage Monolithic Active Pixel Sensors for the Mu3e Experiment"*, Master thesis, Institute of Physics, Heidelberg University, 2014.

[5] A.-K. Perrevoort, *Characterisation of High Voltage Monolithic Active Pixel Sensors for the Mu3e Experiment*, Master Thesis, Institute of Physics, Heidelberg University, 2012.

[6] M. Zimmermann, *"Cooling with Gaseous Helium for the Mu3e Experiment"*, Bachelor's thesis, Heidelberg University, 2012.

[7] L. Huxold, *"Cooling of the Mu3e Pixel Detector"*, Bachelor's thesis, Heidelberg University, 2014.

[8] W. J. Marciano, T. Mori and J.M. Roney, *"Charged Lepton Flavor Violation Experiments"*, Annu. Rev. Nucl. Part. Sci. 58,31541, 2008.

[9] U. Bellgardt et al., [SINDRUM Collaboration], *"Search for the Decay $\mu^+ \to e^+ e^+ e^-$ "*, Nucl. Phys. B 299 1, 1-6, 1988.

[10] W. Bertl et al., [SINDRUM II Collaboration], *"A Search for μtoe conversion in muonic gold"* , Eur. Phys. J. C 47, 337346, 2006.

[11] J. Adam et al. [MEG Collaboration] *"New constraint on the existence of the $\mu^+ \to e^+ \gamma$ decay."*, Phys. Rev. Nucl. Rev. Lett. 110, 201901, 2013, arXiv:1303.0754 [hep-ex].

[12] Y. Kuno and Y. Okada, *"Muon Decay and Physics Beyond the Standard Model"*, Rev. Mod. Phys. 73, 151-202, 2001, arXiv:hep-ph/9909265.

[13] R. Tschirhart, *"The Mu2e experiment at Fermilab"*, Nucl. Phys. B Proc. Suppl. 210-211, 245-248, 2011.

[14] R. Akhmetshin et al., [COMET Collaboration], *Experimental Proposal for Phase-I of the COMET Experiment at J-PARC*, KEK/JPARC-PAC 2012-10, 2012.

[15] Y. Kuno, *"Lepton Favor violation: Muon to electron conversion, COMET and PRISM/ PRIME at J-PARC"*, PoS NUFACT08 111, 2008.

[16] Y. Fukuda et al., [Super-Kamiokande Collaboration], *" Evidence for oscillation of Weak interaction"*, Phys. Rev. Lett. 81, 156211567, 1998, arXiv:hep-ex/9807003.

[17] Q. R. Ahmad et al., [SNO Collaboration], *Measurement of the charged current interactions produced by B-8 solar neutrinos at the Sudbury Neutrino Observatory*, Phys. Rev. Lett., 87 071301, 2001.

[18] K. Eguchi et al., [KamLAND Collaboration], *First results from KamLAND: Evidence for reactor anti- neutrino disappearance*, Phys. Rev. Lett., 90 021802, 2003.

[19] P.-R. Kettle, PSI-internal, LTP Filzbach Meeting, June 2010.

[20] I. Peric, *"A novel monolithic pixelated particle detector implemented in high-voltage CMOS technology"*, Nucl. Instrum. Meth. A582 (3), 876885, 2007.

[21] I. Peric, C. Kreidl and P. Fischer, *"Particle pixel detectors in high-voltage CMOS technology - New achievements* , Nucl. Instr. Meth., A 650(1) 158   162, 2011, International Workshop on Semiconductor Pixel Detectors for Particles and Imaging 2010.

[22] I. Peric and C. Takacs, *Large monolithic particle pixel-detector in high-voltage CMOS technology* , Nucl. Instrum. Meth., A624(2) 504 508, 2010, New Developments in Radiation Detectors - Proceedings of the 11th European Symposium on Semiconductor Detectors.

[23] R. M. Djilkibaev and R. V. Konoplich, *"Rare Muon Decay $\mu^+ \rightarrow e^+ e^+ e^- \nu_e \overline{\nu}_\mu$* , Phys. Rev. D 79, 073004, 2009, arXiv:0812.1355 [hep-ph].

[24] Robert Cook et al., *Concepts and Applications of Finite Element Analysis*, John Wiley & Sons, 1989.

[25] White, F.M., *Viscous Fluid Flow*, McGraw-Hill, New York, 1974.

[26] Schnipke, R.J., *A Streamline Upwind Finite Element Method For Laminar And Turbulent Flow*, Ph.D. Dissertation, University of Virginia, May 1986.

[27] L.H. Thomas, *Elliptic Problems in Linear Difference Equations over a Network*, Watson Sci. Comput. Lab. Rept., Columbia University, New York, 1949.

[28] P. Wesseling, *"Principles of Computational Fluid Dynamics"*, Springer, 2001.

[29] F. P. Incropera, D. P. DeWitt, T. L. Bergman and A. S. Lavine, *"Fundamentals of Heat and Mass Transfer"*, John Wiley & Sons, Inc., textbook, 2007, ISBN: 9780471457282.

Acknowledgement

Declaration

I hereby acknowledge that I am aware of the prerequisites to be met for the assignment of Master's thesis topics under the Examination Regulations of the SciTec Department of the Jena University of Applied Sciences. Also, I declare that I am not in the process of taking a Master's examination in the same field at any other university or college in the territory to which the German Higher Education Framework Act applies. Nor is it true that I irrevocably failed a Master's examination in the same subject area at a university or college in the territory to which the German Higher Education Framework Act applies. I declare that I will observe rules of good scientific practice.

Heidelberg, den (Datum)   . . . .